N° d'ordre : **ANNÉE 2012**

UNIVERSITÉ DE RENNES 1

THÈSE / UNIVERSITÉ DE RENNES 1
sous le sceau de l'Université Européenne de Bretagne

pour le grade de

DOCTEUR DE L'UNIVERSITÉ DE RENNES 1

Mention : Génie Biologique et Médical

Ecole doctorale Vie-Agro-Santé

présentée par

Vito Giovanni Ruggieri

Préparée à l'unité de recherche LTSI – INSERM UMR 1099
Laboratoire Traitement du Signal et de l'Image
UFR Informatique Electronique (ISTIC)

Analyse morphologique des bioprothèses valvulaires aortiques dégénérées par segmentation d'images TDM

Thèse soutenue à Rennes
le 07 décembre 2012

devant le jury composé de :

Jean-Nicolas DACHER
Professeur Université de Rouen / *Rapporteur*

Chafiaa HAMITOUCHE-DJABOU
Professeur Télécom Bretagne / *Rapporteur*

Roland DEMARIA
Professeur Université de Montpellier 1 / *Examinateur*

Jean-François HEAUTOT
Praticien Hospitalier, CHU de Rennes / *Examinateur*

Jean-Philippe VERHOYE
Professeur Université de Rennes 1/*Directeur de thèse*

Pascal HAIGRON
Professeur Université de Rennes 1/*Co-directeur*

Remerciements

Le premier remerciement est adressé à Milena, mon épouse, à qui j'ai dédié cette thèse. Ton amour représente la source de toute l'énergie qui me permet d'avancer.

Je remercie mes parents, qui m'ont permis de grandir dans les meilleures conditions et qui partagent avec un amour inconditionné tant les difficultés que les succès de ma vie.

Je souhaite remercier aussi :

- le Pr Alain Leguerrier pour la confiance qu'il m'a accordée pendant ma permanence dans le Service de Chirurgie Cardiovasculaire et Thoracique du C.H.U. de Rennes. Il restera pour moi un exemple de management, fondé sur un esprit d'équipe qui se traduit par une collaboration quotidienne entre collègues, dans d'idéales conditions, permettant de faire ressortir le meilleur de chacun.

- le Pr Hervé Corbineau pour son aide technique au bloc opératoire qui a facilité et accéléré mon apprentissage dans la pratique chirurgicale. Ceci m'a permis de dédier du temps à d'autres projets, dont celui de cette thèse.

- le Dr Erwan Flecher pour son encouragement quotidien et son amitié que j'espère vivement garder à jamais.

- toute l'équipe des cardiologues interventionnels pour leur collaboration, et en particulier le Pr Hervé Le Breton pour sa disponibilité à participer en tant que membre invité à la soutenance de cette thèse.

- l'équipe de Radiologie, en particulier le Dr Jean-François Heautot et le Dr Antoine Larralde pour la disponibilité qui m'ont accordée pendant ces années et qui m'a permis d'avancer dans mes travaux.

Un grand remerciement au Pr Pascal Haigron, qui a représenté pour moi le "stargate" vers le monde de l'ingénierie. Son aide indispensable a permis de faciliter la communication avec les amis chercheurs et de traduire mes idées en "numérique".

Je remercie le doctorant Qian Wang, mon alter ego ingénieur. Son aide sur le plan mathématique et technique a été indispensable du début jusqu'à la fin de cette extraordinaire expérience de collaboration France-Italie-Chine.

Je remercie aussi le doctorant Raphael Madeleine du LTSI ainsi que le Docteur Simon Esneault de la Societé Therenva qui ont bien participé au développement de ce projet sans être directement impliqués.

Je souhaite remercier l'association ADETEC et la société St Jude Medical. Leur soutien financier a permis le développement et la finalisation de ce travail dans les meilleures conditions.

Au final, un remerciement particulier au Pr Jean Philippe Verhoye. Grace à ses capacités humaines hors du commun et son regard vers le futur, j'ai pu, ces dernières années, avancer rapidement dans différentes directions, tout en gardant comme centre de gravité, l'intérêt et le respect du patient. Je n'oublierai jamais son aide fondamentale à ma maturité personnelle et professionnelle.

Analyse morphologique des bioprothèses valvulaires aortiques dégénérées par segmentation d'images TDM

Résumé

Le but de cette étude est d'évaluer la faisabilité de l'analyse tomodensitométrique 3D des bioprothèses aortiques pour faciliter leur évaluation morphologique durant le suivi et d'aider à la sélection des cas et à l'amélioration de la planification d'une procédure valve-in-valve. Le principal défi concernait le rehaussement des feuillets valvulaires, en raison d'images très bruitées.

Un scanner synchronisé était réalisé chez des patients porteurs d'une bioprotèse aortique dégénérée avant réintervention (images in-vivo). Différentes méthodes pour la réduction du bruit étaient proposées. La reconstruction tridimensionnelle des bioprothèses était réalisée en utilisant des méthodes de segmentation de régions par "sticks". Après ré-opération ces méthodes étaient appliquées aux images scanner des bioprothèses explantées (images ex-vivo) et utilisées comme référence.

La réduction du bruit obtenue par le filtre stick modifié montrait de meilleurs résultats, en rapport signal/bruit, en comparaison aux filtres de diffusion anisotrope. Toutes les méthodes de segmentation ont permis une reconstruction 3D des feuillets. L'analyse qualitative a montré une bonne concordance entre les images obtenues in-vivo et les altérations des bioprothèses. Les résultats des différentes méthodes étaient comparés par critères volumétriques et discutés.

Les images scanner des bioprothèses aortiques nécessitent un traitement de débruitage et de réduction des artéfacts de façon à permettre le rehaussement des feuillets prothétiques. La méthode de segmentation de régions par sticks semble représenter une approche pertinente pour caractériser morphologiquement la dégénérescence des bioprothèses.

I - INTRODUCTION

Durant la dernière décennie, l'utilisation de bioprothèses valvulaires aortiques a considérablement augmenté. L'amélioration des techniques chirurgicales et la durabilité des valves ont probablement contribué cette augmentation. D'autre part, ces vingt dernières années, le risque de décès secondaire à une ré-intervention pour une chirurgie valvulaire aortique à parallèlement diminué. La mortalité opératoire des ré-interventions pour chirurgie valvulaire aortique élective est comprise entre 2 et 7%. L'amélioration de la qualité de vie des patients et ces bons résultats chirurgicaux contribuent à la large diffusion de l'implantation des bioprothèses, même chez des patients jeunes. Ce phénomène, associé à l'augmentation de l'espérance de vie dans les pays industrialisés, va probablement avoir des conséquences dans quelques années, quand de nombreux patients âgés présentant des comorbidités multiples vont nécessiter une ré-intervention pour dégénérescence de bioprothèse. Les données de la littérature montrent que le taux de mortalité peut augmenter à plus de 30% chez des patients à haut risque.

Avec l'apparition des valves percutanées pour traiter le rétrécissement valvulaire aortique chez les patients à haut risque opératoire ou récusés à la chirurgie, la communauté médicale a découvert une option séduisante, bien qu'encore débutante, pour traiter le même type de patients présentant une défaillance de bioprothèse. En effet, l'implantation de valves percutanées évite une nouvelle sternotomie, une nouvelle circulation extra-corporelle et peut potentiellement réduire les coûts en accélérant la récupération du malade et en réduisant la durée du séjour hospitalisé. Les résultats préliminaires montrent que la procédure « valve-in-valve » est faisable, mais des études complémentaires sont nécessaires pour accepter définitivement

cette technique moins invasive. Cependant, même si cela n'a pas été accepté de manière définitive par les autorités médicales ni par l'industrie, l'impression générale et les pratiques « sur le terrain » nous font considérer cette procédure comme un traitement prometteur. De multiples petites séries corroborent cette impression générale. En raison d'une meilleure qualité de vie après implantation de bioprothèse aortique, les chirurgiens cardiaques implantent aujourd'hui de plus en plus de matériel biologique, même chez les patients jeunes, au vu de la possibilité future d'implantation de prothèse par voie percutanée en cas de dégénérescence. En effet, cette future option déjà adoptée est responsable de l'extension des indications d'implantation de bioprothèses aux plus jeunes patients avec comme conséquence l'augmentation de l'incidence de la dégénérescence dans les années à venir.

La cause la plus fréquente de défaillance de bioprothèse est la dégénérescence des feuillets valvulaires. L'examen de référence de suivi des patients après remplacement valvulaire aortique reste l'échographie trans-thoracique (ETT), avec l'échographie trans-œsophagienne (ETO) en cas de doute à l'ETT. L'échographie est le gold-standard pour évaluer la fonction des bioprothèses. Cependant, l'ETT et l'ETO restent limitées pour l'exploration morphologique des bioprothèses, spécialement en ce qui concerne les valvules des bioprothèses, à cause de leur finesse et de l'ombre acoustique causée par le stent ou par l'anneau de suture qui gêne souvent une bonne visualisation des feuillets. De plus, du fait de leur nature bidimensionnelle, il est généralement impossible de visualiser les feuillets qui ne sont pas orientés dans le plan de la sonde. Même l'échographie 3D garde, pour le moment, des applications limitées dans le cadre des bioprothèses aortiques, pour les mêmes raisons.

Ces dernières années, le scanner multi-coupes s'est avéré être un outil prometteur pour préciser des informations diagnostiques dans différentes situations cliniques, comme l'évaluation non invasive des coronaires, la fonction ventriculaire, la morphologie ventriculaire et la viabilité myocardique. Le scanner multi-coupes peut aussi aider à visualiser la morphologie et la mobilité des valves natives dans la sténose valvulaire et mesurer avec précision la surface d'ouverture des valves aortiques. Plusieurs études ont montré que le scanner multi-coupes peut aider à définir le mécanisme de dysfonction d'une prothèse valvulaire mécanique. Quelques études récentes ont montré comment le scanner 64 barrettes permet une meilleure visualisation des feuillets des bioprothèses aortiques par rapport à l'échographie et qu'il peut jouer un rôle pour définir le mécanisme de dysfonction.

Grâce à leur haute résolution spatiale, les images scanner nous permettent généralement une reconstruction 3D des structures d'intérêt. D'une manière générale, l'analyse 3D des images augmente la compréhension et facilite la planification adaptée de la procédure chirurgicale ou endovasculaire.

A l'heure actuelle, les logiciels disponibles pour l'analyse et le traitement des images tomodensitométriques ne permettent pas une reconstruction tridimensionnelle adaptée aux feuillets des bioprothèses en raison de leur finesse. Le péricarde bovin et les valves porcines sont en effet trop fins et les images scanner sont trop altérées par le bruit, les artéfacts des stents métalliques et les mouvements du cœur. Ceci rend difficile l'analyse 3D avec les outils dont nous disposons actuellement. De nouvelles méthodes permettant de traiter ces images haute résolution doivent donc être étudiées et proposées.

Le but de cette étude est d'évaluer la faisabilité de l'analyse morphologique des images 3D des bioprothèses dégénérées obtenue grâce au scanner multi-coupes

synchronisé. Il existe de multiples méthodes décrites dans la littérature pour réduire le bruit et segmenter ces images. Après une présentation des approches les plus importantes, nous étudions et proposons des méthodes de débruitage et de segmentation et nous comparons leurs résultats. De plus, nous comparons les analyses morphologiques réalisées à une référence, à savoir les images scanner des valves explantées, traitées suivant le même procédé, pour valider nos résultats.

II – CONTEXTE MEDICAL

Après la présentation des différents types de bioprothèses disponibles et de leur évolution au cours des années, une analyse de la durabilité des bioprothèses en position aortique est réalisée. Plusieurs modalités en termes de dégénérescence peuvent intervenir sur les bioprothèses, mais la dégénérescence des feuillets valvulaires prothétiques reste la plus commune avec le développement de calcifications ou déchirures. L'apparition d'une micro-thrombose des feuillets dans le postopératoire immédiat, liée à un défaut de traitement anti- thrombotique, est à considérer comme un mécanisme favorisant le développement précoce d'une altération structurelle des feuillets.

L'option thérapeutique de choix pour dégénérescence structurelle d'une bioprothèse est représentée par la ré-intervention. Celle-ci est aujourd'hui une option à risque opératoire limité, mais en présence de facteurs aggravants (comorbidités multiples, urgence, etc..) elle peut devenir une intervention à très haut risque.

Le développement des procédures d'implantation endovasculaire (trans-cathéter) des valves a permis de considérer ce type d'implantation valable aussi dans les cas de dégénérescence de bioprothèse dans l'optique de traiter les patients à risque très haut ou prohibitif. La procédure valve-dans-valve représente une option thérapeutique intéressante mais plusieurs problèmes sont encore à considérer concernant la bonne sélection des cas et la réalisation de la procédure qui reste empirique à l'heure actuelle. Une planification et optimisation de cette implantation pourrait améliorer les résultats.

Avec l'arrivée des bioprothèses trans-cathéter nous assistons à la naissance d'une nouvelle époque pour le traitement des maladies valvulaires guidé par l'image. Les

différentes modalités d'imagerie deviennent de plus en plus nécessaires pour les praticiens de nouvelle génération, car la bonne compréhension structurale et morphologique de la pathologie permet une meilleure planification des procédures. Cela se traduit par une plus grande prise de conscience de la pathologie et devrait par conséquent faciliter la décision clinique et améliorer les résultats.

L'évaluation fonctionnelle des bioprothèses après remplacement valvulaire aortique s'appuie sur des paramètres échocardiographiques qui permettent, conjointement aux données cliniques, le suivi des patients. Toutefois, la fiabilité de l'échographie n'est pas la même lorsque l'on s'intéresse à la compréhension morphologique de la dégénérescence des bioprothèses qui pourrait être utile au cours du suivi standard ainsi que pour la prise de décision quant à la solution thérapeutique. Les mécanismes de défaillance tels que les calcifications ou les déchirures, la formation de pannus ou de thrombose des feuillets valvulaires devraient être détectée en pré-opératoire afin de choisir le traitement le plus adapté et de personnaliser la stratégie thérapeutique.

Dans ce contexte, l'un des points clefs de l'analyse morphologique 3D concerne la mise en œuvre de méthodes performantes pour le traitement des images préopératoires. Dans les chapitres suivants, nous présentons l'état de l'art en ce qui concerne l'imagerie cardiaque, en particulier l’imagerie tomodensitométrique, et nous proposons des méthodes pour traiter les images scanner des bioprothèses aortiques. Enfin, nous discutons nos résultats.

III – ETAT DE L'ART

Les techniques d'imagerie cardiaque ont connus un développement très important dans les dernières années. Les modalités existantes permettent une analyse tridimensionnelle de différentes structures cardiaques mais il existe des limites concernant la possibilité d'analyse morphologique tridimensionnelle des bioprothèses aortiques.

Dans cet objectif, l'imagerie tomodensitométrique apparait aujourd'hui comme la modalité d'acquisition la mieux adaptée. En effet le scanner synchronisé permet d'obtenir des images à haute résolution de la bioprothèse valvulaire aortique. Même si l'on peut regretter la présence d'artefacts liés à la partie métallique du stent, ces limitations paraissent moins difficiles à surmonter, à l'heure actuelle, que les limitations de l'IRM en termes de résolution, de distorsion, d'artefacts et d'élaboration de protocoles d'acquisition dédiés. L'intérêt de l'échographie 3D reste pour le moment limité en ce qui concerne les prothèses valvulaires en position aortique.

Plusieurs facteurs interviennent dans la qualité des images du scanner synchronisé. Leur influence se traduit par des images qui peuvent être plus au moins altérées, surtout par le bruit et les artefacts métalliques. Différents types de méthodes de réduction d'artefacts et de bruit, applicables aux images scanner cardiaque, ont été présentées dans la littérature pour corriger ces altérations. Parmi celles-ci nous avons plus particulièrement relevé les méthodes ayant des propriétés directionnelles et fondées sur la diffusion anisotrope. La segmentation consiste quant à elle à réaliser un partitionnement de l'image en ensembles de pixels/voxels, ou segments. De nombreuses méthodes ont été reportées dans la littérature. Les méthodes utilisées dans le cadre des images de scanner cardiaque font notamment appel à

des techniques de type classification ou seuillage, de type région ou de type contour, ou à la combinaison de ces approches.

Les images scanner représentent des images nécessaires et relativement faciles à réaliser dans un contexte de bioprothèses altérées que ce soit dans l'optique d'une ré-intervention ou d'une procédure valve-in-valve. A l'heure actuelle, les logiciels d'analyse d'images scanner disponibles ne permettent pas de traiter les images de façon à rehausser les feuillets prothétiques pour faciliter la segmentation de ces derniers. D'autres méthodes doivent donc être considérées.

IV – MATERIEL ET METHODES

Dans notre étude, nous avons sélectionné des patients préalablement soumis au remplacement valvulaire aortique chirurgical par bioprothèse, hospitalisés pour dégénérescence de bioprothèse et en attente d'une ré-intervention. Ceci nous a permis de traiter et analyser les images préopératoires concernant les bioprothèses et de comparer nos résultats avec les images obtenues à partir des bioprothèses explantées après la chirurgie. Les critères d'exclusion étaient les suivants: opération en urgence, arythmie chronique (fibrillation auriculaire ou de plus de cinq battements cardiaques prématurés par minute), classe fonctionnelle NYHA IV, insuffisance rénale (créatinine sérique supérieure à 1,4 mg / dL) et allergie connue aux produits de contraste iodés.

Pendant une période de 3 ans, 9 patients atteints de dégénérescence de bioprothèse et éligibles pour une ré-intervention ont été considérés pour l'étude. Parmi ceux-ci, 4 patients ont été inclus en fonction des critères de sélection. Trois patients ont été exclus à cause d'une arythmie stable, 1 pour insuffisance cardiaque avec tachycardie compensatrice et 1 pour insuffisance rénale. Les bioprothèses dégénérées considérées se composaient de deux bioprothèses porcines Carpentier-Edwards Supra Annular Valve (23 et 25 mm), d'une bioprothèse péricardique 23 mm Edwards Perimount et d'une bioprothèse porcine 23 mm Medtronic Mosaic. Selon le cas, la ré-intervention a été effectuée à partir de 7 à 19 ans après l'implantation pour différentes raisons pathologiques.

Les protocoles d’acquisition utilisés, réalisés par un scanner multi-coupes à 64 détecteurs de 0,625 mm (General Electric VCT 64 ou Discovery 750HD), étaient les suivants :

- Protocole in-vivo : images préopératoires obtenues par un angio-scanner coronaire synchronisé à l’ECG et centré sur la bioprothèse avec une reconstruction rétrospective de plusieurs phases du cycle cardiaque. La diastole (70% du cycle cardiaque) était considérée la plus adaptée pour analyser une bioprothèse avec ses feuillets en position de fermeture.
- Protocole ex-vivo : images postopératoires de la bioprothèse dégénérée explantée du patient. Un protocole rochers était réalisé de façon à obtenir des images haute résolution à utiliser comme référence.

Nous avons utilisé les données du scanner multi-coupes pour une évaluation morphologique tridimensionnelle des bioprothèses valvulaires aortiques, en particulier des feuillets prothétiques dégénérés.

L'approche proposée pour l'analyse morphologique des feuillets valvulaires est représentée par la figure 1. Les principales étapes intervenant dans le traitement des images sont les suivantes : (1) définition de la région d’intérêt (ROI) selon le type de stent de la bioprothèse, (2) prétraitement pour la réduction du bruit et le rehaussement des images, (3) segmentation des différentes composantes de la bioprothèse par un processus de croissance de régions (4) visualisation tridimensionnelle des résultats.

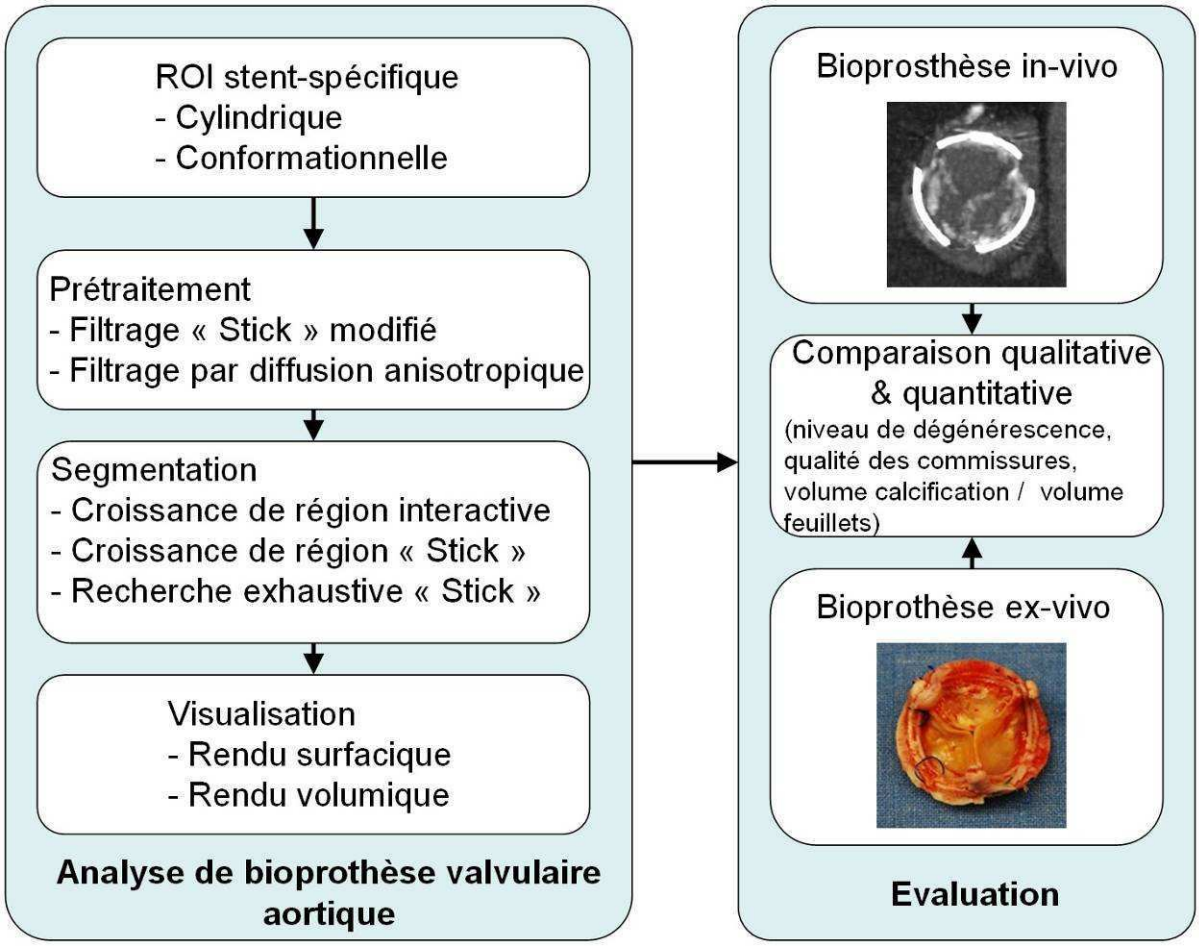

Fig. 1 : Approche proposée pour l'analyse morphologique des bioprothèses valvulaires aortiques dégénérées.

Afin d'évaluer la performance de la segmentation des images « in-vivo » (images préopératoires), les méthodes de segmentation étaient également appliquées aux images « ex-vivo » (bioprothèses explantées).

A. Région d'Intérêt

Afin de faire face aux difficultés rencontrées lors de la segmentation des images tomodensitométriques relatives à la bioprothèse (objets métalliques, finesses des feuillets, densité des composants valvulaires par rapport au stent), nous avons considéré une région d'intérêt (ROI). Bien que cette région doit inclure toutes les structures de la bioprothèse, elle doit également être aussi petite que possible. Dans

cette région, qui est plus petite qu'un volume englobant cubique, la diminution du nombre de voxels doit permettre de simplifier le débruitage et la segmentation (notamment au niveau de la limite externe des feuillets), et de diminuer le pourcentage d'artefacts métalliques et d'erreur de segmentations (principalement causées par le bruit).

La forme de cette région d'intérêt est fonction du type de la valve implantée. Nous avons considéré deux types de forme : (a) cylindrique, utilisée de préférence pour les stents métalliques incomplets et (b) conformationnelle pour les bioprothèses avec stent métallique complet (figure 2).

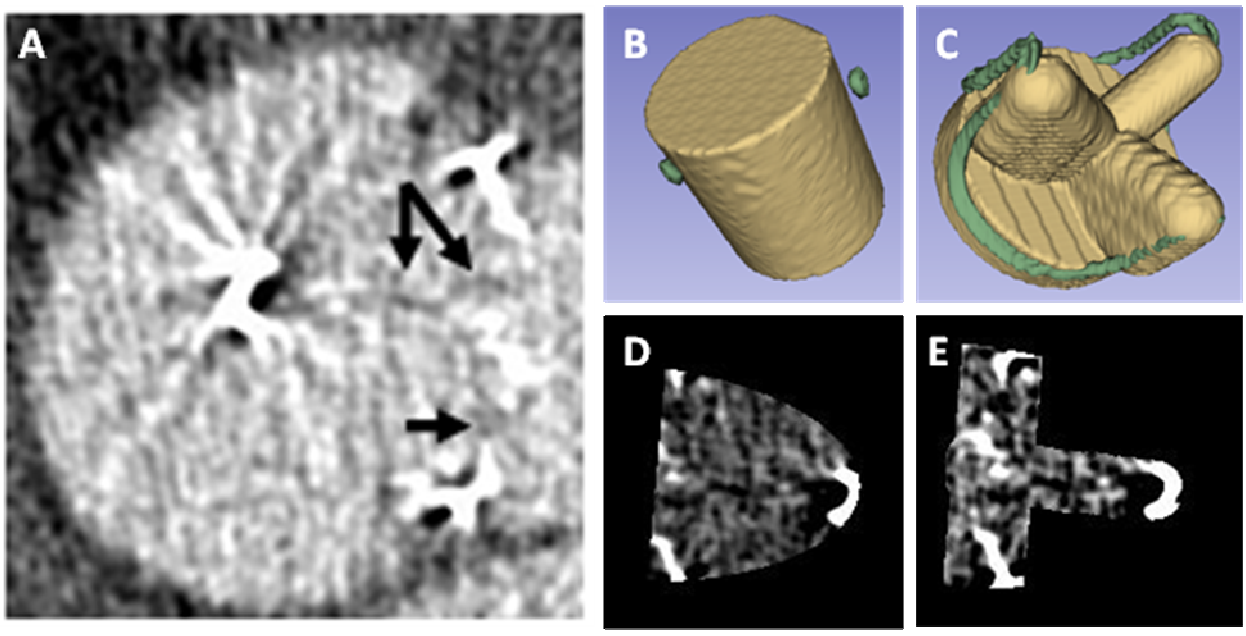

Fig. 2: Région d'intérêt: image TDM dans un volume englobant cubique classique (A), ROI cylindrique (B) et conformationnelle (C), et illustration des images CT correspondantes (D et E respectivement).

B. Prétraitement

Afin de réduire les hyperdensités parasites dans les images tomographiques, un prétraitement est nécessaire. Le but de cette étape est d'augmenter le rapport

signal/bruit (SNR) et d’améliorer le contraste des structures d'intérêt, notamment les feuillets valvulaires.

Nous avons opté pour des méthodes basées sur une adaptation des filtres de diffusion (technique de filtrage anisotrope) et sur une version modifiée et améliorée du filtre "stick", initialement décrit pour le filtrage d’images doppler afin de réduire les échos parasites et d’affiner l’analyse des structures minces. Pour sélectionner l’approche la plus appropriée avant l'étape de segmentation, nous avons considéré le SNR comme critère de performance.

Les *filtres de diffusion anisotrope* ont été présentés dans la littérature pour débruiter les images, notamment les images scanner cardiaques. Grâce à leur aptitude à analyser l'image dans différentes directions, ils permettent d'envisager le rehaussement et le débruitage d’images scanner, tout en conservant les détails des structures fines tels que les feuillets prothétiques. Un niveau de bruit trop élevé dans les images constitue toutefois une limitation pour les filtres de diffusion anisotrope, notamment avec formulation initiale proposée par Perona et Malik. Pour améliorer leur performance dans ces conditions, nous avons utilisé au niveau de la fonction de diffusion la fonction d'arrêt de Tukey et l'écart absolu médian (MAD) conjointement au gradient lissé (Catté_PM) ou à l'information de courbure (ACD). Un filtrage médian a de plus été utilisé pour compléter le processus de filtrage et réduire le bruit impulsionnel.

Le *filtre stick* repose quant à lui sur le partitionnement du voxel considéré en un ensemble de bâtonnets asymétriques pour effectuer un filtrage non-linéaire de l'image. En raison de son asymétrie, le filtre pourrait obtenir de meilleures performances en ce qui concerne la qualité des détails des structures fines (comme les feuillets valvulaires). Ce filtre a été adapté pour le prétraitement des images

scanner de la dégénérescence des bioprothèses aortiques. Dans l'approche proposée, le filtre stick modifié implique une étape préalable de classification, fondée sur l'analyse de configurations particulières dans la région d'intérêt, suivie d'une étape de filtrage adapté à la classe des voxels (lumière vasculaire, feuillets, artefacts, ...).

Contrairement au filtre de diffusion, le nombre d'itérations ne constitue pas un paramètre sensible. Le filtre stick montre un comportement convergent après plusieurs itérations. Typiquement, le résultat converge après 5 itérations pour un SNR inférieur ou égal à 8 et après 3 itérations lorsque le SNR est supérieur à 10. L'inconvénient du filtre stick est sa complexité calculatoire (nombre d'opérations à réaliser). Le temps de calcul peut être raccourci par une ROI définie par le stent. Le nombre de voxels se réduit généralement à 40% du volume englobant cubique avec la ROI cylindrique et à 16% de ce volume avec la ROI conformationnelle.

C. Segmentation de la valve

Quatre types principaux de tissus sont identifiables selon la valeur de densité (Hounsfield Units - HU) mesurée au scanner. Par ordre décroissant de HU on reconnaît: le stent, les calcifications des feuillets, la lumière vasculaire et les feuillets valvulaires. Le premier élément, affichant des valeurs HU élevées, peut être aisément segmenté par seuillage. La segmentation envisagée est plus particulièrement centrée sur les feuillets bioprothétiques.

Trois méthodes de segmentation de régions ont été implémentées (avec différents niveau d'interactivité pour l’utilisateur) pour la segmentation des feuillets prothétiques.

1 - Croissance de région "interactive" (IRG)

Ce processus interactif vise à fournir une approche de référence pour l'évaluation des résultats. Un critère (seuil) d'agrégation des voxels très sélectif a volontairement été choisi afin d'obtenir des régions très homogènes. La contrepartie est la taille très restreinte de ces régions à l'issue de la croissance, et donc la nécessité de définir interactivement un nombre important de points germes pour obtenir une segmentation complète des structures d'intérêt. Cette segmentation est réalisée au moyen du logiciel 3D Slicer après une phase de prétraitement des images basé sur le filtrage par diffusion anisotrope.

Pour chaque composante prothétique, de multiples points germes (environ 20) ont été sélectionnés de façon interactive. L'algorithme par croissance de région a été appliqué (voisinage 26 connexes). Le critère d'agrégation des voxels s'appuie sur la moyenne et l'écart type de la valeur des voxels dans le voisinage cubique considéré. Les valeurs initiales des seuils d'agrégation fournies automatiquement par le logiciel est réajustées interactivement par l'utilisateur. L'extraction et la visualisation des résultats du maillage de surface 3D délimitant les régions ont été réalisées en utilisant l'algorithme du Marching Cube.

2 - Croissance de région Stick (Stick RG)

Afin d'améliorer la segmentation des structures fines, notamment des feuillets valvulaires prothétiques, nous avons développé une méthode par croissance de région directionnelle basé sur un voisinage structuré en bâtonnets (voisinage stick) dans la région d'intérêt (ROI).

Un nombre très limité de points d'origine (en général 4 à 6) sont sélectionnés de manière interactive à l'intérieur des feuillets. Un ensemble de N voxels à l'intérieur des

feuillets a été défini en tenant compte, pour chaque point d'origine, des voxels appartenant à leur voisinage défini par les sticks. Le critère de similitude prend en compte la cohérence des directions de sticks ayant des distributions de niveau de gris comparables (variations des valeurs le long du stick). Cette approche a été mise en œuvre en utilisant les outils de développement logiciel MatLab. Lorsque le voxel appartient à la composante qui nous intéresse, il constitue un nouveau point d'origine. Ce processus est répété jusqu'à ce qu'aucun nouveau voxel ne soit marqué comme appartenant à la même classe que le point germe.

3 – Recherche Exhaustive Stick (SES)

Afin de réduire davantage le niveau d'interactivité dans le processus de segmentation, une exploration systématique de la ROI a été mise en place sans avoir besoin de définir les points germes.

En considérant les voxels situés dans la ROI, nous utilisons le résultat de la classification réalisée dans la phase de prétraitement. Le voisinage (typiquement 7 * 7 * 7 voxels) de tous les voxels à l'intérieur de la ROI est partitionné en un ensemble de sticks asymétriques et analysé afin de classer les voxels comme appartenant à des structures fines (incluant les feuillets), à la lumière vasculaire, à des structures tubulaires (incluant le stent métallique complet) ou aux autres structures (incluant les calcifications et le stent métallique incomplet). En considérant les Sticks S_m présentant de faibles variations locales de valeurs, cette classification est ensuite affinée par seuillage afin d'identifier les voxels appartenant aux composantes de la bioprothèse : feuillets (valeurs moyennes locales faibles le long de S_m), stent métallique complet (valeurs moyennes locales élevées le long de S_m), calcifications et stent métallique incomplet (valeurs moyennes locales le long de S_m supérieures aux valeurs de la lumière artérielle). Pour cette opération trois seuils sont utilisés. Ils

sont déterminés interactivement par simple pointage d'un voxel appartenant au stent, aux calcifications, et à la lumière artérielle. Cette méthode de segmentation simplifie le mode opératoire, mais peut s'avérer moins performante en présence de bruit et d'artefacts en raison de la définition globale des trois seuils.

V – RESULTATS ET DISCUSSION

Pendant la ré-intervention le mécanisme de dégénérescence de chaque bioprothèse explanté était évalué. La figure 3 montre les 4 cas de dégénérescence.

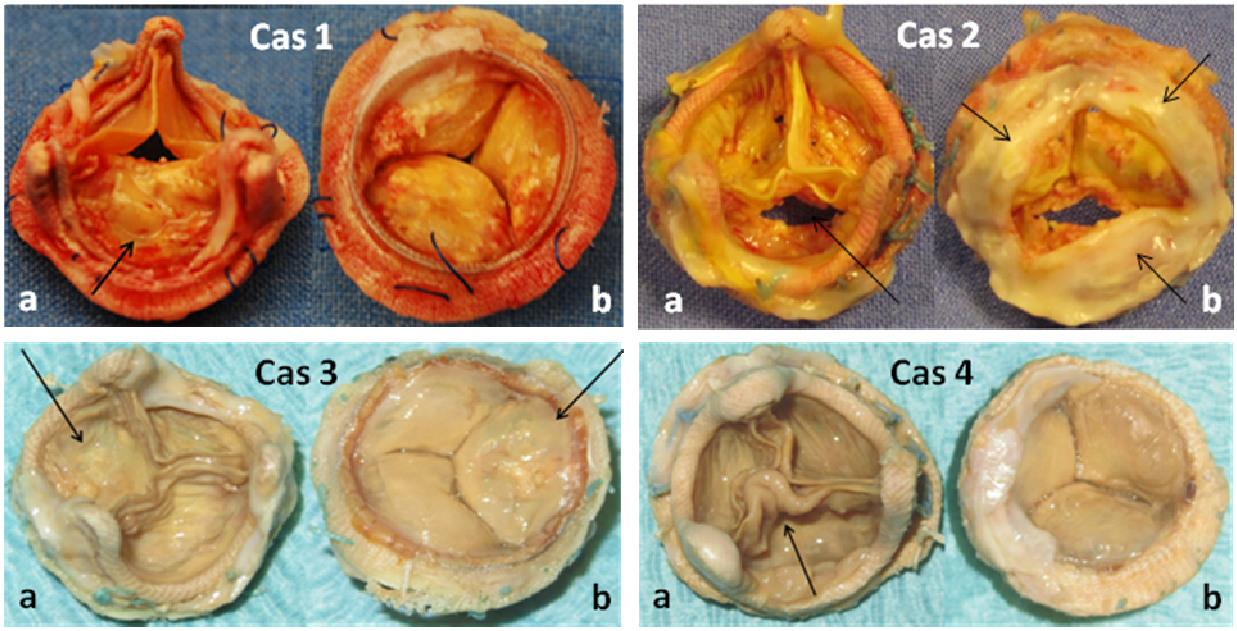

Fig. 3: Cas n°1 – bioprothèse péricardique montrant un prolapsus d'un feuillet calcifié. Cas n°2 – bioprothèse porcine présentant une déchirure d'un feuillet et la présence d'un pannus sous-valvulaire calcifié. Cas n°3 – bioprothèse porcine ayant un feuillet calcifié. Cas n°4 – bioprothèse porcine avec feuillet colonisé par une infection.

Les images du scanner synchronisé préopératoire (in-vivo) ont été d'abord analysées par le logiciel de la console scanner AW Volume Share (General Electric Healthcare workstation) avec des résultats qui n'étaient pas satisfaisants en ce qui concerne le rehaussement des feuillets prothétiques à cause de l'importante quantité de bruit et d'artefacts. Enfin, les images étaient traitées par les méthodes de filtrage et de segmentation proposées.

A. *Prétraitement*

Les voxels spécifiques aux bioprothèses ont d'abord été sélectionnés en considérant la ROI définie par le stent. Une première appréciation qualitative des résultats montre que le filtre Stick modifié rehausse mieux le contraste entre les feuillets valvulaires et les structures environnantes. En plus de cette évaluation qualitative, le SNR a été calculé à partir des images d'origine et des images traitées (figure 4). Cette évaluation objective montre que le filtre stick permet d'obtenir le meilleur SNR pour les quatre patients. Ce résultat est compatible avec l'appréciation subjective.

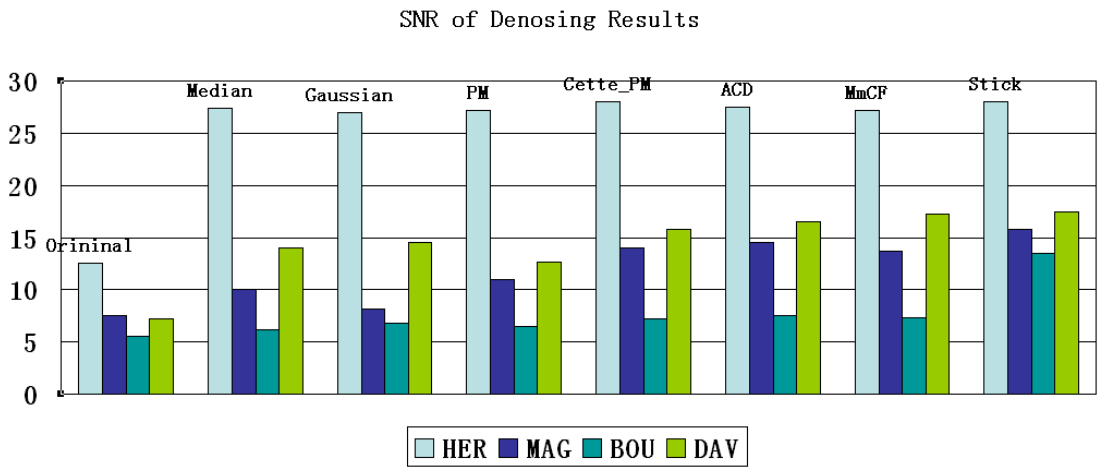

Fig. 4 : rapport signal/bruit (SNR) des images originales et obtenues après débruitage par différents filtres.

B. *Segmentation*

Après l'étape de prétraitement, les différentes méthodes de segmentation (IRG, Stick RG et SES) ont été appliquées aux images in-vivo (IV) et ex-vivo (EV). Nous présentons les résultats obtenus pour chaque patient (HER, MAG, BOU et DAV) en considérant le meilleur volume scanner (phase optimale) du cycle cardiaque

en fin de diastole, lorsque les valvules prothétiques sont fermées. Le premier exemple est représenté par le cas de la bioprothèse péricardique (HER). Grâce à la haute qualité de ces images toutes les méthodes de segmentation donnent des résultats qualitativement similaires et satisfaisants (figure 5).

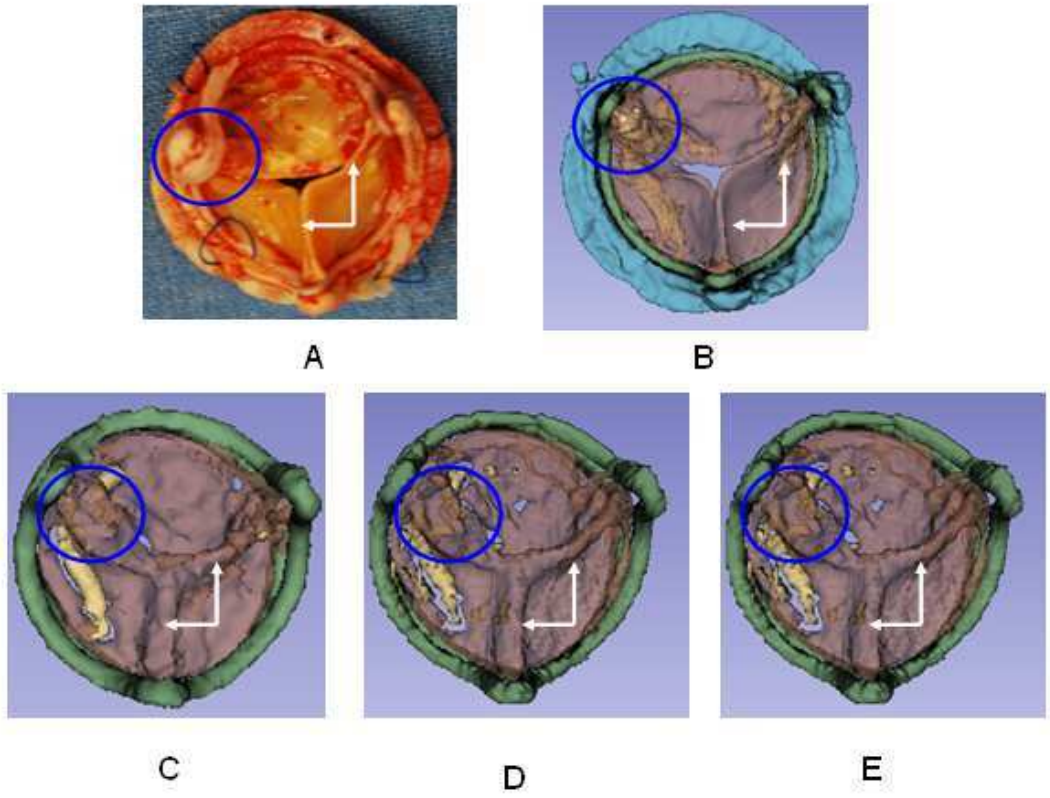

Fig. 5: Visualisation des résultats dans le cas n° 1 - HER. Bioprothèse explantée (A), segmentation des images ex-vivo (B), segmentation des images in-vivo par méthode IRG (C), Stick RG (D) et SES (E). La perte d'une commissure est indiquée avec les cercles bleus et la bonne coaptation des feuillets avec les flèches blanches.

Le deuxième exemple illustre les résultats obtenus dans les deux cas de bioprothèse porcine (BOU et DAV). Bien que les images initiales étaient faiblement contrastées et très bruitées dans la zone d'intérêt, les bords des feuillets semblent bien détectés. Néanmoins, par rapport à la segmentation interactive (IRG), les méthodes basées sur les sticks (Stick RG et SES) ne permettent pas une description complète des feuillets (figure 6).

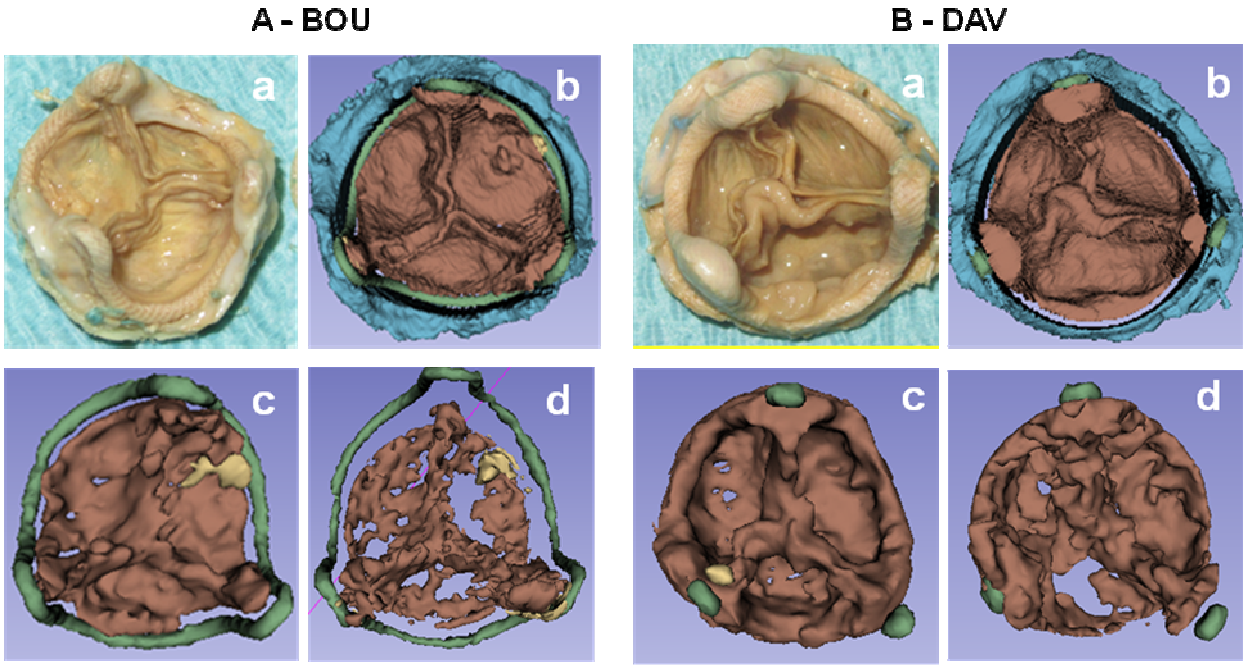

Fig. 6: Visualisation des résultats dans les cas n° 3 – BOU (A) et 4 – DAV (B). Bioprothèse explantée (a), segmentation des images ex-vivo (b), segmentation des images in-vivo par méthode IRG (c) et Stick RG (d).

Au vu de ces résultats (BOU et DAV), nous observons que les feuillets n'étaient pas entièrement segmentés : ils apparaissent avec des trous ou des pièces manquantes. La raison pourrait être liée à la présence de calcifications et à un effet de volume partiel. Pour remédier à ce défaut de segmentation, dans certains cas, on pourrait procéder de la manière suivante :

- segmentation automatique basée sur Stick RG (ou SES) pour décrire les principales composantes de la bioprothèse ;
- segmentation interactive (IRG) pour compléter la description des parties manquantes des feuillets.

Dans le cas 2 – MAG d'une bioprothèse porcine, en raison de la présence de structures à très faible contraste, la segmentation des feuillets était particulièrement

complexe. L'IRG donnait les meilleurs résultats, mais pas entièrement satisfaisants dans ce cas. Une amélioration manuelle à dû être mise en place.

La principale difficulté était dans ce cas le haut niveau de bruit et des frontières entre les structures très peu contrastées (absentes localement). Tous les voxels de valeurs faibles situés dans la ROI ont été classés comme feuillets. En outre, il existe de nombreuses régions incomplètes dans les feuillets.

La visualisation des résultats de segmentation a été réalisée par rendu volumique (figure 7). La présence d'un pannus sous-valvulaire calcifié est caractéristique dans ce cas et responsable de l'obstruction de la valve.

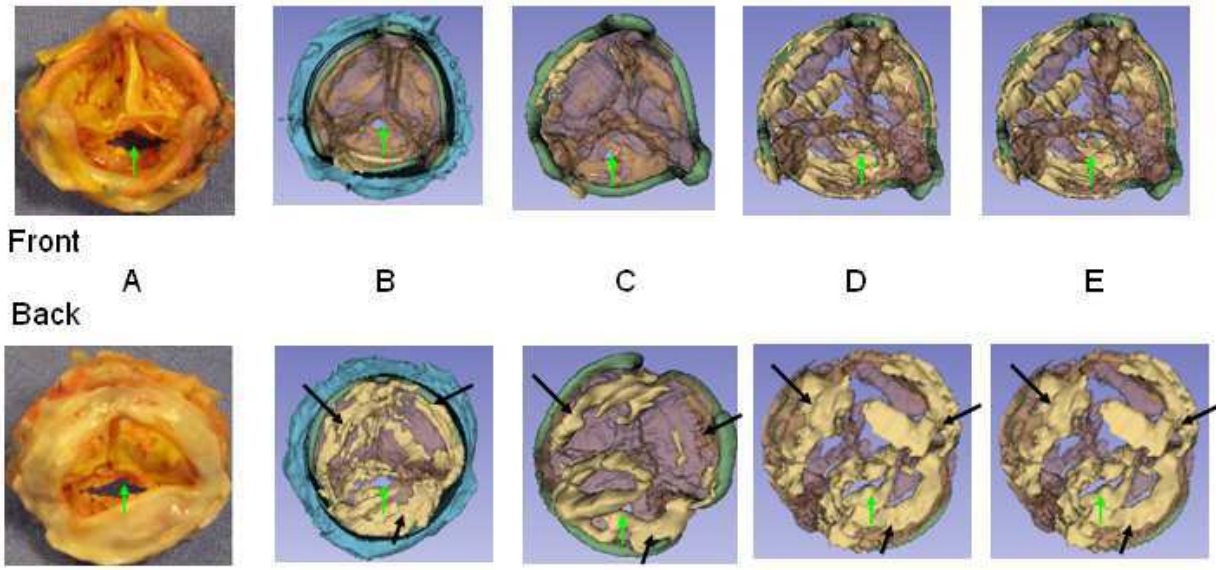

Fig. 7: Visualisation des résultats de segmentation du cas n° 2 - MAG. Bioprothèse explantée (A), images ex-vivo segmentées (B), images in-vivo segmentées par la méthode IRG (C), Stick RG (D) et SES (E). Le pannus calcifié est indiqué par les flèches noires et la déchirure des feuillets par les flèches vertes.

Une analyse volumétrique a ensuite été menée afin de comparer objectivement les résultats obtenus par les trois méthodes sur les images in-vivo (IV) et ex-vivo (EV).

Le critère utilisé pour évaluer les résultats était le volume des composants de la bioprothèse. Les résultats de cette analyse sont présentés en figure 8 (les volumes sont exprimés en mm^3).

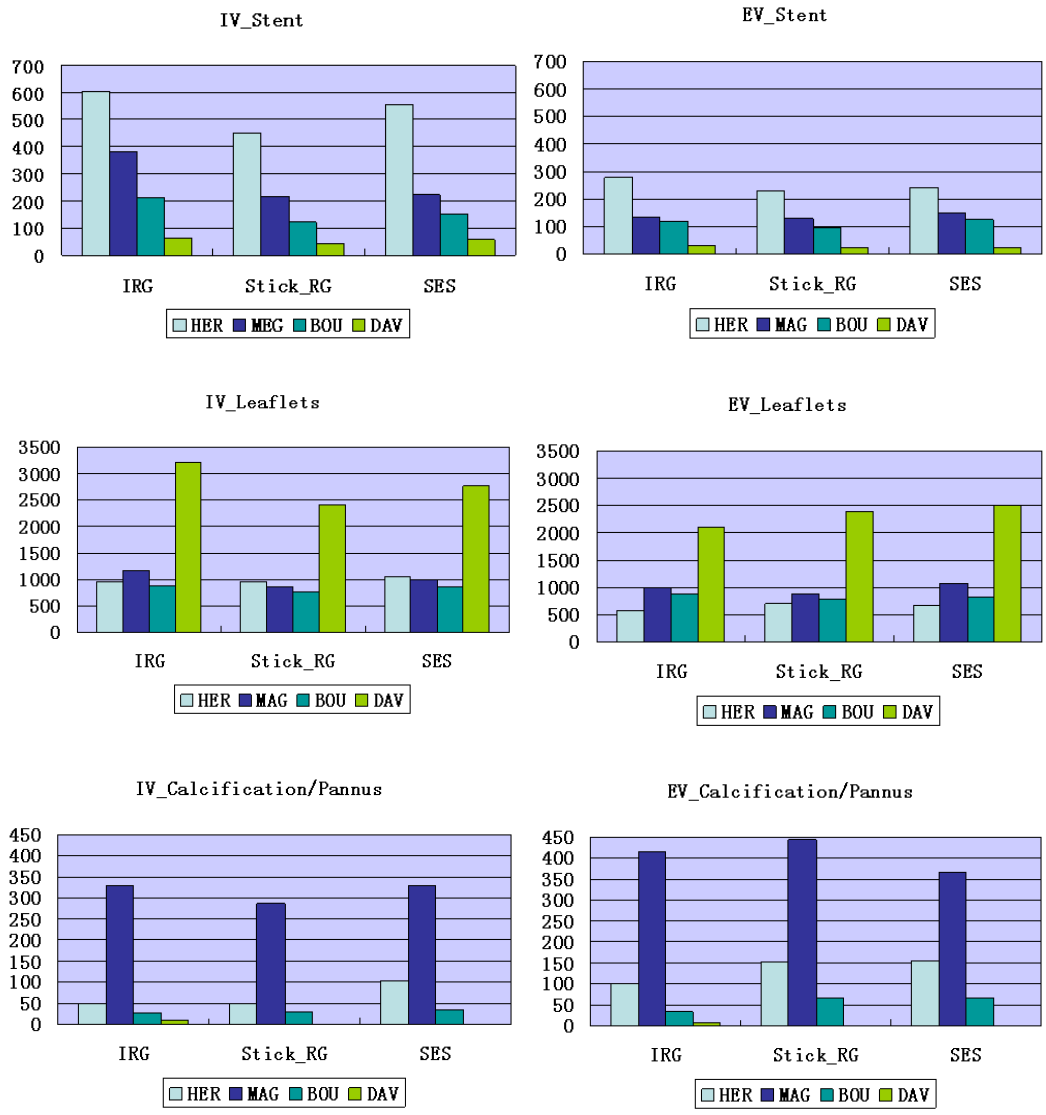

Fig. 8: Analyse volumétrique des composantes des bioprothèses

Une correction de la différence de volume entre les données in- et ex-vivo pour les feuillets prothétiques était envisagée en considérant le stent comme structure de référence. L'estimation du taux de correction permettant de compenser des distorsions pouvant être liés à différents facteurs (mouvement des structures, conditions anatomo-physiologiques in-vivo vs. ex-vivo), pourrait être assimilée à un

étalonnage. L'application de ce taux de correction dans le cas HER semble réduire les différences entre les volumes des feuillets in-vivo et ex vivo (figure 9).

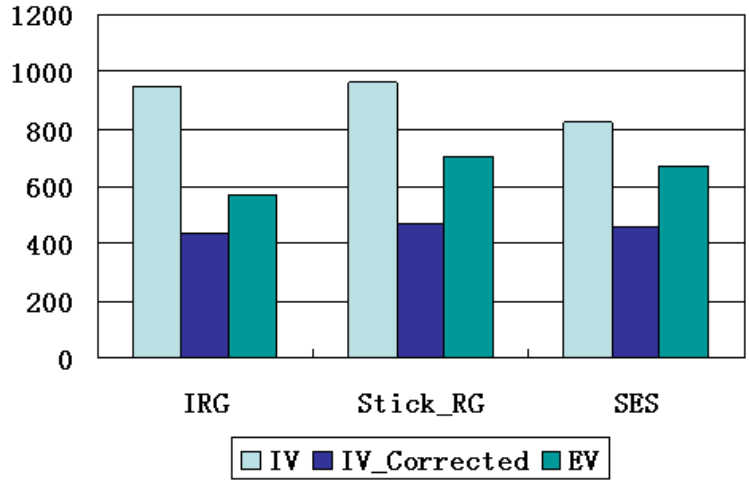

Fig. 9: Application du taux de correction dans le cas n°1.

Dans cette étude, nous avons testé trois méthodes de segmentation par région d'images tomodensitométriques sur des bioprothèses aortiques dégénérées. Ces méthodes, d'approche différente, semblent donner des résultats comparables. Il s'agit de méthodes de segmentation semi-automatique. La méthode IRG nécessite plus d'interaction en comparaison avec les méthodes stick RG et SES.

Le prétraitement des données représente une étape essentielle. En effet, les images tomodensitométriques des bioprothèses doivent être débruitées avant d'être segmentées en raison de la présence de bruit et d'artefacts. Différents filtres ont été testés en vue d'améliorer le contraste des feuillets valvulaires. Le filtre stick, modifié afin d'être appliqué aux images tomodensitométriques, a montré de meilleurs résultats visuels. Cette constatation a été confirmée par les analyses objectives du SNR. Il est à noter que ce processus de filtrage est réalisé par le logiciel MatLab et nécessite un temps de calcul plus importants.

En ce qui concerne les résultats de la segmentation, plusieurs commentaires peuvent être faits. Parmi les images analysées, les meilleurs résultats ont été obtenus dans le cas de la bioprothèse péricardique. La raison en est attribuée en partie à l'épaisseur du tissu valvulaire. En effet, les feuillets valvulaires péricardiques sont plus épais que les feuillets valvulaires d'origine porcine. Des volumes plus élevés ont été observés dans certains composants des bioprothèses in-vivo, en comparaison aux bioprothèses ex-vivo. Plusieurs facteurs expliquent cette différence. En effet, outre le fait qu'il n'existe pas d'acquisition spécifique pour analyser les bioprothèses, la résolution d'image n'est pas la même in-vivo et ex-vivo. Les acquisitions ex-vivo ont été réalisées par un protocole haute résolution afin d'optimiser la qualité des images, alors que les acquisitions in-vivo ont été réalisées par le protocole standard des scanners coronaires couplés à l'ECG. Lors de cet examen, les mouvements cardiaques et la superposition du sang engendrent des différences volumiques non négligeables. Pour faire face à ce problème, nous proposons un facteur de correction qui pourrait représenter un moyen intéressant pour réduire les différences de volume, mais il faudrait le valider à plus grande échelle.

La qualité des images tomodensitométriques des bioprothèses in-vivo tient également à la fréquence cardiaque lors de l'examen. Cette fréquence ne devrait pas excéder les 65-70 bpm. Cependant, les patients peuvent présenter, en pré-opératoire, une tachycardie ou une contre-indication aux bêtabloquants.

Dans tous les cas, nous avons observé dans les images in-vivo une sous-estimation de la dégénérescence des feuillets valvulaires. Ce résultat est à nuancer. En effet, les bioprothèses analysées n'étaient pas, finalement, fortement calcifiées et la dégénérescence était principalement liée à un épaississement valvulaire (difficile à détecter sur les images du scanner).

Notre étude suggère que l'analyse 3D préopératoire des bioprothèses dégénérées est faisable, mais les images CT ont besoin d’un traitement supplémentaire. Une fois améliorées, les images peuvent être segmentées et les reconstructions qui en résultent peuvent aider à visualiser directement la morphologie des feuillets et pourraient jouer un rôle dans la compréhension du mécanisme de dégénérescence des bioprothèses. De plus, ces méthodes arrivent à identifier la présence de calcifications des feuillets ainsi que la présence d'un pannus sous valvulaire.

VI – CONCLUSION ET PERSPECTIVES

L'échocardiographie reste la référence pour l'analyse fonctionnelle des bioprothèses dégénérées. Ces dernières années ont vu naître un intérêt particulier concernant l’analyse morphologique de la valve aortique par images scanner.

Dans cette étude nous avons propose une nouvelle approche pour l’analyse morphologique des bioprothèses valvulaires aortiques dégénérées par segmentation d’images tomodensitométriques. Nos résultats préliminaires suggèrent la possibilité d'améliorer le rehaussement des feuillets bioprothétiques aortiques en appliquant les méthodes de traitement envisagées pour réduire le bruit et segmenter les images scanner préopératoires. Parce qu'à ce jour l’analyse morphologique des feuillets des bioprothèses est complexe voire impossible avec d'autres techniques d'imagerie, nous croyons que dans un avenir proche la segmentation d’images scanner à haute résolution pourrait jouer un rôle important chez les patients ayant une bioprothèse aortique dégénérée pour améliorer la compréhension du mécanisme de dysfonctionnement.

Des études supplémentaires sont nécessaires pour améliorer et valider ces résultats. Sous réserve d'une validation plus poussée des méthodes de traitement d'image proposées, vraisemblablement accompagnée d'une adaptation des protocoles d'acquisition, une analyse de la dégénérescence des bioprothèses pourrait être envisagée sur des séries plus importantes. Il est également important, à notre avis, de caractériser les propriétés mécaniques des feuillets normaux ou dégénérés pour les différents types de bioprothèses. Cela permettrait de créer une base de données de référence. De cette façon, les reconstructions 3D des bioprothèses pourraient

représenter dans un futur proche un outil important pour améliorer la planification de la procédure valve-in-valve ou pourraient être utilisées pour simuler cette procédure endovasculaire en préopératoire (figure 10).

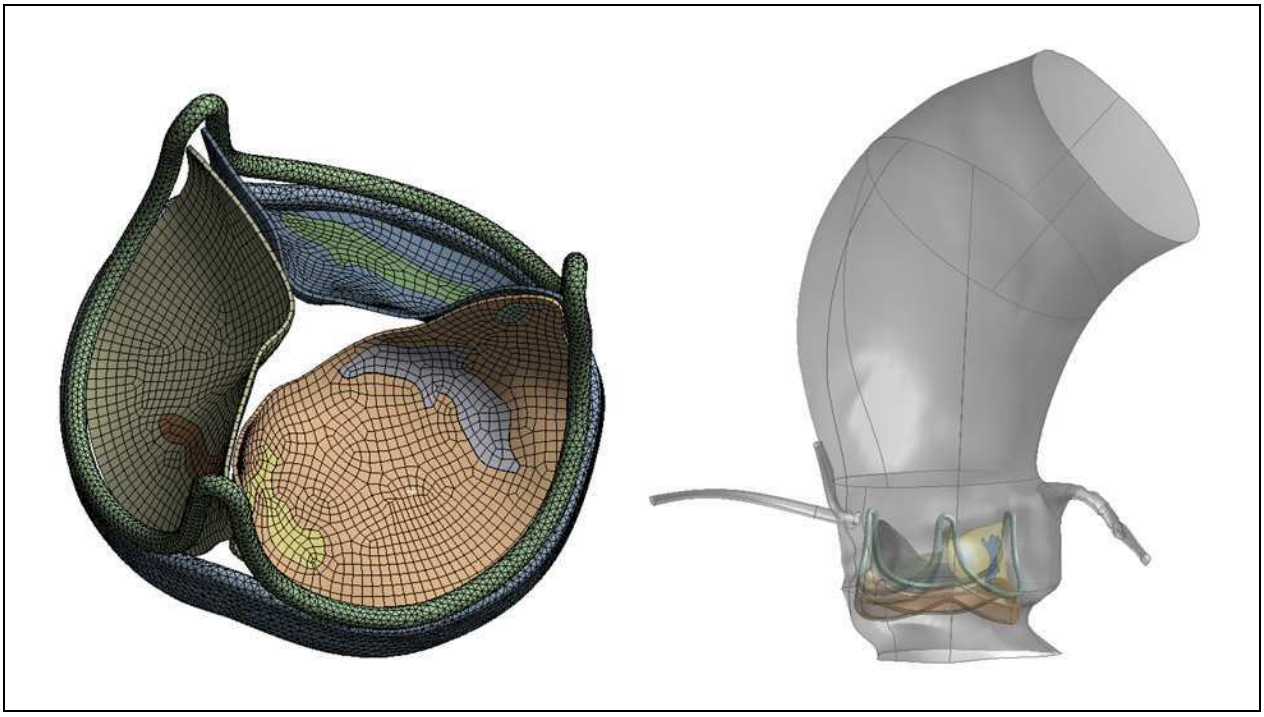

Fig. 10: Maillage décrivant la géométrie de la prothèse valvulaire et les propriétés des tissus (A), ainsi que les structures environnantes (B), dans le cas 1 - HER.

Morphological analysis of degenerated aortic valve bioprostheses by CT scan images segmentation

Abstract

The aim of the study was to assess the feasibility of CT based 3D analysis of degenerated aortic bioprostheses to make easier their morphological assessment. This could be helpful during regular follow-up and for case selection, improved planning and mapping of valve-in-valve procedure. The challenge was represented by leaflets enhancement because of highly noised CT images.

Contrast-enhanced ECG-gated CT scan was performed in patients with degenerated aortic bioprostheses before reoperation (in-vivo images). Different methods for noise reduction were tested and proposed. 3D reconstruction of bioprostheses components was achieved using stick based region segmentation methods. After reoperation, segmentation methods were applied to CT images of the explanted prostheses (ex-vivo images).

Noise reduction obtained by improved stick filter showed best results in terms of signal to noise ratio comparing to anisotropic diffusion filters. All segmentation methods applied to in-vivo images allowed 3D bioprosthetic leaflets reconstruction. Explanted bioprostheses CT images were also processed and used as reference. Qualitative analysis revealed a good concordance between the in-vivo images and the bioprostheses alterations. Results from different methods were compared by means of volumetric criteria and discussed.

ECG-gated CT images of aortic bioprostheses need a preprocessing to reduce noise and artifacts in order to enhance prosthetic leaflets. Stick region based segmentation seems to provide an interesting approach for the morphological characterization of degenerated bioprostheses.

CONTENTS

I – Introduction

During the last decade, the relative use of bioprosthetic aortic valves has clearly increased. Improvements in surgical techniques and valve durability are likely to have fueled this increase. On the other hand, over the last 2 decades, the mortality risk of redo aortic valve surgery has decreased similarly. The operative mortality for an elective redo aortic valve surgery is reported to range from 2% to 7%. Together with the best postoperative quality of life, these good surgical results contribute to the large diffusion of bioprostheses implantation even in younger patients. This phenomenon, associated to the increased life expectancy in industrialized countries, will probably show its consequences in the next years when a large number of elderly patients with associated comorbidities will need a re-intervention for bioprosthesis degeneration. Literature data show that mortality rate can increase to more than 30% in high-risk and non-elective patients. With the introduction of the transcatheter aortic valve to treat native aortic valve stenosis in high or prohibitive surgical risk patients through a less invasive technique, medical community has discovered a seducing but still emergent option to treat bioprosthesis failure in the same kind of patients. In fact transcatheter valve implantation avoids re-sternotomy and cardiopulmonary bypass and can potentially reduce resource utilization by accelerating patient recovery and reducing length of hospital stay. Preliminary results showed that this “valve-in-valve” procedure is feasible, but additional data should be verified to definitively accept this less invasive option. However, even if not yet officially recognized from authorities and manufacturers, the general feeling and the ‘real life’ practice consider this procedure as a potential treatment and multiple small series are going to be reported. Because of the best quality of life for patients after bioprosthetic aortic valve

replacement, cardiac surgeons are implanting today more and more biological devices, even in younger patients, taking into account the possibility of a transcatheter procedure in case of degeneration. Indeed, this “accepted future option” is responsible for a further diffusion of bioprostheses implantation in younger patients with consequent increasing incidence of failure in the next years.

The most frequent failure modality for bioprostheses is represented by leaflet degeneration. The current reference standard for follow-up in patients after aortic valve replacement remains trans-thoracic echocardiography, with trans-esophageal exploration in case of questionable findings at trans-thoracic. Echocardiography represents the gold standard for functional assessment of bioprostheses. However, both trans-thoracic and trans-esophageal echocardiography have limited usefulness for the morphological assessment, especially concerning bioprosthetic leaflets, because of their thickness and the acoustic shadowing from stent or suture ring that often prevents good leaflet visualization. Furthermore, given their two-dimensional imaging nature, it is generally impossible to directly image the leaflets that are not oriented in the imaging plane. Even the new 3D echocardiography has, for the moment, limited application on the aortic bioprostheses also because of the anterior position.

In recent years, multi-detector computed tomography has emerged as a promising tool to provide precise diagnostic information in different clinical situations, such as non-invasive evaluation of coronary disease, ventricular morphology and function and myocardial viability. Multi-detector CT can also help visualize the morphology and motion of native and diseased stenotic aortic valves and precisely measure aortic valve opening areas. Several studies suggest that multi-detector CT can help assess mechanism of dysfunction in mechanical prosthetic heart valve disorders.

Few recent studies have showed that 64 multi-detector CT allows better visualization of the bioprosthetic valve leaflets comparing to echocardiography and that it could play a role in clarifying the mechanism of dysfunction.

In general clinical practice CT scan images normally allow a tridimensional reconstruction of the structures of interest, thanks to their high spatial resolution. The 3D analysis of these images should improve the users understanding and facilitates the planning of surgical/interventional procedures on these structures.

In this context, the starting idea of this research work was that the tridimensional reconstruction of bioprosthetic structures, in particular of prosthetic leaflets, could make easier the morphological analysis of degenerated bioprostheses during normal follow-up and be used for patients' selection, improved planning and mapping of valve-in-valve procedure.

Currently, the available softwares to analyze and process CT scan images do not allow an efficient and effective tridimensional reconstruction of the bioprostheses leaflets because of their thickness. Bovine pericardium and porcine valve leaflets are in fact too thin and CT images are also altered by noise, stent metal artifacts and heart beat. This makes difficult the automatic analysis with available tools and new methods to process these high resolution images have to be considered.

The aim of this study was to assess the feasibility to analyze and morphologically characterize 3D multi-slices CT images of degenerated bioprostheses. Multiple methods for noise reduction and segmentation are available in literature. After a presentation of the most important available approaches, we study and propose methods for noise reduction and segmentation and we compare their results. Moreover we directly confront the morphological findings with an independent

reference standard such as the explanted bioprostheses CT images, processed with the same methods, to validate our results.

II – MEDICAL CONTEXT

2.1 AORTIC VALVE BIOPROSTHESES

Aortic valve replacement represents a standardized and safe operation for the treatment of severe aortic valve disease and, at the same time, one of the most frequent procedures in cardiac surgery. For the Euro Heart Survey on Valvular Heart Disease, that has prospectively collected data from patients with aortic valve disease and treated during the period April-July 2001 in 92 institutions from 25 european countries, the aortic valve stenosis represents the most frequent valve disease (33.9% of total), followed by mitral regurgitation (24.8%) [2.1]. Moreover, in patients with aortic valve stenosis the native valve was replaced by a bioprosthesis in 50% of cases; a mechanical prosthesis was used in 49% of patients. Homograft and autograft represented the 0.6% and the 0.4, respectively. On the contrary, in patients with aortic insufficiency a mechanical prosthesis was mostly used (76.5%), probably because of the younger age of these patients. Observed operative mortality was 3.1% in cases of aortic valve stenosis and 3.4% in cases of aortic insufficiency.

2.1.1 Types of devices

Bioprostheses are generally constituted by animal heterograft (porcine valve leaflets or bovine pericardium). Over the past 40 years, advances in tissue fixation methodology and chemical treatments to prevent calcification have yielded

improvements in the longevity of bioprostheses. All heterograft valves are preserved with glutaraldehyde, which cross-links collagen fibers and reduces the antigenicity of the tissue. Glutaraldehyde also reduces the rate of in vivo enzymatic degradation and causes the loss of cell viability, thereby preventing normal turnover and remodeling of extracellular matrix tissues. Calcification occurs when nonviable glutaraldehyde-fixed cells cannot maintain low intracellular calcium. Calcium-phosphate crystals form at the phospholipid-rich membranes and their remnants, and collagen also calcifies. Glutaraldehyde fixation in porcine valves can be performed at high pressure (60–80 mm Hg), low pressure (0.1–2 mm Hg), or zero pressure (0 mm Hg). Pericardial prostheses are fixed in pressure-free conditions. Porcine prostheses fixed at zero pressure retain the collagen architecture of the relaxed aortic valve cusp. Higher fixation pressures cause tissue flattening and compression with loss of transverse cuspal ridges and collagen crimp. Multiple chemical treatments have been proposed to decrease the calcification process that invariably leads to material failure and valvular dysfunction. These include sodium dodecyl sulfate, polysorbate-80, Triton X-100 and N-lauryl sarcosine, amino-oleic acid, aminopropanehydroxydiphosphonate, toluidine blue, controlled-release diphosphonates, ferric chloride, aluminum chloride, and phosphocitrate.

Today, multiple anti-calcification protocols used to treat bioprostheses are protected by patent. Some examples are the XenoLogix System (Edwards Lifesciences Inc., Irvine, CA) [2.2] and the BiLinx System (St. Jude Medical Inc., St. Paul, MN).

Stented bioprostheses

Stented bioprostheses represent in terms of numbers, the most used biological valvular devices. This subgroup includes valvular devices realized using a rigid artificial structure (stent) including a metallic part that represents the support for the biological tissue (leaflets). First-generation bioprostheses were preserved with high-pressure fixation and were placed in the annular position. They include the Medtronic Hancock Standard and Modified Orifice and the Carpentier-Edwards Standard porcine prostheses, not more used in clinical practice.

Second-generation prostheses are treated with low or zero-pressure fixation. Several second-generation prostheses may also be placed in the supra-annular position, which allows placement of a slightly larger prosthesis in order to reach a best effective orifice area with consequent hemodynamic advantages and lower risk of patient/prosthesis mismatch. These bioprostheses have largely been used in clinical practice (Fig. 2.1); in fact most part of durability data with long term follow-up, up to 25 years, come from the analysis of patients populations having a second generation device [2.3]. Porcine second-generation prostheses include the Medtronic Hancock II and Carpentier-Edwards Supra-annular (SAV) valves. Second-generation pericardial prostheses include the Carpentier-Edwards Perimount and Mitroflow Synergy (Sulzer Carbomedics, Austin, TX) valves.

Fig. 2.1: Second generation bioprostheses.

Third generation prostheses (Fig. 2.2) incorporate zero- or low-pressure fixation with anti-mineralization processes that are designed to reduce material fatigue and calcification. They include the porcine Medtronic Mosaic and St. Jude Epic constituted by porcine aortic valve leaflets mounted into a low profile stent, and the pericardial Carpentier Edward Magna, Sorin Mitroflow and St. Jude Medical Trifecta. The last two bioprostheses are characterized by pericardium mounted externally to the stent in order to obtain a larger effective orifice area with consequent better hemodynamics.

Fig. 2.2: Third generation bioprostheses.

Stentless bioprostheses

Stentless porcine valves (Fig. 2.3) have gained popularity in cardiac surgery due to pioneering work by David at the Toronto General Hospital in 1988 [2.4]. Since they do not have obstructive stents and strut posts, stentless valves provide residual gradients and effective orifice areas that are similar to freehand allografts. Since stentless valves are more difficult to implant and require a longer cross-clamp time, the risks of operation must be matched to a specific benefit the patient may receive with a stentless valve. There is conflicting evidence that the use of stentless valves results in improved left ventricular mass regression over stented bioprostheses. There is also no evidence that incremental improvements in left ventricular mass provide additional clinical benefit. Thus, the routine use of stentless bioprostheses cannot be

recommended for most patients with small aortic roots with the currently available data. At this time, stentless porcine valves are most useful in a relatively younger patient with a small aortic root who is active and likely to be limited by the elevated residual gradient a stented bioprosthesis will create.

Fig. 2.3: Stentless bioprostheses.

The first stentless device used in modern clinical practice was the St Jude Toronto SPV [2.5]. Other devices in this class are represented by the Medtronic Freestyle, the Edwards Prima and the Sorin Solo.

Homografts and autografts

Other substitutes that could be used to replace the aortic valve in some particular cases are the homo- and auto-grafts.

Fig. 2.4: Aortic homograft.

The homograft is represented by a complete cryopreserved human aortic root (Fig. 2.4). It is real tissue transplantation and it is treated to reduce antigenicity before its implantation. After, it doesn't need immunotherapy. Implantation involves not only the diseased valve but also the aortic root with coronary arteries reimplantation, with a consequent increased operative risk comparing to simple aortic valve replacement.

The most important interest is represented by the high resistance to infections that explains their potential use in case of destroying infective endocarditis. Homografts have also been used, during a short time, for aortic root replacement in young patients for their best durability comparing to second generation bioprostheses. However, the best results of third generation bioprostheses together with the

technical difficulties to reoperate the severe calcified degenerated homografts, have contributed to strongly decrease their use in clinical practice.

The autograft is represented by the use of autologous pulmonary root to replace native aortic root. The native pulmonary root is replaced with a homograft (Ross procedure). This operation is limited to few selected cases and represents a rare choice in cardiac surgery for adults.

2.1.2 Bioprostheses durability

The opportunity to discuss in a rational manner and to compare the clinical results obtained by different valve substitutes is based on standardization of definitions of adverse events observed during clinical follow-up of patients. In this regard, it was important the consensus of the scientific community, whose first publication dates back to 1988 (consensus statement of the Society of Thoracic Surgeons, STS, and the American Association of Thoracic Surgeons, AATS) [2.6]. The most recent version of these guidelines for the description of the events of mortality and morbidity in patients with prosthetic heart valves was published in 2008 (Guidelines for reporting morbidity and mortality after cardiac valve interventions) [2.7].

The main limitation to the use of bioprostheses is related to their evolution to the structural degeneration. The appearance of structural valve degeneration exposes the patient to the risks of an evolutionary valvular disease and possibly to the risks related to a reoperation to replace the degenerated bioprosthesis with a new one. This limitation was evident from the earliest historical experiences that have analyzed

the initial valve bioprosthesis; it was also highlighted as the degeneration of the biological valve devices preceded at a higher rate in patients with younger age at implantation [2.8]. It was not possible, however, to clarify the mechanisms underlying this phenomenon, whereas the available evidence may contradict this observation. It was also pointed out that while the overall survival at 10 years after surgery is substantially comparable between patients who received a bioprosthesis and those who received a mechanical prosthesis [2.9], from the fifteenth year post-surgery it is possible to experience reduced survival free from valve-related adverse events in patients who received a bioprosthesis, because of the impact of structural degeneration [2.10]. These findings are generally valid regardless of the bioprosthesis model analyzed. In many series previously published survival after aortic valve replacement is assessed between 80% and 85% at 5 years, between 65% and 75% at 10 years, and between 45% and 55% at 15 years [2.10-2.12]. This difference remains evident despite the higher incidence of bleeding events in patients who received a mechanical prosthesis as a result of oral anticoagulant therapy. This observation highlights the epidemiological importance of structural degeneration of the bioprosthesis, despite the continuous progress in anti-calcification treatments. However, it was shown that a number of additional patient-related instead of prosthesis-related factors have an impact on clinical outcomes at long-term follow-up after aortic valve replacement. Among these, the coexistence of coronary artery disease and a sub-optimal functional state at the time of surgery are independently associated with reduced survival at 10 years after surgery [2.13-2.16]. Additional variables that were associated with less flattering clinical outcomes are the coexistence of nephropathy or atrial fibrillation and the female gender. In a large study [2.17] has been reported that the causes of death related to the prosthesis

justify the 41% of deaths reported at 15 years follow-up among patients with bioprostheses, although this data should be interpreted considering that it includes also the number of deaths from unknown cause. A proportion of these unknown deaths may be unlikely to actually be considered in relation of cause and effect with the valve prosthesis. On the other hand, the cardiac deaths not prosthesis-related justified the 21% of deaths in the same follow-up of patients with bioprosthesis. This observation has to be compared with the respective values of 37% and 17% observed in patients with mechanical prostheses[2.17].

It should be noted as in the study of long-term clinical results of valvular bioprosthesis, in which the frequency of non-fatal adverse events related to the prosthesis becomes important (in particular structural degeneration), the statistical methodology through which these data are processed acquires greater importance. In fact, the actuarial method (also known as Kaplan-Meier) determines a pessimistic assessment for individual patients in relation to clinical variables related to the prosthesis. In fact, the number of deaths during follow-up due to non-cardiac causes will mask the true incidence of non-fatal events related to the prosthesis (such as structural degeneration and related reoperation) [2.18-2.19]. This effect is much more pronounced the longer is the duration of follow-up after implantation of the bioprosthesis. In order to predict, in individual patients, the risk of developing a degeneration of the bioprosthesis as a function of patient's life expectancy at the time of surgery, and then in order to decide on the basis of evidence the opportunity to implant a bioprosthesis rather than a mechanical prosthesis, it is therefore preferable to consider the "actual" methodology, or cumulative risk. On the other hand, this methodology would be inadequate to compare the clinical results of two different

bioprosthesis (actuarial methodology is best for this purpose) [2.20-2.21]. In other words, the difference between the results obtained using the two methods will be smaller the higher is the frequency of the 'non-fatal' events (structural degeneration, reoperation) as cause of death at follow-up, or the higher is the frequency of deaths from unknown causes (which are counted as valve-related deaths). These methodological approaches are therefore complementary (the one useful for determining the valve prosthesis “destiny” and the other to determine the patients “destiny”).

2.1.3 Mechanisms of bioprosthesis failure

Time-related structural valve dysfunction leading to regurgitation or stenosis is the major drawback of bioprosthetic valves. Fortunately, the vast majorities of valve failures are nonfatal and progress slowly; if identified in a timely manner, an elective redo surgery can be performed with relative safety. Structural valve dysfunction is age-dependent. In fact, it is nearly uniform by 5 years in patients younger than 35 years of age, but occurs in only 10% in those older than 65 years of age within 10 years.

Failure modes can be influenced by: 1) host metabolic pathways; 2) bioprosthesis engineering and chemistry (e.g., leaflet suturing material, stent post flexibility, prosthesis fabric covering, leaflet fixation process); and 3) mechanical loading effects (e.g., leaflet flexural stress/strain).

Broadly speaking, bioprosthetic valve failure can be the result of calcification, wear and tear, pannus formation, thrombosis, and/or endocarditis (Fig. 2.5).

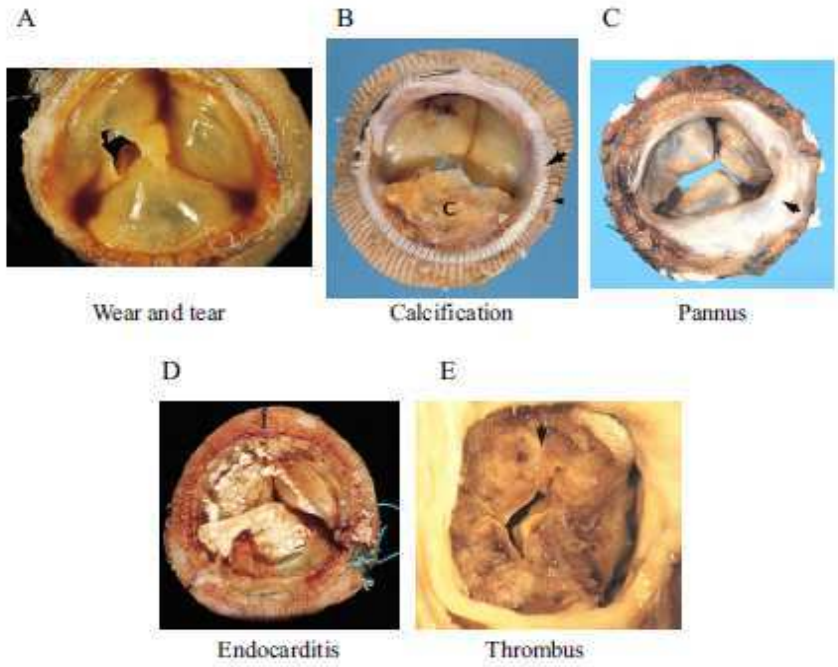

Fig. 2.5: Mechanisms of bioprosthesis failure.

Leaflet tissue deterioration, whether calcific or non-calcific, is the major cause of bioprosthetic valve failure [2.22-2.25]. Although the glutaraldehyde fixation process of bioprosthetic heart valves is intended to promote tissue durability by creating stable cross links between collagen fibers and render the heterograft material biologically inert, residual glutaraldehyde-derived polymers may serve as calcium-binding sites that promote calcium-phosphate precipitates. Furthermore, toxic glutaraldehyde may result in cell death of bioprosthetic valve leaflets and host fibroblasts/macrophages. The mitochondria of dead cells, rich in phosphate, can be an additional source of calcium-binding sites. For these reasons, anticalcification treatments (e.g., Edwards ThermaFix, Medtronic AOA) serve to reduce potential binding sites by: 1) residual glutaraldehyde substraction, 2) phospholipid extraction; and/or 3) terminal liquid sterilization. Calcific deposits have a propensity to develop in areas where leaflet

flexion and stress are greatest: at the basal and commissural attachment points. Approximately three-fourths of patients with leaflet calcification and tears suffer from aortic regurgitation [2.22-2.25]. The presence of calcification is a common finding in explanted bioprosthesis, especially in the first and second generation devices. Schoen and colleagues proposed a classification of bioprostheses calcifications (Tab. 2.1) [2.26-2.27].

Tab. 2.1: grading of calcification in bioprostheses degeneration.

Grading of Calcification (Shoen et al.)	
Grade 0	No calcification
Grade 1	Small, isolated calcific nodules
Grade 2	Moderate, patchy nodules up to 1mm in length
Grade 3	Severe nodules up to 2 mm in length
Grade 4	Very severe, diffuse nodules capable of puncturing through the cusp surface

Leaflet tears represent a very frequent failure modality. Even for this type of lesion a classification has been proposed (Tab. 2.2) [2.28].

Tab. 2.2: grading of tears in bioprostheses degeneration.

Grading of Tears (According to Ishihara et al.)	
Type I	Linear tears involving the free edge of cusp
Type II	Linear tears running parallel to the sewing ring, along the basal regions of cusp
Type III	Large round or oval perforations occupying the central regions of the cup
Type IV	Small and multiple pinhole like fenestrations in the cusp

The prolapse of one or more valve leaflets is considered by some authors as a specific lesion, while others will consider it as a consequence of a leaflet tear. However, the prolapse consists in the excessive movement of one or more valve leaflets toward the outflow of the left ventricle. The lesion determining the prolapse can be an important vertical tear of the leaflet free edge or a disconnection of the leaflet from its suture line on the stent (Fig. 2.6).

Fig. 2.6: leaflet tears in degenerated porcine bioprosthesis.

Pannus represents a host tissue response and develops at the host-prosthesis interface. Early pannus is composed of myofibroblasts, fibroblasts and capillary endothelial cells. Overtime pannus may calcify. Some pannus formation over the suture is normally expected and functions to form a non-thrombogenic surface. When exuberant, however, it may extend to the leaflets and contribute to leaflet stiffening and dysfunction. Pannus formation is usually mild and can be detected in the vast majority (~70%) of explanted valves.

A classification has also been proposed for this type of lesion (Tab. 2.3) [2.29]; according to this classification, only in the two last grades (a pannus which extends for more than 2 mm inside the effective orifice area) will result in significant hemodynamic effects and may result in valve dysfunction.

Tab. 2.3: grading of pannus in bioprostheses degeneration.

Grading of Pannus (Modification from Butany et al.)	
Grade 0	No pannus
Grade 1	Mild and involving part of the circumference of the valve ring
Grade 2	Moderate and extending up to 2 mm onto the surface of the cusp
Grade 3	Severe and extending beyond 2 mm of onto the surface of the cusp
Grade 4	Very severe and surrounding the flow and nonflow surfaces of the cusp, causing the cusp to shorten

It should be noted that a mild pannus can be virtually observed in all bioprostheses after the first year post-implantation. It has been suggested also a temporal correlation with the anatomo-pathological grade of pannus. In fact, in a series of explanted pericardial bioprostheses (Carpentier-Edwards Perimount) [2.29], the prostheses presenting a pannus grade 1 were implanted 4.4 years before, while valves showing a pannus grade 2 were implanted 9.1 years before. A similar period of time had elapsed between the implant and the evidence of pannus grade 3 or 4. This suggests that the operating time of the valve is not sufficient to justify the size of the pannus overgrowth. Some additional factors are involved in the pathogenesis of the pannus (probably hemodynamic, metabolic and immune) and these factors vary from patient to patient and realize the differences between the various cases. These mechanisms, however, remain largely unknown.

Some authors have previously attempted a comparison of the failure mode between two different pericardial bioprostheses, in particular the Carpentier-Edwards Perimount and the Ionescu-Shiley [2.29-2.30]. Results showed that calcifications and pannus formation were more frequent and evident in the first model, on the contrary in the second was more frequent the presence of leaflets tears as mechanism of structural degeneration requiring valve reoperation. These observations suggest that small differences in the design of different prosthetic patterns, in the distribution of hemodynamic stress and in the anti-mineralization treatments can significantly influence the modality of structural degeneration from one model to another.

Thrombosis and endocarditis occur less frequently than the aforementioned modes of bioprosthetic failure, occurring at a rate of 0.2% per year and 1.2% per year, respectively [2.31]. They represent usually sub-acute or acute failure modalities and they need a rapid treatment comparing to other leaflets failures.

During *infective endocarditis* a microorganism colonizes the bioprosthesis producing fever, heart murmur, splenomegaly, embolic manifestations, and bacteremia or fungemia. Early diagnosis of this condition is extremely important because it almost invariably leads to devastating complications and death if not treated properly.

Prosthetic valve thromboembolism is a complex phenomenon, occurring through an interaction between prosthesis type and patient-related factors. The pathologic events leading to thromboembolism start immediately after surgery. Damaged paravalvular tissue and deposition of fibrinogen on the valve surface activate platelets as soon as blood starts flowing across the valve leading to immediate platelet adhesion and aggregation. Within 24 h after surgery, platelet deposition on the Dacron sewing ring can be imaged radiographically however, these platelets are highly sensitive to shear forces and they are prone to continued activation and

destruction. Also coagulation factors are activated after valve implantation, leading to further clot formation. This is inherent to the thrombogenicity of the prosthetic material (suture material, Dacron sewing ring, struts and hinge points) and sites of debrided tissue (valve excision site). Trans-prosthetic turbulent flow leads to regional increase in shear stress, structural damage of the endocardium and causes a loss of local resistance to thrombosis. Turbulent areas on the outflow side of the prosthesis create flow stagnation, trapping damaged platelets and activated factors. This provides an ideal substrate for thrombus formation and subsequent embolization. Thrombin can also be formed on platelet membranes after their activation, further promoting the organization and growth of platelet fibrin thrombus.

It is important to remember that micro-thrombus formation, immediately after surgery, can be responsible for early degeneration and calcification of bioprosthetic leaflets. Adequate postoperative anti-thrombotic management is mandatory but currently a common guideline doesn't exist [2.32].

2.2 REOPERATIVE AORTIC BIOPROSTHESIS SURGERY

2.2.1 Low or high risk procedure?

In the past, there were only a few generally accepted indications to use a bioprosthesis for primary, isolated aortic valve replacement: (1) the presence of well-established contraindications to continuous anticoagulation, (2) the inability to monitor prothrombin levels adequately, and (3) patients whose survival was limited and more dependent on non-valve–related issues [2.33-2.34]. In recent years, however, the use of biologic valves in the aortic position has become more common [2.35-2.36]. As mentioned earlier, reoperations are technically demanding, and many patients present in a poor functional state that further increases their mortality, in some series up to 19% [2.37-2.39]. Generally speaking, optimal planning for reoperation prior to deterioration to NYHA class III–IV levels and before unfavorable comorbid conditions have arisen is imperative to ensure good outcomes [2.40]. Following these guidelines in the modern era, elective re-replacement of malfunctioning aortic bioprostheses can be performed with results similar to those of the primary operation [2.33, 2.41-2.42]. In 2005 the Mayo Clinic, for example, reviewed its experience with 162 reoperative aortic valve replacements (AVRs). Early mortality for reoperative AVR was not statistically different from that for primary AVR [2.43]. In light of recent lower operative mortality in reoperative valve surgery, a more conservative approach toward issues such as "prophylactic" AVR in patients with asymptomatic mild to moderate aortic stenosis at the time of coronary artery bypass grafting (CABG) also may be more appropriate [2.44].

In evaluating the reoperative patient, the presence of concomitant coronary artery disease and pulmonary hypertension has been shown consistently to be independent risk factors [2.33]. Patients with these risk factors therefore need careful surveillance once the probability of bioprosthetic dysfunction begins increasing (6 to 10 years after implantation). Regarding valve surveillance and timing of reoperation, the following variables are relevant to the clinical management of patients with an aortic bioprosthesis: a history of endocarditis prior to the first operation, perioperative infectious complications, coronary artery disease acquired after the first operation, an increase in pulmonary artery pressure and a decrease in left ventricular function during the interoperative interval [2.33]. Proper timing of the reoperation therefore is paramount because duration of clinical signs with a dysfunctional aortic bioprosthesis may be misleading. This is further supported by the fact that the need for emergency reoperation is the most ominous risk factor and consistently yields a high early mortality rate of 25 to 44% [2.45].

Reoperation after homograft/root/allograft

Aortic valve replacement with homografts and autografts was performed increasingly because of excellent freedom from thromboembolism, resistance to infection, and reasonable hemodynamic performance [2.46]. While improved durability of current tissue valves has slowed this trend, autografts and, to a lesser degree, homografts remain popular in younger patients owing to durability and, in the case of autografts, the potential for growth [2.47-2.48]. Consequently, many patients will require aortic valve re-replacement for structural degeneration of their homograft or autograft valve [2.49]. It is expected that about one-third of patients younger than 40 years of age will require aortic valve re-replacement within 12 years of homograft placement. This is due primarily to calcification and structural valve degeneration. As such, the issue of

homograft or autograft durability is particularly pertinent in this subgroup of younger patients who are expected to live beyond 15 years from time of operation.

The incidence of patients with homografts or autografts in need of a second valve operation is expected to increase owing to the aforementioned recent popularity and availability of these conduits. Also, there is varied opinion as to the optimal surgical method of primary homograft AVR, with increased rates of aortic insufficiency in patients with the subcoronary implantation technique. Importantly, the selected technique of primary homograft operation may have relevance at reoperation because calcification or aneurysmal dilatation of the homograft may pose surgical challenges at reoperation. Despite these challenges, Sundt and others [2.50-2.52] have documented the feasibility of aortic valve re-replacement after full-root replacement with a homograft. How to best approach the reoperative root scenario and which valve to reimplant, however, have been debated. At one extreme, Hasnet and colleagues documented the results of 144 patients who underwent a second aortic homograft replacement with a hospital mortality rate of only 3.5% [2.49]. Although Kumar and colleagues, in a multivariate analysis of reoperative aortic valve surgery, did not show that a previous homograft added significant risk [2.53], the technical aspects of reoperative AVR in this patient population consistently have been found to be challenging owing to the heavy calcific degeneration that invariably occurs. With this in mind, and owing to the typical absence of the need for a second root operation, a more simplified approach to reoperative aortic valve surgery in patients with previously placed homografts may be optimal [2.54]. This simplified approach consists to perform aortic valve re-replacement using a mechanical valve or, less commonly, a stented xenograft while reserving a second homograft and root

operation for specific indications such as endocarditis, associated root pathology, or a very young patient with contraindications to a mechanical valve.

Homograft re-replacement nonetheless is performed but is much less common, and hospital mortality varies widely across many centers, ranging between 2.5% and 50% [2.50-2.52]. David and colleagues, for example, reviewed their experience with root operations in 165 patients who previously had undergone cardiac surgery. Of these, 28 had a previous root operation. Overall, 12 operative (7%) and 20 late deaths (12%) occurred [2.55]. Variations in sample size, valve selection, surgical techniques, and patient factors, as well as the experience of the surgeons, may account for these wide differences.

2.2.2 Surgical technique

Prior to proceeding with a resternotomy, the relationship between certain anterior mediastinal structures (e.g., the right ventricle and the aorta) and the posterior aspect of the sternum must be assessed carefully. This generally can be visualized on chest radiograph or more accurately with a computed tomographic (CT) scan. It has been shown that multidetector computed tomographic (MDCT) scanning, in combination with retrospective electrocardiographic gating, can be used as a noninvasive way to assess not only the heart's location in relation to the sternum but also graft location and patency (Fig. 2.7) [2.56-2.58].

Fig. 2.7: preoperative CT scan showing patent LIMA graft (A) and aortic pseudo-aneurysm in contact with sternum (B).

Exposure of the femoral vessels and preparation for emergency femoral-femoral cardiopulmonary bypass should be considered prior to resternotomy. In selected cases of heightened concern for right ventricle–graft injury or in cases in which a left internal mammary artery (LIMA) graft is patent, the surgeon should consider the use of cardiopulmonary bypass prior to chest reentry. Sternal wires from the previous operation should be undone carefully but left in place as a safeguard during initial sternal division. An oscillating bone saw can be used to divide the anterior sternal table. Following this, bilateral pleural spaces should be entered inferiorly, followed by careful dissection of other mediastinal structures. The pericardial dissection plane can be developed by starting at the cardiophrenic angle and advancing slowly cephalad and laterally on the surface of the right side of the heart. Cephalad dissection should start with freeing the innominate vein prior to spreading the retractor to avoid its injury. Further dissection then is carried down to the superior vena cava, being careful to note the location of the right phrenic nerve. An area of consistently dense adhesions is the right atrial appendage, and caution should be used here. In addition,

great care should be taken to avoid "de-adventializing" the aorta. The area where the aorta apposes the pulmonary artery is another site of potential injury.

Repairing small ventricular or atrial lacerations should not be attempted before releasing the tension of the surrounding adhesions. Repair of great vessel injuries or severe right ventricle injuries is best done under cardiopulmonary bypass. Active hemorrhage during a second sternotomy usually is due to adherence of the heart or great vessels to the posterior sternum. Of note, prior use of a right internal mammary artery (RIMA) graft can be particularly challenging because it frequently crosses the midline, and extreme caution must be used in first dissecting out this vessel. When major hemorrhage does occur on sternal entry, attempts at resternotomy should be abandoned, and the chest should be reapproximated by pushing toward the midline. The patient should be heparinized immediately while obtaining femoral arterial and venous cannulation. Blood loss from the resternotomy should be aspirated with cardiotomy suction and returned to the pump. Once bypass has been established, core cooling should be commenced with anticipation of the need for circulatory arrest. Once cool, flow rates can be reduced, and the remaining sternal division can be completed, followed by direct repair of the underlying injury. Anticipating the possibility of this scenario, exposition of peripheral cannulation sites prior to beginning a resternotomy should be considered. In cases of heightened concern for right ventricle or graft injury, or in patients with a patent LIMA to left anterior descending (LAD) artery graft, cardiopulmonary bypass and cardiac decompression may be initiated prior to sternal reentry. After safe sternal entry, the patient may be weaned from bypass for further dissection of adhesions to avoid prolonged pump times.

After aortic cross-clamp and aortotomy, the valve prosthesis is excised with sharp dissection. Care must be taken to remove all sutures and pledgets from the annulus. Annular injuries caused while excising the prosthesis are carefully repaired.

In all repeat aortic procedures, rigorous myocardial protection must be applied because these procedures often have longer ischemic times. Antegrade cold blood cardioplegia is usually employed throughout the case by selective cannulation of the coronary ostia.

2.2.3 Reoperation for bioprosthetic structural deterioration

The basis for the progressive improvement of the results in aortic valve reoperation is represented by the application of narrower surveillance protocols and the indication for reoperation in an earlier evolution stage of pathology before general clinical deterioration. This approach is particularly well applicable to patients undergoing aortic valve replacement with a bioprosthesis; in such patients structural degeneration and subsequent functional impairment (stenosis, insufficiency or steno-insufficiency) are generally developed in a slowly progressive way, thus allowing an effective periodic monitoring and an elective planning of reoperation.

In such conditions, the risk of surgical replacement of a degenerated bioprosthesis is currently similar to the risk associated with a first surgery for aortic valve replacement [2.59-2.60]. Interestingly, in several studies the execution of the reoperation in late represented an independent factor of increased operative mortality. In a series of 162 reoperations on the aortic valve realized in the time period between 1993 and 2001, it was observed an operative mortality of 5%, not significantly greater ($p = 0.2$) when compared to the 3% of mortality after primary aortic valve replacement during the

same period [2.61]. This study confirmed that prosthetic endocarditis, advanced NYHA functional class, impaired systolic function of the left ventricle and peripheral vascular disease were independently associated with mortality. Another recent series of valve reoperation confirmed these concepts and reported an overall operative mortality of 3.8% [2.62].

These results are indeed support for an expansion of the use of aortic bioprostheses in younger patients. This conclusion assumes greater importance if we consider that for choosing between a biological and mechanical prosthesis, the risk of structural degeneration of the bioprosthesis and the risk of reoperation due to this complication should be assessed primarily. Mortality for prosthetic endocarditis, known to be higher, should not be considered in the calculation of mortality from reoperation for structural degeneration.

Looking at literature, there are not available studies about patients undergoing reoperation on aortic bioprosthesis comparing the operative mortality according to the different indications for reoperation (structural degeneration, non-structural dysfunction or infective endocarditis). For this purpose, in our Department of Cardiovascular and Thoracic Surgery, a retrospective study specifically designed to answer this question has recently been conducted [2.63]. In this study, a population of 164 patients undergoing reoperation on aortic bioprosthesis at our institution from 1980 to 2011 was stratified according to the class of indication for reoperation as previously specified: structural degeneration (94 cases, 57.3%), non-structural dysfunction (34 cases, 20.7%) or infective endocarditis (36 cases, 22%). While the operative mortality observed in the whole population was 10.9%, the observed mortality in the subgroup of patients undergoing reoperation for structural degeneration was significantly lower (8%) in comparison to both other subgroups

(endocarditis and non structural dysfunction). In addition, the rate of major perioperative complications (stroke, myocardial infarction, cardiogenic shock) was significantly higher in patients undergoing reoperation for infective endocarditis ($p = 0.006$). To emphasize that these three classes of indications for reoperation correspond basically to three different patients profiles, the analysis of follow-up (mean follow-up of 8.2 ± 5.8 years for a total of 1110.4 patient-years) has shown that patients reoperated for structural degeneration were characterized by a significantly higher long-term survival comparing to the other classes ($p = 0.0002$, Kaplan-Meier stratified analysis).

Moreover a further study was recently conducted at our institution on the SVD subgroup (81 patients) with the purpose to ascertain and compare the performance of the most common scoring systems for the prediction of operative mortality in patients undergoing reoperation for structural degeneration of aortic bioprosthesis. In this study we also addressed the mechanisms of bioprosthetic failure observed after valve explantation, in order to determine the prevalence of conditions which may jeopardize the efficacy of the Valve-in-Valve procedure. Our data indicate mild but consistent superiority of the EuroSCORE II in this peculiar population comparing to EuroSCORE I and STS Score. In addition, after intra-operative evaluation, we reported a considerable rate of bioprosthetic failure mechanisms which had not been revealed by preoperative imaging: significant subvalvular pannus (4.9%), association of significant pannus and leaflet tear (13.6%), isolated valve thrombosis (2.5%), association of valve thrombosis and significant pannus (1.2%), paravalvular leakage (2.5%) and bioprosthetic stent torsion causing malcoaptation of leaflets (1.2%). Thus, up to 25.9% of patients included in our series carried at least one misdiagnosed mechanism of bioprosthetic dysfunction.

This study emphasizes the issues of reliability of standard imaging in clarifying the presence of mechanisms which either would not be corrected by the valve-in-valve procedure or may lead to procedural failure.

2.3 VALVE-IN-VALVE PROCEDURE

Although, as described above, the risk of reoperation of bioprosthesis is gone considerably decreasing during the last few years (down to 2% of reported operative mortality), on the other hand it is known that the mortality rate can reach up to 30% for patients at high surgical risk because of multiple co-morbidities and non-elective conditions.

Already used for the treatment of patients with native aortic valve stenosis and considered at excessive surgical risk, the TAVI procedure (Transcatheter Aortic Valve Implantation) has been proposed for use in the context of the bioprosthesis degeneration in patients similarly considered at excessive operative risk.

Such a procedure (called Valve-in-Valve) provides for the implantation of a transcatheter valve within the degenerated bioprosthesis already in place, which is therefore not removed but, similarly to what happens in the TAVI procedure for the native aortic valve, constitutes the support for the transcatheter valve (Fig. 2.8).

Fig. 2.8: Edwards Sapien transcatheter valve deployed into a bioprosthesis.

This procedure is still not yet recognized as indication by the producers of the transcatheter valve devices and by regulatory authorities of the United States of

America. Currently, the major manufacturers of transcatheter valve (Edwards Inc. and Medtronic Inc.) have applied to obtain the CE mark for the Valve-in-Valve procedure; for this purpose clinical trials are in progress in order to verify the reproducibility and the safety of this procedure in sufficiently large series of patients. The first clinical experiences have demonstrated the technical feasibility.

In 2007, Wenaweser et al. [2.64] reported the first case of a transcatheter valve implanted into a degenerated surgical aortic bioprosthesis using a Medtronic CoreValve system (Fig. 2.9).

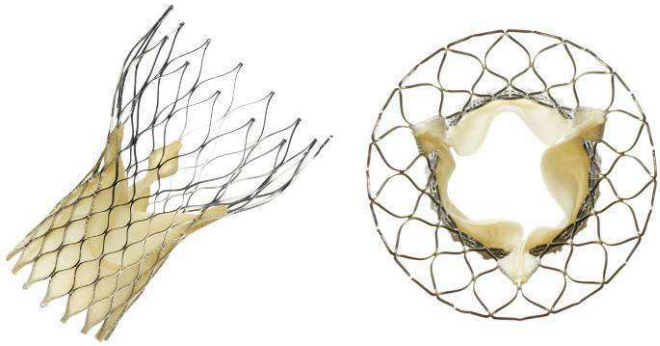

Fig. 2.9: Medtronic CoreValve transcatheter valve.

Since then, numerous case reports have been described also with the use of the other available device Edwards Sapien (Fig. 2.10) and through different accesses as trans-femoral, trans-apical and trans-axillary [2.65-2.73].

Fig. 2.10: Edwards Sapien transcatheter valve.

2.3.1 Technical aspects

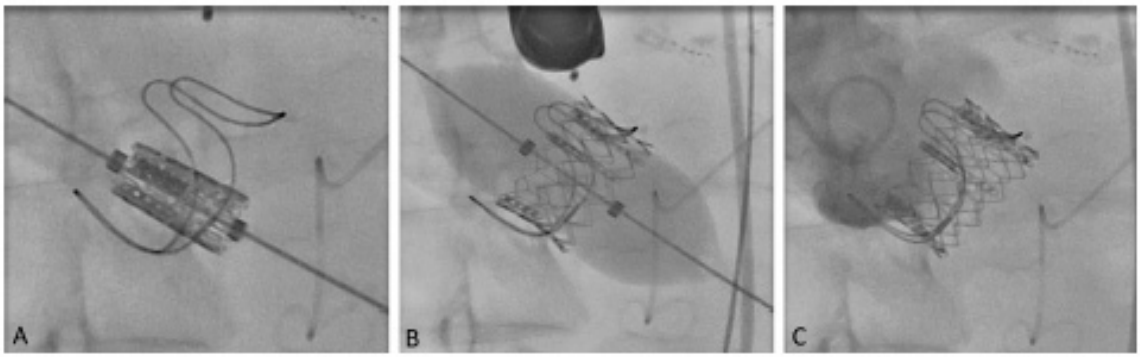

Fig. 2.11: valve-in-valve procedure using Edwards Sapien transcatheter valve. Intraoperative fluoroscopy during (A) device positioning, (B) valve deployment and (C) control aortography.

For the planning and implementation of the Valve-in-Valve procedure (Fig. 2.11), the assessment of exact dimensions and mechanical characteristics of the degenerated bioprosthesis inside which we intend to expand the transcatheter prosthesis is foundamental. In a stented bioprosthesis we can distinguish the external diameter (A) from the internal diameter (B) of the stent and from the diameter of the suture ring (D), as shown in Figure 2.12.

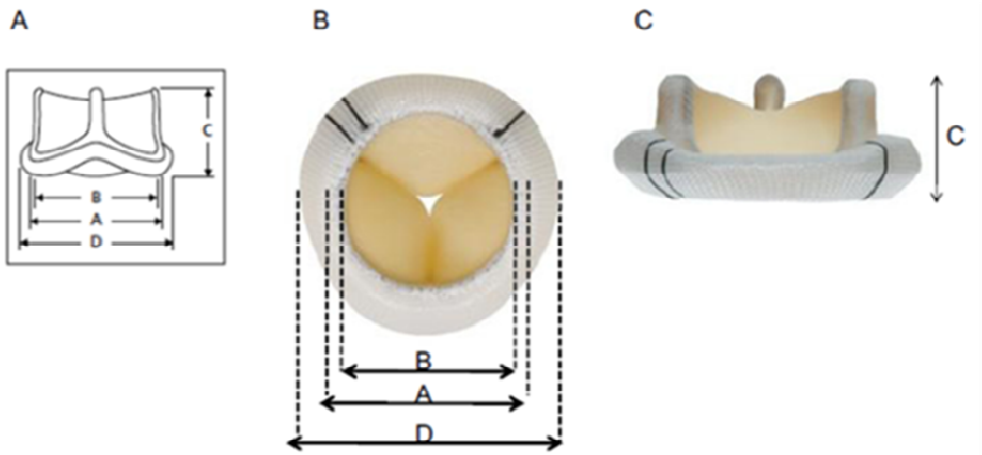

Fig. 2.12: bioprosthesis different diameters can change according to valve type.

It is evident that the internal diameter of the stent has the greater importance for the size selection of the transcatheter prosthesis to implant. However, the diameter in millimeters supplied by producers of bioprostheses is not adequate for this purpose, since it generally refers to the external diameter of the stent. In addition, the criteria to define the size of the bioprostheses vary between different manufacturers.

Available preoperative radiological study, carried out either by multislice CT or by high definition echocardiography acquires a fundamental role. These imaging modalities allow to accurately measure the diameter of the landing zone of the transcatheter prosthesis. Currently, conversion tables are available to facilitate the choice of the size of the transcatheter valve starting from the internal diameter of the stent in different models of bioprosthesis (Table 2.4 shows the measures variations in different types of bioprostheses with 23 mm labeled valve size).

Tab. 2.4: measure variations in different types of bioprostheses with 23 mm labeled valve size.

	Labeled Valve Size	Stent Outer Diameter (1)	Stent Inner Diameter (2)	Suture Ring Outer Diameter (3)	Valve Height (4)	
Porcine Aortic Valves						
Medtronic Mosaic	23	23	20.5	28	16	
Medtronic Hancock II	23	23	20.5	28	16	
Medtronic Hancock Modified Orifice	23	23	20	29.2	16/18	
Edward's Porcine	23	23	21		16 (*implant height*)	
St. Jude Biocor/Epic	23	23	21		15	
Pericardial Aortic Valves						
Edward Perimount	23	23	22	31	16	
Edward Perimount Magna	23	23	22	31	16	
Sorin Mitroflow	23	22.6	19	26	14	

When transcatheter valves are implanted into native aortic valves, prostheses are typically oversized relative to the annulus diameter by 10% to 30%. Whether sizing principles should differ for a Valve-in-Valve implantation, and even more specifically,

between non-distensible stented valves and “somewhat” distensible stentless valves is yet to be determined. In the absence of any firm evidence or recommendations, the manufacturer’s sizing principles have to be used (23-mm, 26-mm, 29-mm Edwards Sapien valve for internal diameters measuring 18 to 21 mm, 22 to 25 mm and 26 to 28 mm, respectively; 23-mm, 26-mm, 29-mm and 31-mm Medtronic CoreValve for internal diameters measuring 18 to 20mm, 20 to 23 mm, 23 to 27 mm and 26 to 31 mm, respectively.

The choice of the transcatheter valve size is crucial: an undersized transcatheter valve may increase the risk of paravalvular leak or migration/embolization. On the other hand, oversizing may lead to geometrical distortion of the transcatheter valve leaflets and influence its durability. Experimental work in this field is extremely limited. Using pulse duplicators, Azadani et al. [2.74] recently examined the hemodynamic behavior of a 23-mm transcatheter valve implanted within degenerated small-sized Carpentier-Edwards Perimount bioprostheses (19, 21, and 23 mm). The investigators noted that the rigid base ring and the stent posts of the bioprosthesis prevented full expansion of the transcatheter valve in all cases. Although the transvalvular gradients decreased significantly in the 23- and 21-mm bioprostheses, there was no improvement within the 19-mm Perimount bioprosthesis. Furthermore, there was significant central aortic regurgitation with the 19-mm Perimount bioprosthesis. The investigators concluded that the rigid base ring and stent posts appear to offer adequate anchorage for the transcatheter valve. With the currently available transcatheter aortic valves, a Valve-in-Valve implantation within a 19-mm surgical bioprosthesis may yield unacceptable hemodynamics and should be discouraged.

The radio-opaque markers of the bioprosthesis are good landmarks in fluoroscopy during the Valve-in-Valve procedure. The combination of transesophageal

echocardiography with the new generation of high-definition images represents, according to the latest evidence, a useful intraoperative tool to optimize the accuracy of the positioning of the device [2.75]. The fluoroscopic projection, employed for the valve delivery, should be perpendicular to the base ring of the bioprosthesis. In general, the transcatheter valve should be released coaxial to the bioprosthesis.

Although the transfemoral and the transaxillary routes are feasible, a transapical approach (only possible with Edwards Sapien device) facilitate the coaxiality between the transcatheter valve and the bioprosthesis and the first crossing of the bioprosthesis leaflets with the guidewire. The transaortic approach is less considered for Valve-in-Valve procedure because the necessity of a upper partial re-sternotomy, even if it could be considered in some particular cases in which other approaches are not feasible.

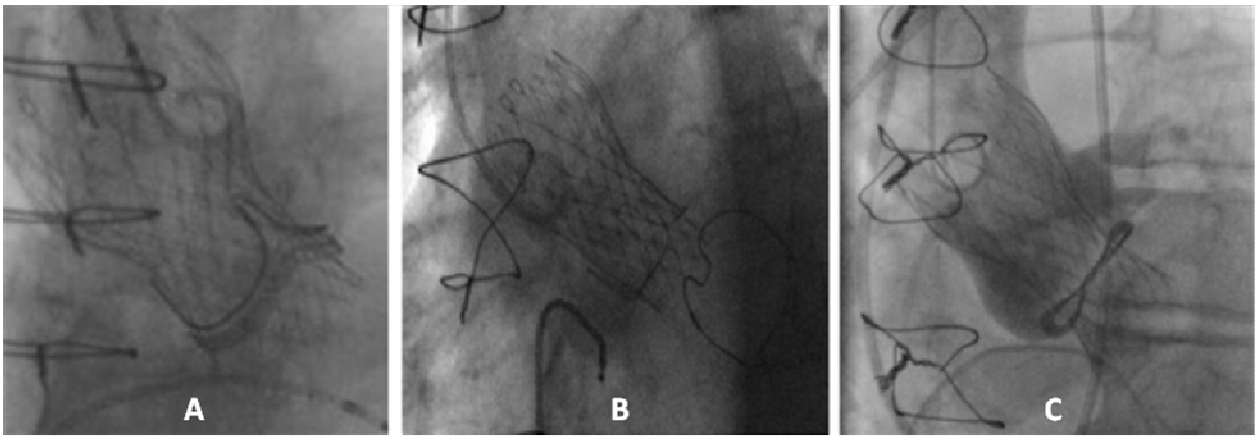

Fig. 2.13: Medtronic CoreValve device deployed into three different bioprostheses (A) Edwards Perimount, (B) C-E Supra-Annular and (C) Sorin Soprano.

In Figure 2.13 it is possible to observe the positioning of the Medtronic CoreValve device within three different degenerated bioprostheses Edwards Perimount, Carpentier-Edwards Supra-Annular and Sorin Soprano (respectively from left to right).

Balloon pre-dilatation before the valve-in-valve implantation is still discussed because of the risk of distal embolization of calcified fragments from leaflets or pannus, which is present in the majority of explanted bioprostheses. Moreover, pre-dilatation can be responsible for prosthetic leaflets laceration causing severe aortic insufficiency with consequent intra-procedural hemodynamic destabilization [2.72]. Furthermore, the most frequent mechanism of bioprostheses failure is the development of valve insufficiency because of leaflets lacerations; such a mechanism would not require a pre-dilation to allow the good expansion of the transcatheter valve.

These technical considerations should be declined on individual cases by considering the mode of failure of the bioprosthesis. It has been suggested as the presence of bulky calcifications or pannus overgrowth can be responsible for a significant discrepancy between the internal diameter of the stent as declared by the manufacturer and the effective internal diameter. It remains to clarify the possible role of pannus in its various degrees as a potential contraindication to the Valve-in-Valve procedure [2.76].

2.3.2 Preliminary results

As specified above, the valve-in-valve procedure is still not recognized as indication by the manufacturers of the transcatheter devices and by regulatory authorities. Since 2007, when the first transcatheter valve was implanted into a degenerated bioprosthesis, multiple case reports or short series have been published, showing the feasibility of the procedure.

One of the first published experiences comes from the German Heart Center in Munich, where among 556 patients who underwent TAVI from 2007 to 2011, 20

(3.6%) had undergone a valve-in-valve procedure [2.77]. In this series, the mean logistic EuroSCORE was 27 ± 13% and the mean STS score was 7 ± 4%. Fourteen patients had a stented bioprosthesis while the remaining had a stentless. The most frequently used access route was that transapical. In two patients the procedure could not be completed, because of the inability to release the prosthesis in one case and the appearance of "stone heart" immediately after balloon predilatation in the second case. This last event can be attributed to massive myocardial ischemia due to obstruction of the coronary ostia. Two more deaths were attributed to post-procedural myocardial ischemia from intraprocedural left coronary ostium obstruction in one case and cardiogenic shock resulting from severe valvular insufficiency in another case. The total procedural mortality in this study was therefore considerable (20%). Another small recent series available [2.78], consisting of 25 cases, reported a 30-day mortality of 12% and confirmed the coronary obstruction as a potential complication of the procedure. In this series, the logistic EuroSCORE score was 31.5 ± 14% while the mean STS score was 8.2 ± 4.2%. The incidence of atrio-ventricular block needing for permanent pacemaker implantation was considerable: 12% during the hospital stay plus an additional patient during follow-up. They observed no or minimal peri-prosthetic insufficiency in 16 patients (64%). The results at follow-up (6 months) were encouraging with all surviving patients in NYHA functional class I or II, a significant decrease in trans-valvular gradient and the stability of the left ventricular ejection fraction compared to the previous procedure.

Medical community has integrated that this procedure could represent, in the next future, a good option to avoid re-sternotomy in excessive surgical risk patients but reproducibility and durability results need to confirm the feasibility data. In order to cumulate the experience about this procedure some non randomized international

registries were born. In 2011 data from a Registry including 9 clinical sites in Germany and Switzerland were published [2.79]. This registry included 47 patients with a mean logistic Euroscore 35 ± 18.5% undergoing transfemoral (n=25) or transapical (n=22) valve-in-valve procedure. They reported a high technical success rates with acceptable post-procedural valvular function and excellent functional improvement. However, in these predominantly elderly high-risk patients with multiple comorbidities, the procedure was associated with 17% hospital mortality.

The most important registry is represented by the Global Valve-in-Valve Registry [2.80] including 54 centers from different countries (North America, Europe, Middle East, Australia and New-Zealand). It includes 416 patients, treated with both available devices. Results have been presented during the EuroPCR 2012 meeting in Paris. Hemodynamic and functional results showed the clinical effectiveness of the procedure. Hospital mortality was 10.9%. Multivariate analysis identified in the bioprosthesis stenosis the principal predictive factor for mortality. These data showed something important about the procedure safety: the malposition rate was 11.1%. The reasons have to be searched in the learning curve and in the intrinsic difficulty of the procedure.

Looking at these preliminary results, it is certainly true that this potential less invasive treatment of bioprosthesis degeneration is encouraging the implantation of bioprostheses even in younger patients. This phenomenon will increase in the next future the incidence of bioprostheses degeneration.

2.4 CONCLUSION

With the advent of trans-catheter valve we are witnessing the birth of a new era for the management of valve diseases based on imaging. Imaging modalities are becoming more and more necessary for new generation practitioners because the good structural and morphological understanding allow a better planning of the procedures. This translates into a greater awareness of the pathology and should consequently facilitate clinical decision improving results.

The functional assessment of bioprostheses after aortic valve replacement is represented by echocardiographic parameters that allow patients follow-up together with the clinics. But the reliability of echocardiography is not the same when we look at the morphological understanding of the bioprosthetic degeneration that could be useful during standard follow-up as well as for the decision making of a therapeutic solution. Failure mechanisms such as leaflet calcifications or tears, pannus formation or leaflets thrombosis should be preoperatively detected in order to choose the best adapted treatment.

In this context, some methods to allow 3D leaflets analysis should be considered. In the following chapters we present the state of the art on cardiac imaging, especially CT images, and we propose some methods to process CT images concerning bioprosthesis. Finally we discuss our results.

2.5 REFERENCES

[2.1]. Iung B, Baron G, Butchart EG, et al. A prospective survey of patients with valvular heart disease in Europe: the Euro Heart Survey on valvular heart disease. Eur Heart J 2003;24:1231-43.

[2.2]. Cunanan CM, Cabiling CM, Dinh TT et al. Tissue characterization and calcification potential of commercial bioprosthetic heart valves. Ann Thorac Surg 2001;71:S417-21.

[2.3]. Ruggieri VG, Flecher E, Anselmi A, et al. Long-Term Results of the Carpentier-Edwards Supraannular Aortic Valve Prosthesis. Ann Thorac Surg. 2012 Jul 7.

[2.4]. Lupinetti FM, Lemmer JH Jr. Comparison of allografts and prosthetic valves when used for emergency aortic valve replacement for active infective endocarditis. Am J Cardiol 1991; 68: 637.

[2.5]. David TE, Armstrong S, Sun Z. The Hancock II bioprosthesis at ten years. Ann Thorac Surg 1995;60:S229-34.

[2.6]. Edmunds LH, Cohn LH, Weisel RD. Guidelilnes for reporting morbidity and mortality after cardiac valvular operations. J Thorac Cardiovasc Surg 1988;96:351-3.

[2.7]. Akins CW, Miller DC, Turina IM et al. Guidelines for reporting morbidity and mortality after cardiac valve interventions. J Thorac Cardiovasc surg 2008.

[2.8]. Cohen G, David TE, Ivanov J et al. The impact of age, coronary artery disease, and cardiac comorbidity on late survival after bioprosthetic aortic valve replacement. J Thorac Cardiovasc Surg 1999;117:273-84.

[2.9]. Hammermeister KE, Sethi GK, Henderson WG et al. A comparison of outcomes in men 11 years after heart-valve replacement with a mechanical valve or bioprosthesis. Veterans Affairs Cooperative Study on Valvular Heart Disease. N Engl J Med 1993;328:1289.

[2.10]. David TE, Ivanov J, Armstrong S et al. Late results of heart valve replacement with the Hancock II bioprosthesis. J Thorac Cardiovasc Surg 2001;121:268.

[2.11]. Stahle E, Kvidal P, Nystrom SO et al. Long-term relative survival after primary heart valve replacement. Eur J Cardio-Thorac Surg 2002;11:81.

[2.12]. Dellgren G, David TE, Raanani E et al. Late hemodynamic and clinical outcomes of aortic valve replacement with the Carpentier-Edwards Perimount pericardial bioprosthesis. J Thorac Cardiovasc Surg 2002;124:146.

[2.13]. Verheul HA, van den Brink BB, Bouma BJ et al. Analysis of risk factors for excess mortality after aortic valve replacement. J Am Coll Cardiol 1995;26:1280.

[2.14]. Abdelnoor M, Hauge SN, Hall KV et al. Prognostic variables in late follow-up of aortic valve replacement using the proportional hazard model: a study on patients using the Medtronic-Hall cardiac prosthesis. Life Support Syst 1986;4:103.

[2.15]. Aranki SF, Rizzo RJ, Couper GS et al. Aortic valve replacement in the elderly. Effect of gender and coronary artery disease on operative mortality. Circulation 2002;88:II17.

[2.16]. Gonzalez-Lavin L, Gonzalez-Lavin J, McGrath LB et al. Factors determining in-hospital or late survival after aortic valve replacement. Chest 2002;95:38.

[2.17]. Hammermeister KE, Sethi GK, Henderson WG, et al. Outcomes 15 years after valve replacement with a mechanical versus a bioprosthetic valve: final report of the Veterans Affaits randomized trial. J Am Coll Cardiol 2000;36:1152.

[2.18]. Grunkeimeier G, Jin R, Eijkemans J et al. Actual and actuarial probabilities of competing risks: apples and lemons. Ann Thorac Surg 2007;83:1586-1592.

[2.19]. Grunkemeier G, Takkenberg J, Jamieson WR et al. Reporting “actual freedom” should not be banned. J Thorac Cardiovasc Surg 2008;135:460-462.

[2.20]. Bodnar E, Bkackstone E. An “actual” problem: another issue of apples and oranges. J Thorac Cardiovasc Surg 2006;131:1-3.

[2.21]. Grunkemeier G, Takkenberg J, Jamieson WR et al. In response to: Bodnar E, Blackstone EH. Editorial: an “actual” problem: another issue of apples and oranges. J Heart Valve Dis 2006;15:305-6.

[2.22]. Butany J, Nair V, Leong SW, et al. Carpentier-Edwards Perimount valves—morphological findings in surgical explants. J Card Surg 2007;22:7–12.

[2.23]. Butany J, Vanlerberghe K, Silver MD. Morphologic findings and causes of failure in 24 explanted Ionescu-Shiley low-profile pericardial heart valves. Hum Pathol 1992;23:1224 –33.

[2.24]. Roselli EE, Smedira NG, Blackstone EH. Failure modes of the Carpentier-Edwards pericardial bioprosthesis in the aortic position. J Heart Valve Dis 2006;15:421–7, discussion 427–8.

[2.25]. McGonagle-Wolff K, Schoen FJ. Morphologic findings in explanted Mitroflow pericardial bioprosthetic valves. Am J Cardiol 1992;70:263–4.

[2.26]. Schoen FJ, Levy RJ: Founder's Award, 25th Annual Meeting of the Society for Biomaterials, perspectives. Providence, RI, April 28-May 2, 1999. Tissue Heart Valves: current challenges and future research perspectives. J Biomed Mater Res 1999;47:439.

[2.27]. Schoen FJ, Levy RJ, Nelson AC et al. Onset and progression of experimental bioprosthetic heart valve calcification. Lab Invest 1985;52:523.

[2.28]. Ishihara T, Ferrens VJ, Boyce SW et al. Structure and classification of cuspal tears and perforations in porcine bioprosthetic cardiac valves implanted in patients. Am J Cardiol 1981;48:665-78.

[2.29]. Butany J, Nair V, Leong S et al. Carpenier-Edwards Perimount valves – morphological findings in surgical explants. J Card Surg 2007;22:7-12.

[2.30]. Butany J, Leask R. The failure modes of biological prosthetic heart valves. J long Term Eff Med Implants 2001;11:115-35.

[2.31]. Grunkemeier GL, Jin R, Starr A. Prosthetic heart valves: objective performance criteria versus randomized clinical trial. Ann Thorac Surg 2006;82:776–80.

[2.32]. Colli A, Verhoye JP, Heijmen R, et al. Antithrombotic therapy after bioprosthetic aortic valve replacement: ACTION Registry survey results. Eur J Cardiothorac Surg. 2008 Apr;33(4):531-6.

[2.33]. Vogt PR, Brunner-LaRocca H, Sidler P, et al. Reoperative surgery for degenerated aortic bioprostheses: Predictors for emergency surgery and reoperative mortality. Eur J Cardiothorac Surg 2000; 17:134.

[2.34]. Borkon AM, Soule LM, Baughman KL, et al. Aortic valve selection in the elderly patient. Ann Thorac Surg 1988; 46:270.

[2.35]. Birkmeyer NJ, Birkmeyer JD, Tosteson AN, et al. Prosthetic valve type for patients undergoing aortic valve replacement: A decision analysis. Ann Thorac Surg 2000; 70:1946.

[2.36]. Birkmeyer NJ, Marrin CA, Morton JR, et al. Decreasing mortality for aortic and mitral valve surgery in northern New England. Northern New England Cardiovascular Disease Study Group. Ann Thorac Surg 2000; 70:432.

[2.37]. Bloomfield P, Wheatley DJ, Prescott RJ, Miller HC. Twelve-year comparison of a Bjork-Shiley mechanical heart valve with porcine bioprostheses. N Engl J Med 1991; 324:573.

[2.38]. Cohn LH, Collins JJ Jr, DiSesa VJ, et al. Fifteen-year experience with 1678 Hancock porcine bioprosthetic heart valve replacements. Ann Surg 1989; 210:435. discussion 442.

[2.39]. Jamieson WR, Munro AI, Miyagishima RT, et al. Carpentier-Edwards standard porcine bioprosthesis: Clinical performance to seventeen years. Ann Thorac Surg 1995; 60:999. discussion 1007.

[2.40]. O'Brien MF, Harrocks S, Clarke A, et al. Experiences with redo aortic valve surgery. J Card Surg 2002; 17:35.

[2.41]. Barwinsky J, Cohen M, Bhattacharya S, et al. Bjork-Shiley cardiac valves long term results: Winnipeg experience. Can J Cardiol 1988; 4:366.

[2.42]. Gaudiani VA, Grunkemeier GL, Castro LJ, et al. The risks and benefits of reoperative aortic valve replacement. Heart Surg Forum 2004; 7:E170.

[2.43]. Potter DD, Sundt TM 3d, Zehr KJ, et al. Operative risk of reoperative aortic valve replacement. J Thorac Cardiovasc Surg 2005; 129:94.

[2.44]. Phillips BJ, Karavas AN, Aranki SF, et al. Management of mild aortic stenosis during coronary artery bypass surgery: An update, 1992–2001. J Card Surg 2003; 18:507.

[2.45]. Bortolotti U, Guerra F, Magni A, et al. Emergency reoperation for primary tissue failure of porcine bioprostheses. Am J Cardiol 1987; 60:920.

[2.46]. Byrne JG, Karavas AN, Aklog L, et al. Aortic valve reoperation after homograft or autograft replacement. J Heart Valve Dis 2001; 10:451.

[2.47]. O'Brien MF, McGiffin DC, Stafford EG, et al. Allograft aortic valve replacement: Long-term comparative clinical analysis of the viable cryopreserved and antibiotic 4℃ stored valves. J Card Surg 1991; 6:5 34.

[2.48]. McGiffin DC, Galbraith AJ, O'Brien MF, et al. An analysis of valve re-replacement after aortic valve replacement with biologic devices. J Thorac Cardiovasc Surg 1997; 113:311.

[2.49]. Hasnat K, Birks EJ, Liddicoat J, et al. Patient outcome and valve performance following a second aortic valve homograft replacement. Circulation 1999; 100:II-42.

[2.50]. Albertucci M, Wong K, Petrou M, et al. The use of unstented homograft valves for aortic valve reoperations: Review of a 23-year experience. J Thorac Cardiovasc Surg 1994; 107:152.

[2.51]. Sundt TM 3d, Rasmi N, Wong K, et al. Reoperative aortic valve operation after homograft root replacement: Surgical options and results. Ann Thorac Surg 1995; 60:S95; discussion S100.

[2.52]. Yacoub M, Rasmi NR, Sundt TM, et al. Fourteen-year experience with homovital homografts for aortic valve replacement. J Thorac Cardiovasc Surg 1995; 110:186. discussion 193.

[2.53]. Kumar P, Athanasiou T, Ali A, et al. Redo aortic valve replacement: Does a previous homograft influence the operative outcome? J Heart Valve Dis 2004; 13:904.

[2.54]. Sadowski J, Kapelak B, Bartus K, et al. Reoperation after fresh homograft replacement: 23 years' experience with 655 patients. Eur J Cardiothorac Surg 2003; 23:996.

[2.55]. David TE, Feindel CM, Ivanov J, Armstrong S. Aortic root replacement in patients with previous heart surgery. J Card Surg 2004; 19:325.

[2.56]. Aviram G, Sharoney R, Kramer A, et al. Modificatoin of surgical planning based on cardiac multidetector computed tomography in reoperative heart surgery. Ann Thorac Surg 2005; 79:589.

[2.57]. Gilkeson RC, Markowitz AH, Ciancibello L. Multisection CT evaluation of the reoperative cardiac surgery patient. Radiograhics 2003; 23:S3.

[2.58]. Dobell AR, Jain AK: Catastrophic hemorrhage during redo sternotomy. Ann Thorac Surg 1984; 37:273.

[2.59]. Vogt PR, Brunner-LaRocca H, Sidler P et al. Reoperative surgery for degenerated aortic bioprostheses: predictors of emergency surgery and reoperative mortality. Eur J Cardio-Thorac Surg 2000;17:134-9.

[2.60]. Gaudiani VA, Grunkemeier GL, Castro LJ et al. The risks and benefits of re operative aortic valve replacement. Heart Surg Forum 2004;7:E170-3.

[2.61]. Potter D, Sundt TM, Zehr K et al. Operative risk of reoperative aortic valve replacement. J Thorac Cardiovasc Surg 2005;129:94-103.

[2.62]. Luciani N, Nasso G, Anselmi A et al. Repeat valvular operations: bench optimization of conventional surgery. Ann Thorac Surg 2006;81:1279-83.

[2.63]. Ruggieri VG, Roudmane Lenglet N, Anselmi A, et al. Résultats de la chirurgie valvulaire aortique redux après implantation d'une bioprothèse. Expérience rennaise. Journal Chirurgie Thoracique Cardio-Vasculaire - 2012 ; 16(3) : 157-163.

[2.64]. Wenaweser P, Buellesfeld L, Gerckens U et al. Percutaneous aortic valve replacement for severe regurgitation in degenerated bioprosthesis: the firs valve in valve procedure using the CoreValve revalving system. Catheter Cardiovasc Interv 2007;70:760-4.

[2.65]. Klaaborg KE, Egeblad H, Jakobsen CJ et al. Transapical transcatheter treatment of a stenosed aortic valve bioprosthesis using the Edwards Sapien transcatheter heart valve. Ann Thorac Surg 2009;87:1943-6.

[2.66]. Attias D, Himbert D, Hvass U et al. Valve-in-valve implantation in a patient with stentless bioprosthesis and severe intraprosthetic aortic regurgitation. J Thorac Cardiovasc Surg 2009;138:1020-2.

[2.67]. Schmoeckel M, Boeckstegers P, Nikolau K et al. First successful transapical aortic valve implantation after aortic allograft replacement. J Thorac Cardiovasc Surg 2009;138:1016-7.

[2.68]. Dainese L, Fusari M, Trabattoni P et al. Redo in aortic homograft replacement: transcatheter aortic valve as a valid alternative to surgical replacement. J Thorac Cardiovasc Surg 2010;139:1656-7.

[2.69]. Ferrari E, Marcucci C, Sulzer C et al. Which available transapical transcatheter valve fits into degenerated aortic bioprosthesis? Interact Cardiovasc Thorac Surg 2010;11:83-5.

[2.70]. Webb JG, Wood DA, Ye J et al. Transcatheter valve-in-valve implantation for failed bioprosthetic heart valves. Circulation 2010;121:1848-57.

[2.71]. Seiffert M, Franzen O, Conradi L et al. Series of transcatheter valve-in-valve implantations in high-risk patients with degenerated bioprostheses in aortic and mitral position. Catheter Cardiovasc Interv 2010;76:608-15.

[2.72]. Ruggieri VG, Bedossa M, Verhoye JP. Urgent transaxillary valve-in-valve procedure using the Edwards 16F expandable introducer. Catheter Cardiovasc Interv 2012 in press.

[2.73]. Verhoye JP, Ruggieri VG, Paramythiotis A et al. Trans-apical valve in homograft. J Heart Valve Dis 2012 in press.

[2.74]. Azadani AN, Jaussaud N, Matthews P et al. Transcatheter aortic valves inadequately relieve stenosis in small degenerated bioprostheses. Interact Cardiovasc Thorac Surg 2010;11:70-77.

[2.75]. Verhoye JP, Lapeze J, Anselmi A et al. Association of transaortic approach and transesophageal echocardiography as the primary imaging technique for improved results in transcatheter valve implantation. Interact Cardiovasc Thorac Surg 2012 in press.

[2.76]. Ruggieri VG, Anselmi A, Wang Q, et al. CT scan images processing to detect the real mechanism of bioprosthesis failure. Implication for valve-in-valve implantatio. JHVD 2012 in press.

[2.77]. Piazza N, Bleiziffer S, Brockmann G et al. Transcatheter aortic valve implantation for failing surghical aortic bioprosthetic valve: Part 2. JACC Cardiovascular Interventions 2011;4:733-42.

[2.78]. Bedogni F, Laudisa ML, Pizzocri S et al. Transcatheter valve-in-valve implantation using CoreValve revalving system for failed surgical aortic bioprostheses. JACC Cardiovasc Interv 2011;4:1228-34.

[2.79]. Eggebrecht H, Schäfer U, Treede H, et al. Valve-in-valve transcatheter aortic valve implantation for degenerated bioprosthetic heart valves. JACC Cardiovasc Interv. 2011 Nov;4(11):1218-27.

[2.80]. Dvir D. TAVI for degenerative bioprosthetic surgical valves : results of the global valve-in-valve registry. Late Breaking clinical Trial. EuroPCR 2012.

III – STATE OF THE ART

3.1 3D CARDIAC IMAGING

Cardiac imaging techniques have had a great development in the last years. In this section we present the three main 3D imaging modalities and we focus on multi-slices CT.

Threedimensional (3D) echocardiography offers the ability to improve and expand the diagnostic capabilities of cardiac ultrasound. However, as with any emerging technology, the enthusiasm to embrace a new technique must be tempered by a critical appraisal of the evidence supporting its use. At the moment, it represents a new safe, non-invasive imaging modality that is complementary and supplementary to 2D imaging and that provides improved accuracy and reproducibility over 2D methods for left ventricular volume and function calculation and for the mitral valve functional assessment [3.1]. Limitations of 3D echocardiography includes poor visualization of anterior structures of the heart, suboptimal images due to poor ECG triggering in patients with arrhythmias, reduced spatial and temporal resolution with narrow angled acquisitions as well tissue dropout. Anterior cardiac structures such as the aortic and tricuspid valves due to their increased distance from the probe cannot be visualized as well as posterior structures such as the mitral valve [3.2]. Finally, at the moment echocardiography remain the gold standard to analyze aortic bioprosthesis function, but can't be used for the morphological tridimensional analysis of bioprosthetic leaflets yet.

Magnetic resonance imaging (MRI) [3.3] is an imaging methodology based on aligning the spin axis of nuclei within molecules of the object being visualized using both powerful superconducting magnets and radio frequency signals and detectors. MRI in cardiac imaging is growing, because its outstanding differentiates in soft tissues. There is a promising future in cardiac MRI by more efficient scans, increasing availability of scanners and more widespread knowledge about its clinical application. The quality of MRI images may be reduced by the continuous movement of vascular structures and current implementations for cardiology uses are sometimes limited by lengthy protocols, claustrophobia and contraindications based on some complex metallic implants such as metal stent of aortic valve prosthesis. Concerning valve prosthesis and leaflets degeneration, the main physical limitation of MRI are the metal artifacts from the stent and the inability to visualize calcifications. On the other hand it may play a role in the identification of leaflets thrombosis.

Computed tomography (CT) angiography [3.4] is an imaging methodology using a ring-shaped machine with an X-Ray source spinning around the circular path so as to calculate (generally use Fourier filter back projection) the X-Ray density voxels inside circular path. Because of the incredible developments in CT technology, Cardiac CT imaging is growing. Currently, multi-slicer computed tomography (MSCT), or known as “multi-detectors CT (MDCT)”, have 64 or more detectors. It allows to make a cardiac imaging in a very short time. Moreover it can provide 3D+T cardiac image sets.

3.2 MULTI-SLICE CT (MSCT) FOR CARDIAC IMAGING

3.2.1 ECG-Gated Cardiac CT [3.5]

MSCT was presented to cardiac imaging in 1999. The current generation of MSCT systems is capable of acquiring 4 to 64 sections of the heart simultaneously with ECG gating in either a prospective or retrospective mode. MSCT differs from single detector–row helical or spiral CT systems principally by the design of the detector arrays and data acquisition systems, which allows the detector arrays to be configured electronically to acquire multiple adjacent sections simultaneously. In the current 64-row MSCT systems, the thickness of slice can be of 0.625 mm at least.

3.2.1.1 General Principles

The basic principles of MDCT are relatively simple (Fig. 3.1 A). The X-ray point source and the detector array are placed on opposite sides of the patient on a ringlike structure called the gantry. The gantry rotates around the patient, who is located on a table at its center. The table moves at constant speed along the axis of the gantry. X rays are emitted toward the patient, penetrate the patient, and are captured by one or more detectors. This process generates a series of helical projections of the patient's attenuation properties. Images representing X-ray attenuation at each point in the volume traversed by the photons are then mathematically reconstructed from the helical projection data (Fig. 3.1 B).

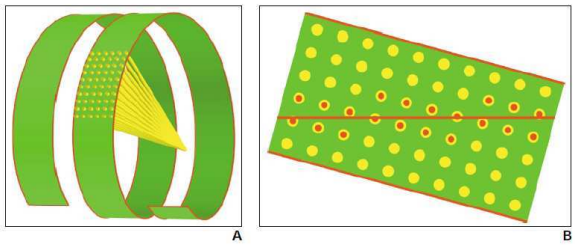

Fig. 3.1: Drawings show helical projections from MDCT. A, Detectors follow 3D helical path, with table advancing at constant speed while gantry is rotating. Tube emits X-ray radiation (*yellow*) that is recorded by detectors. Resulting set of projections has helical configuration in space. B, Images are reconstructed from projection data by linear interpolation from projections closest to image plane. Advanced algorithms correct for cone-beam geometry [3.5].

Effective slice thickness using a single-slice detector scanner is determined by collimation, whereas in multidetector scanners it is determined by both the detector configuration and the reconstruction method. The table travel per complete rotation of the gantry divided by the X-ray beam width is called the “beam pitch”. The beam pitch conforms to the current industry standard of pitch. In multi-detector scanners, another definition of pitch is sometimes used: the table travel per complete rotation of the gantry divided by the detector width, called the “detector pitch”. With a (beam) pitch of 0, there is no table motion and scanning is axial. With a pitch of 1, the table displacement for each rotation is equal to the *z*-axis dimension of the array of active rows of detectors. A pitch greater than 1 implies gaps in the helix of projections, whereas a pitch between 0 and 1 implies overlap between the projections (Fig. 3.2).

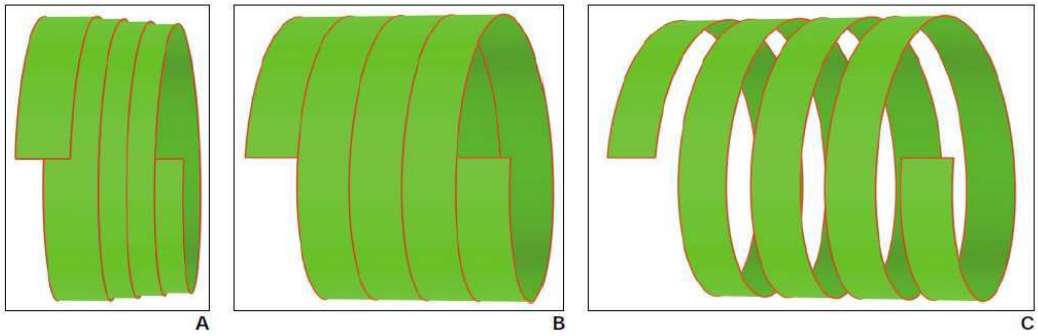

Fig. 3.2: Drawings show that relation of table movement with respect to gantry rotation is described by beam pitch. A, Pitch of 0.5:1 indicates 50% overlap in projection data. B, Pitch of 1:1 indicates neither overlap nor gap in data. C, Pitch of 1.5:1 indicates 50% gap in data [3.5].

Images are reconstructed from linear interpolation of projection data from rays that are the closest to the image plane, using algorithms to correct for cone-beam geometry. A minimum of 180º of projection data are mathematically required to reconstruct a complete image. Thus, slice thickness increases with pitch, which determines how much the table travels during a 180º rotation. The thinnest slice is equal to the height of a single row of detectors (the detectors are actually wider than the slice to compensate for geometric magnification). Thicker slices can be generated mathematically by combining the thinner slices. The determinants of in-plane resolution are focal spot size, detector width and geometry, reconstruction algorithm, and image matrix size. The determinants of longitudinal *z*-axis resolution are focal spot size, detector height and collimation, and reconstruction algorithm. The determinants of temporal resolution are gantry rotation speed and reconstruction algorithm.

3.2.1.2 Cardiac Gating

Gating techniques are used to improve temporal resolution and minimize imaging artifacts caused by cardiac motion. Two approaches to cardiac gating are typically used: prospective ECG triggering and retrospective ECG gating. The least cardiac motion occurs during diastole, when the ventricles are passively filling. A comparison between prospective and retrospective ECG-gating is presented in Tab. 3.1 [3.6].

Tab. 3.1: Comparison of different parameters between prospective and retrospective ECG-gating.

Parameters to be compared	Retrospective ECG-gating		Prospective ECG-gating	
	Pros	Cons	Pros	Cons
Scanning protocols	Axial helical scan allows acquisition of volume data	Exposure takes place during the entire cardiac cycle and only a portion of data is used for reconstruction	Exposure only occurs at a selected cardiac cycle (late diastolic phase)	Axial non-helical scan with most of the manufacturers; thus no volume data is available
Image quality (assessable segments)	98-100%	Affected by heavy calcification and high heart rate	95-99%	Affected when heart rate is >70 bpm
Effect of heart rate	Diagnostic accuracy is high even in higher heart rate; Independent of heart rate with dual source CT	Diagnostic accuracy slightly decreases with increasing heart rate (70-100 bpm)	High assessable segments and diagnostic value in low heart rate	Limited to heart rate <70 bmp; Limited to regular and stable heart rate
Diagnostic value	High sensitivity and specificity, especially very high negative predictive value	Sensitivity is affected by heavy calcification	High diagnostic accuracy, although the data is scarce at the moment	Very limited data available
Radiation dose	Online tube current modulation could reduce radiation dose	High radiation dose with range of 7.6-31.8 mSv	Significant reduction of with range of 2.1-9.2 mSv	
Cardiac functional assessment	Available as volume data are acquired		Functional assessment is only available with 256- or 320-slice CT	Unavailable with 64-slice CT scanners

Prospective ECG triggering uses the ECG signal to control scanning, so that X rays are generated and projection data are acquired only during cardiac diastole, more than half the rotation of the gantry. The total number of slices produced per heartbeat during this half

rotation of the gantry is proportional to the number of rows of active detectors. Because an axial scanning method (rather than helical) is typically used and the table has to move by the total collimation width after each acquisition, one heartbeat typically has to be skipped between each acquisition. About 12 cm of scanning is required to cover most heart sizes, which requires approximately 48 heartbeats for single-slice CT (5-mm collimation), 24 heartbeats for 4-slice MDCT (2.5-mm collimation each row), 12 heartbeats for 16-slice MDCT (1.25-mm collimation each row) and 6 heartbeats for 64-slice MDCT (0.625-mm collimation each row). Thus, multidetector technology can obtain the entire scan during one breath-hold. The start of the diastolic phase of the cardiac cycle is estimated from the prior three to seven consecutive heartbeats and occurs approximately 450 msec before the R wave on the ECG.

Prospective triggering techniques have important limitations. They are sensitive to heart rate changes and arrhythmias, but they have limited spatial *z*-axis resolution in order to cover the entire heart in a single breath-hold. They are effective only for heart rates of less than 70 beats per minute and perform poorly with arrhythmias, such as in atrial fibrillation. To overcome these limitations, retrospective ECG gating techniques are commonly used, at the expense of a higher radiation dose.

Retrospective gating techniques allow faster continuous cardiac volume coverage, improved *z*-axis resolution, and imaging of the entire cardiac cycle for functional analysis. In retrospective techniques, partially overlapping MDCT projections are continuously acquired, and the ECG signal is simultaneously recorded. Algorithms are then used to sort the data from different phases of the cardiac cycle by progressively shifting the temporal

window of acquired helical projection data relative to the R wave (Fig. 3.3).

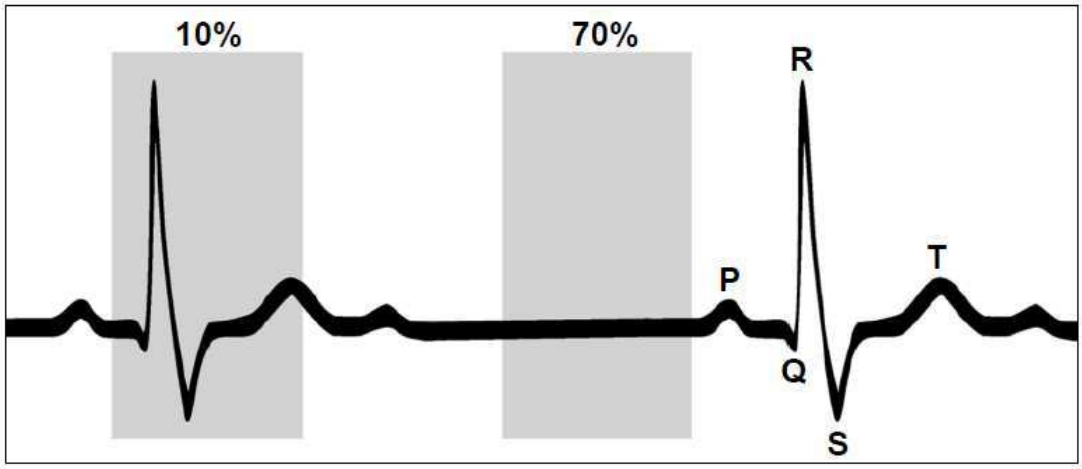

Fig. 3.3: Temporal window for reconstruction from projection data is approximately 250 msec. Drawing shows that center of window can be located anywhere during heart cycle. Left box has its center at 10% of R-R interval, which is during systole. Right box has its center at 70% of R-R interval, which is during diastole and is most common motion-free imaging temporal window for heart [3.5].

Every position of the heart must be covered by a detector row at every point during the cardiac cycle. This means that the scanner table must not advance more than the total width of the active detectors for each heartbeat. Helical pitch can be varied proportionally to the heart rate to achieve continuous volume coverage. Typical pitch for an average heart rate of 70 beats per minute is 0.16-0.22:1, with a total scanning time of about 5-10 sec for a 64-slice MDCT scanner using 0.625-mm collimation.

Two main algorithmic approaches are used to perform retrospective cardiac gating: partial scanning and segmented adapted scanning. To reconstruct an image, a minimum helical projection data segment of 180º must be available for every fan angle, corresponding to a rotation of 180º plus the breadth of the fan beam, so approximately two thirds of a full gantry rotation is required (Fig.3.4 A). This technique is called *partial scanning*. Temporal

resolution is therefore two thirds of rotation time. Parallel beam geometries and rebinning techniques can be used to decrease the minimum data segment to 180º, with a temporal resolution of half the rotation time, or 250 msec for 16-slice MDCT scanners. The partial scanning technique is typically used in patients with heart rates between 40 and 75 beats per minute. To improve temporal resolution, *segmented adaptive reconstruction* can be used, which involves combining shorter segments of projection data from two of more subsequent cardiac cycles (Fig. 3.4 B). Temporal resolution is equal to that of the longest projection data segment. Maximum values for temporal resolution are 125 msec for segmentation over two cardiac cycles and 65 msec over four cardiac cycles. Either volume coverage or longitudinal resolution may need to be reduced to maintain a low pitch and still scan in a single breath-hold.

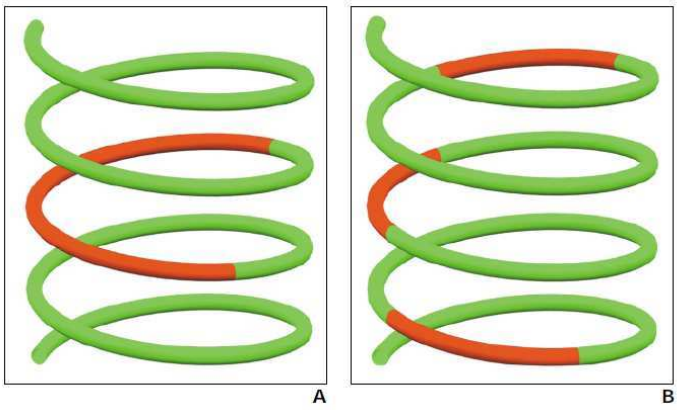

Fig. 3.4: Drawings show two types of retrospective reconstruction algorithms. A, In partial scanning algorithm, continuous segment of projection data at single heartbeat is used to reconstruct image. B, In segmented adaptive algorithm, different segments of projection data from same phase of cardiac cycle at successive heartbeats are used to reconstruct image. Cardiac cycle and gantry rotation must not be synchronized for different segments to cumulatively cover large enough range of projection angles to reconstruct image from data [3.5].

3.2.1.3 Technical Considerations

Several elements of cardiac CT can be optimized to produce the best possible images at the lowest dose of radiation.

Patient Position

The position of the patient in the CT scanner is important, because a patient placed offcenter in the scanner produces images with suboptimal temporal resolution. The temporal resolution of any given pixel in an image depends on the temporal window of the projection data used to reconstruct that specific pixel. In helical CT using a partial scanning algorithm, a minimum helical projection data segment of 180º must be available for every fan angle, so each image is reconstructed from a segment of projection data longer than 180º. However, not every detector contributes data at each projection angle to reconstruct an image. For example, if a patient is scanned clockwise from the 11-o'clock to the 7-o'clock position to produce an image, the left side of the chest in the image has a much tighter temporal window than the right side. The temporal resolution of the points of the image increases almost linearly between the edges of the field of view going from the left side of the chest to the right side. By positioning the heart near the center of rotation of the gantry, the temporal resolution of its elements remains constant and average, rather than going from bad to better as the X-ray tube rotates on the gantry.

Heart Rate

The heart rate of the patient is an important determinant of image reconstruction quality and for selecting scanning parameters such as pitch and reconstruction algorithms. If the heart

rate is too high (> 100 beats per minute), a temporal resolution of less than 150 msec becomes necessary for motion-free cardiac imaging during diastole. Segmented adaptive reconstruction can be used to improve temporal resolution, but at the expense of volume coverage or longitudinal resolution, to keep scanning time in one breath-hold. If neither can be sacrificed, β-blocker medication can be administered orally or IV 1 hr before scanning to reduce the heart rate and its variations.

If segmented adaptive reconstruction is used, improved temporal resolution can be achieved only if the patient's heart rate is not synchronized with the rotation cycle of the gantry. If they are synchronized, the same cardiac phase corresponds to the same angular segment of projection data at every rotation, and it is therefore not possible to build the 180º span of projection data required to reconstruct individual images.

A patient's heart rate may vary during scanning. The heart rate decreases after breathholding. If the heart rate varies during scanning after the rotation time and pitch are selected by the operator, the temporal resolution will vary from image to image.

Pitch

Helical pitch is a parameter that is selected before the examination is acquired. Helical pitch is varied proportionally to the heart rate to achieve continuous volume coverage. If the heart rate increases, the pitch can increase. If the heart rate decreases, the pitch must decrease. If the pitch is too high given the heart rate, gaps in the image data set are present. A pitch that is too low implies increased radiation exposure and increased duration of the breath-hold. Before scanning, the heart rate of the patient should be assessed under breath-holding conditions, and the lowest expected heart rate should be used to select the

pitch. The latest scanners can automatically adjust the pitch when variations in the heart rate are detected.

Collimation

Scans should be acquired at the best possible spatial resolution for the specific task at hand. Coronary angiography requires the best resolution. The left main artery has a diameter of 4 mm, and the distal left anterior descending and circumflex arteries have diameters of 1 mm. Sub-millimeter spatial resolution, both in-plane and longitudinally, is therefore required for coronary CT angiography. Other examinations, such as calcium scoring, do not require a so fine longitudinal spatial resolution and are performed with slightly larger collimation. It is always possible to reconstruct thicker slices from the projection data of thinner slices, but thinner slices require higher radiation exposure.

Dosimetry

Radiation exposure for cardiac CT is relatively high because of continuous overlapping scanning and the use of retrospective cardiac gating. Coronary CT angiography has a 5- to 10-mSv exposure, which is more than the typical 2 mSv of traditional diagnostic catheter coronary angiography. Calcium scoring has an exposure of 1–2 mSv. Modern scanners incorporate fine control of tube current with respect to cardiac cycle, and this will become more important as spatial resolution is improved in future units. Radiation dose should be high enough to maintain an appropriate contrast-to-noise ratio for diagnostic quality images, but no higher.

3.2.1.4 Clinical Indications

The two most important clinical indications for cardiac CT are calcium scoring and coronary CT angiography. CT may also be used to characterize coronary plaque and to evaluate cardiac function, myocardial perfusion, infarcts, tumors, pericardial disease, postsurgical complications and congenital malformations. The exact roles of coronary CT angiography for atherosclerotic heart disease and patient selection criteria for coronary CT angiography are under investigation.

3.3 NOISE AND ARTIFACTS

3.3.1 Noise and metal artifacts in MSCT images

The main source of noise in CT is quantum noise [3.7-3.9]. It results from statistical fluctuations in the number of X ray quanta. In MSCT images, noise is emerging from several sources: detector elements, signal transmission, reconstruction and processing methods, etc. Due to these complex dependencies, the noise distribution model is usually unknown.

Streak artifacts constitute a kind of directed noise, like metal artifacts, that results in general from an inconsistency in projection sample measurements. Such inconsistencies may arise from patient motion, data under-sampling or when only few quanta reach the detector [3.7-3.9]. This happens mainly when highly attenuating objects, like bones or metallic stents, are scanned (Fig 3.5).

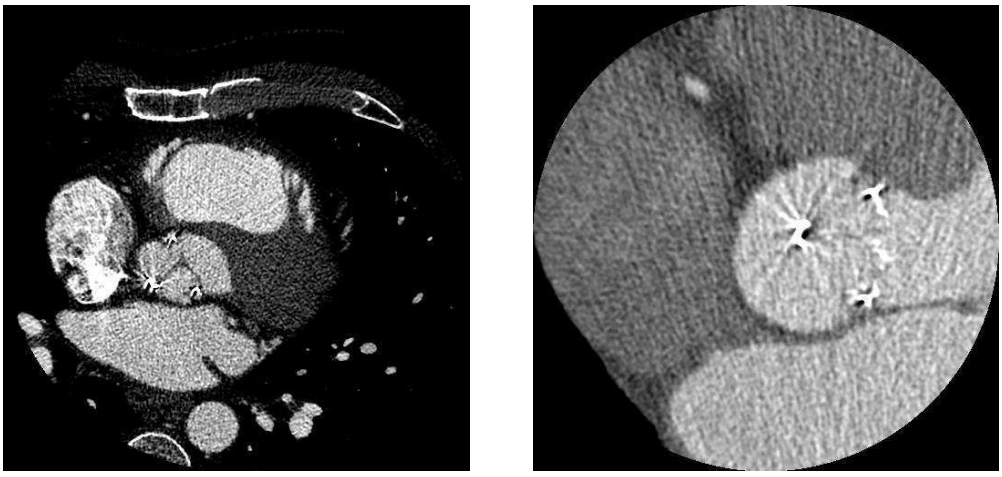

A B

Fig. 3.5: Example of noise and metal artifacts in MSCT images of bioprosthesis (A, B). Image B shows strong directional noise.

Bioprostheses can have incomplete or complete metallic stent. Because of the higher atomic number, the metal object attenuates X-rays in the diagnostic energy range much more than soft tissues and bone, and much fewer photons can reach detectors [3.10]. When metal is present, pronounced dark and bright streaks are produced in reconstruction with conventional filtered back projection. These artifacts seriously degrade image quality, particularly near the metal surfaces. Primary applications of metal artifact reduction include dental, orthopedic, oncologic imaging. Metal artifact reduction in MSCT images of aortic valve prosthesis is a new issue in cardiac CT imaging.

3.3.2 Motion–related imaging artifacts

Although cardiac CT imaging has a very high temporal resolution (between 80ms and 330ms), this is not enough to avoid the motion–related imaging artifacts. MSCT demands a 65 bpm heart rate limitation (for the coronary arteries) [3.4]. The motion–related imaging artifacts may cause false segmentation of moving leaflets (both prosthesis and natural), increasing the thickness value.

3.3.3 Spatial resolution

Currently, the spatial resolution of MSCT can reach values down to 0.3 mm per pixel and 0.6 mm for z-axis [3.4]. Analyzing aortic valve bioprosthesis, the problem is represented by leaflets thickness. Depending from the type of bioprosthesis, pericardial or porcine, and

from the manufacturer, leaflet thickness is submillimetric. In the process of filtered back projection (FBP), voxels, whose spaces include both leaflets and vascular lumen with radio contrast dye, may be affected by partial volume effect.

3.4 MSCT IMAGE PREPROCESSING

Maintaining information details while reducing noise and artifacts is essential in the processing of ECG-gated MSCT images. However, the noise and metal artifacts in MSCT images cannot be accurately modeled into one specific distribution [3.8, 3.9]. When considering thin structures it can be difficult to distinguish informative anatomical/pathological features from noise/artifact. In the following we present some pre-processing methods reported in the literature to reduce metal artifacts and noise.

3.4.1 Metal artifact reduction

Metal objects in the region of interest cause inconsistencies of the acquired data set. During the image reconstruction using the standard filtered back projection (FBP), these inconsistent values lead to metal artifacts that overlay the whole image as star shaped streaks. To enhance the image quality and to ensure a correct diagnosis, metal artifact reduction (MAR) techniques are required. In the last three decades, many MAR methods have been presented. One popular strategy is the substitution of metal influenced Radon values with surrogate values [3.10]. This technique first separates metal data from uninfluenced values in Radon space. A re-computation of the influenced data is possible, e. g. using detector based interpolation [3.11], sinogram-gradient based interpolation [3.12, 3.13], wavelets [3.14] or an adapted inclusion of the metal influenced data [3.15]. However, even with high level interpolation residual inconsistencies may remain. Since the standard

FBP is very susceptible also to residual inconsistencies, a more appropriate reconstruction method is required to reduce or rather avoid metal artifacts.

Projection-based method for reducing metal artifacts caused by hip prostheses in multi-slice helical CT was presented [3.16]. The proposed method is based on reformatted projection, which is formed by combining the projection data at the same view angle over the full longitudinal scan range. Detection and segmentation of the metal were performed on each reformatted projection image. Two dimensional interpolation based on Delaunay triangulation was used to fill voids left after removal of the metal in the reformatted projection. The corrected data were then reconstructed using a commercially available algorithm. The main advantage of this method is that both the detection of the metal objects and the interpolations are performed on complete reformatted projections with the entire metal region.

3.4.2 Noise reduction

In order to reduce the noise in CT images a preprocessing step is usually implemented. The goal of this preprocessing is to increase the signal to noise ratio (SNR) as well as to increase the contrast of the structures of interest.

Classic smoothing filters, such as Median filter and Gaussian blur, may not give acceptable results. We present in the following some of the filtering approaches reported in the literature such as Hessian based filters and anisotropic diffusion filters that, in our opinion, could be interesting to reduce noise in MSCT images of thin structures.

3.4.2.1 Hessian based filters

This class of filters is also called “vessel enhancing filters”. They have strong abilities in keeping small vessel details while reducing noise in the image. Lorenz filter [3.17], Frangi filter [3.18] and Sato filter [3.19] were proposed for noise reduction and segmentation in medical images of vessels.

3D Hessian matrix is defined as follows:

$$H_\sigma = \sigma^2 \begin{pmatrix} \frac{\partial^2 u_\sigma}{\partial x^2} & \frac{\partial^2 u_\sigma}{\partial x \partial y} & \frac{\partial^2 u_\sigma}{\partial x \partial z} \\ \frac{\partial^2 u_\sigma}{\partial x \partial y} & \frac{\partial^2 u_\sigma}{\partial y^2} & \frac{\partial^2 u_\sigma}{\partial y \partial z} \\ \frac{\partial^2 u_\sigma}{\partial x \partial z} & \frac{\partial^2 u_\sigma}{\partial y \partial z} & \frac{\partial^2 u_\sigma}{\partial z^2} \end{pmatrix}$$

Where $u_\sigma = I * G_\sigma$ is the convolution between the original image and a Gaussian function.

$\lambda_1, \lambda_2, \lambda_3$ are the 3 matrix eigenvalues (they are defined as $|\lambda_1| < |\lambda_2| < |\lambda_3|$). The eigenvector associated with the smallest eigenvalue points out the direction with the smallest curvature of Hessian matrix (direction of vessel). Other 2 eigenvectors define a plane orthogonal to the vessel direction.

When considering voxels within an ideal tubular structure, the eigenvalues behave typically as follows:

$\lambda_1 \approx 0$, $|\lambda_1| << |\lambda_2|$, and $\lambda_2 \lambda_3 > 0$

Thus, the relations between the eigenvalues are summarized in table 3.2.

Tab. 3.2: Possible patterns in 2D and 3D, depending on the value of the eigenvalues (H=high, L=low, N=noisy, usually small). The eigenvalues are ordered as: $|\lambda_1| \leq |\lambda_2| \leq |\lambda_3|$ [3.18].

2D		3D			orientation pattern
λ_1	λ_2	λ_1	λ_2	λ_3	
N	N	N	N	N	noisy, no preferred direction
		L	L	H-	plate-like structure (bright)
		L	L	H+	plate-like structure (dark)
L	H-	L	H-	H-	tubular structure (bright)
L	H+	L	H+	H+	tubular structure (dark)
H-	H-	H-	H-	H-	blob-like structure (bright)
H+	H+	H+	H+	H+	blob-like structure (dark)

The vesselness function is defined as:

$v_0(s) = 0$ if $\lambda_2 > 0$ or $\lambda_3 > 0$ (the tubular is a dark structure)

$$v_0(s) = (1 - \exp(-\frac{R_A^{\,2}}{2\alpha^2}) \exp(-\frac{R_B^{\,2}}{2\beta^2})(1 - \exp(-\frac{s^2}{2c^2})) \tag{3.1}$$

Where:

$R_A = \frac{|\lambda_2|}{|\lambda_3|}$ and $R_B = \frac{|\lambda_1|}{|\lambda_2 \lambda_3|}$

are used to classify tubular structure and streak artifacts.

$S = \sqrt{\lambda_1^{\,2} + \lambda_2^{\,2} + \lambda_3^{\,2}}$ is used to classify vessel and non-stationary streak.

Because of the different size of arteries in images, the vesselness function is modified as:

$$v = \max_{\alpha_{\min} \leq \alpha \leq \alpha_{\max}} v_0(s, \alpha)$$

Where $\alpha_{\min}$ and $\alpha_{\max}$ are the minimum and maximum radius of arteries in original CT set.

Hessian based filters show a good adaptability to tubular structures such as vessels. But in the case of aortic valve prosthesis, some components, like leaflets, cannot be featured by cylindrical patterns.

3.4.2.2 Partial differential equations (PDE) based filters (anisotropic diffusion filters)

The anisotropic diffusion filters are non-linear filters based on partial differential equations. They have been proposed for noise reduction and segmentation in different types of cardiac images, especially in high level noise CT images and ultrasound images.

The main idea of anisotropic diffusion filters is that image features, such as discrete gradient, modified curvature or local variance, can be used to derive different intensities of diffusion in different directions.

Perona-Malik (PM) Model [3.20] was the first introduced anisotropic diffusion filter in 1990. All of other anisotropic diffusion filters were developed from this filter. In PM Model, the values of resulting voxels I_p^{t+1} are calculated as:

$$I_p^{t+1} = I_p^t + \frac{\lambda}{|\eta_p|}\sum_{q\in\eta_p} c(\nabla I_{p,q}^t)\nabla I_{p,q}^t \quad , \qquad (3.2)$$

where η_p is the neighborhood of the current voxel and $|\eta_p|$ is the number of voxels in η_p. I_p^t is the current value of the voxel. $\nabla I_{p,q}^t$ is the discrete gradient along the q[th] direction (defined by the current voxel and neighboring voxels). *c(x)* is the function used to control the rate of diffusion along different directions. It can take different expressions such as:

$$c(x) = \frac{1}{1+(x/k)^2} \quad \text{or} \quad c(x) = \exp(-(x/k)^2),$$

k is a parameter to control the diffusion intensity in directions. It is determined by the

intensity of noise. If the voxels are inside different objects, $\nabla I_{p,q}^t >> k$, $c(\nabla I_{p,q}^t) \to 0$, the processing of diffusion is stopped. If the voxels are inside the same object, $\nabla I_{p,q}^t \le k$, the diffusion is increased. The higher is k (use of a more strength diffusion), the more smoothed are the images after an iteration.

λ is an additional parameter to control overall diffusion intensity. It is determined by the level of noise. A quick diffusion ($\lambda = 1$) is set when the noise is low and a slaw diffusion is applied when the noise level is high.

Classical Anisotropic diffusion operators as PM model can enhance edge while denoising the image. The main drawback with PM model is the determination of the parameter k in the case of images with high level of noise. Thus, when the value of k is high to denoise the image, $c(\nabla I_{p,q}^t)$ and $\nabla I_{p,q}^t$ may give both high outputs for the noise voxels. After some iterations, some sharp impulse noises may appear. These impulse noises can not be smoothed by PM model itself.

Catté_PM model [3.21] was presented in 1992. It uses a Gaussian convolution function to improve the performance of PM model in case of strong Gaussian noise:

$$I_p^{t+1} = I_p^t + \lambda \sum_{q \in \eta_p} (\alpha_p^t + \alpha_q^t) \nabla I_{p,q}^t \qquad (3.3)$$

where：

$\alpha_p^t = c(|\nabla (G_\sigma * I)|)$, $G_\sigma(x) = (2\pi\sigma)^{-0.5} \exp(-x^2 / 4\sigma)$ is the Gaussian function with variance σ. "*" is convolution.

In addition to the strong assumption on noise distribution, which introduces a new parameter σ, the difficulty of determining the parameter k is not solved in Catté_PM model.

Fourth-order partial differential equation (F_PED) [3.22] was presented in 2000. It introduced fourth-order partial differential equation in the diffusion equation. This filter can reduce staircase but it may produce strong impulse noise (salt and pepper noise) during filtering.

To deal with impulse noise appearing during diffusion, *Anisotropic Median Diffusion* (AMD) model [3.23] introduced a median filtering after diffusion iteration:

$$I_p^{t+1} = \underset{q \in W}{Median}(I_p^{t+1}, I_q^{t+1}) \tag{3.4}$$

W is the neighborhood used in additional Median filter.

Tukey's Biweight function (also known as bisquare function) [3.24] was introduced to perform a piecewise-smoothing:

$\rho(x,\sigma) = \frac{x^2}{\sigma^2} - \frac{x^4}{\sigma^4} + \frac{x^6}{3\sigma^6}$ when $|x| < \sigma$ and $\rho(x,\sigma) = \frac{1}{3}$ in other cases. Fig 3.6 shows its curve.

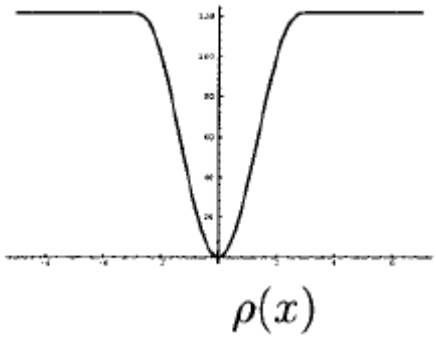

Fig 3.6: Curve of Tukey's Biweight function.

Because its good performance in terms of robustness and edge keeping, AMD model combined this function with c(x) to better control (and stop) the diffusion:

$$c(x) = 1 \text{ when } |\nabla I| \le k$$

$$c(x) = \frac{25}{16k}\left(1 - \left(\frac{\nabla I}{\sqrt{5}k}\right)^2\right)^2 \text{ when } k < |\nabla I| \le \sqrt{5}k \tag{3.5}$$

$c(x) = 0$ when. $|\nabla I| > \sqrt{5}k$

When the gradient is smaller than *k*, the neighboring voxel is considered to has a large probability to be inside the same object as the current voxel and the diffusion is not limited; When the gradient is between k and $\sqrt{5}k$, the probability is less and the diffusion is limited; when the gradient is bigger than $\sqrt{5}k$, it is considered that the neighboring voxel belongs to an other object and the diffusion is stopped.

Black et al. [3.24] also presented a method to determine parameter *k* using median absolute deviation (MAD):

$$k = \frac{1}{0.6745} median(|\nabla I_i| - median(\nabla I_i))|_{I \in ROI} \quad (3.6)$$

which is the MAD of the discrete gradient in the region of interest.

Kernel anisotropic diffusion (KAD) [3.25] was presented to preprocess images with high level of noise. It incorporates a kernelized gradient operator in the diffusion, leading to more effective edge detection and providing a better control of the diffusion process. The main drawback of this approach is the size of the kernel. The large size of the kernel required to reduce noise is not well adapted to the processing of thin structures.

Anisotropic Curvature Diffusion, which is based on a modified curvature diffusion equation (MCDE) [3.26-3.28], has been introduced to overcome impulse noise enhancement in anisotropic diffusion filter. In anisotropic curvature diffusion, the discrete gradient $\nabla I^t_{p,q}$ used in PM Model was replaced by a curvature function:

$$I_p^{t+1} = I_p^t - \frac{\lambda}{N} \sum_{q \in \eta_p} c(Curv(L^t_{p,q}))Curv(L^t_{p,q}) \quad (3.7)$$

where $L^t_{p,q}$ is the line defined by the current voxel and a direction given by a voxel of the neighborhood η_p. $Curv(L^t_{p,q})$ is the discrete curvature at the voxel along this line.

Vessel enhancing diffusions (VED) [3.29] use the diffusion direction based on vessel function defined by Frangi filter (introduced in section 3.4.2.1). The partial differential equation of VED can be expressed as:

$$I_p^{t+1} - I_p^t = div(D \times \nabla I_p^t) \tag{3.8}$$

Where:

$$D = Q\lambda' Q^T$$

Q is Eigenvector matrix of Hessian matrix.

Min-Max curvature flow [3.30, 3.31] was presented as a class of PDE-based algorithms suitable for image denoising and enhancement in 1995. These techniques are applicable to both impulse noise and full-image continuous noise. It applies a variant of the curvature flow algorithm on 2D images where diffusion is turned on or off depending of the scale of the noise that one wants to remove.

The value of voxels after filtering is defined as follow:

$$I_t = F(\kappa)|\nabla I| \tag{3.9}$$

$$\kappa = div\left(\frac{\nabla I}{|\nabla I|}\right)$$

Max min flow is defined as:

$$F(\kappa) = \begin{cases} \max(\kappa, 0) & \text{if } a(x,y) < G(x,y) \\ \min(\kappa, 0) & \text{otherwise,} \end{cases}$$

where a(x, y) is the average value of image intensity I(x, y) in a small neighborhood around the pixel (x, y), and G(x, y) is defined as the average intensity evaluated in the direction

perpendicular to the gradient direction.

And Min Max curvature flow is defined as:

$$F(\kappa) = \begin{cases} \kappa & \text{if } |\nabla I| < T \\ \min/\max \text{ flow} & \text{otherwise,} \end{cases} \quad (3.10)$$

where T is some threshold value set on the local gradient magnitude to enhance selected regions. Pixels at which the gradient magnitude is greater than T are preferred and are diffused using the min/max flow. The remaining points are diffused using the plain curvature flow.

Anisotropic diffusion filters may be suitable for reducing noise in MSCT data of bioprosthesis thanks to their ability of keeping the details of structures along different directions. The main drawback of these filters is their limited performance in case of high level noise. Although modified models introduced different features and improved diffusion equations, limitations still exist and have to be considered, especially in the case of cardiac MSCT images.

3.4.2.3 Noise reduction in LDCT images

Reducing dose during CT imaging is a new challenge. In recent years, some specific techniques have been proposed for improving the quality of Low Dose CT (LDCT) images which include very high level quantum noise.

For instance, a hybrid approach, making use of low-pass and directional filters from previously segmented regions (both non-structured and structured), has been described

[3.32].

In 2010, a filter named SharpView CT applies a multi-frequency analysis to divide the image into several subbands and separately process them before re-combination [3.33].

In 2011, a weighted intensity averaging over large-scale neighborhoods (WIA-LN) was proposed for processing abdominal LDCT images, which can be deemed as a large-scale nonlocal means (LNLM) [3.34].

The weighted large-scale averaging in the LNLM method relies on the information redundancy property within a local neighborhood to suppress mottled noise without obvious loss of image details. Nevertheless, the LNLM method is not effective in suppressing the non-stationary streak artifacts in thoracic CT images [3.34].

A qualitative and quantitative study performed on a thoracic phantom and a comparison with the HDCS filter [3.35] was reported. Results obtained on real data with an expert-based evaluation, show that the proposed method achieved effective noise/artifact reduction in thoracic LDCT images with little compromise in contrast.

3.5 IMAGE SEGMENTATION

Image segmentation is the process of partitioning a digital image into multiple sets of pixels, or segments. The objective is to change the representation of the image into a description that is more meaningful and easier to analyze [3.36]. It plays a major role in many medical imaging applications, by automating or facilitating the delineation, localization and characterization of anatomical structures and other regions of interest. A lot of segmentation methods have been reported in the literature. They are based on different kinds of approaches such as classification or thresholding, region-based segmentation, edge-based segmentation or a combination ot these approaches.

In the following we do not draw up an exhaustive presentation of the different methods. We focus on some of these methods which have been reported or could be used to segment cardiovascular CT images

3.5.1 Thresholding

Thresholding is the most simple and widely used segmentation approach [3.37]. It uses single threshold (image is segmented as object and surround) or multiple thresholds to segment voxels into different regions. These thresholds can be determined from the histogram of the image. The performance of this kind of approach is very limited in the presence of noise.

3.5.2 Region Growing

Approaches based on region growing compare features of neighboring voxels, such as local variance, difference of gray levels, texture, with those of current voxel to decide if the neighboring voxels could be included into the segmented region or not [3.38-3.41].

These approaches require one or several initial points (seeds) located inside the object of interest. In some cases (thin structures) the seeds must be precisely positioned. This initialization is usually manual. Neighboring voxels which are included into the segmented region are considered as new seeds and the process is iterated until no new seed can be included.

Region growing does not require the exploration of the whole image. The exploration process is driven by the data (seed points). If the criterion used for the aggregation of voxels is too selective a lot of seeds are required, especially in the presence of noise. In case of over-segmentation (small homogeneous sub-set) a fusion step has to be applied to recover the structures of interest.

3.5.3 Watershed segmentation algorithm

Vincent et al. presented Watershed segmentation algorithm in 1991 [3.42]. Watershed segmentation decomposes an image into regions which represent the influence areas of the intensity local minima. In analogy with topography, if the image is considered as an elevation map, each watershed region is a distinct catchment basin, separated from

adjacent basins by higher intensity ridges. For this reason, applying the watershed to a gradient magnitude image is a means of separating objects by their contours.

Watershed algorithm can deal with the segmentation of relatively large objects with smooth edges. In cardiac images, it was used to segment ventricular cavity [3.43-3.44].

3.5.4 Geometrical moments

3D geometrical moments can be used to characterize images. Moments of order *p,q,r* are defined as:

$$M_{p.q.r} = \int_x \int_y \int_z x^p y^q z^r f(x,y,z) dxdydz \tag{3.11}$$

where x, y, z are the voxel coordinates, and f is the image function.

Voxels in different kinds of structures have different features that can be described with these moments. They were used for the segmentation of surfaces [3.45]. This technique has also been to detect tubular structures in images. Analytical expressions have been developped to calculate features of local vessels in MRI [3.46]. In 2006, Bousse et al. applied these expressions to the characterization of vascular structures in CT [3.47].

3.5.5 Snake algorithm

The snake-segmentation algorithm is an iterative edge-based approach introduced by Kass [3.48] for the segmentation of 3D images.

A snake-contour is represented by a parametric curve v(s). The snake-contour is iteratively

adapted by a dynamic process which minimizes the energy E(v(s)). This energy can be composed of different terms including internal (snake curve) and external (image features) dynamic energies.

This kind of algorithm was largely used for the segmentation of medical images, such as the segmentation of vascular structures in ultrasound and CT images.

3.5.6 Level set algorithm

The level set segmentation algorithm was developed by Stanley Osher and James Sethian in the early 1987 [3.49], and has been improved in 2003 [3.50].

The level set is defined by a parameterized closed curve or contour. Curve propagation is controlled by an implicit function which is calculated from the positive values of the region outside the contour and the negatives values of the region inside the contour.

The level set algorithm represents an adaptive, flexible and efficient method that has been used in many medical imaging and diagnostic applications.

3.6 VISUALIZATION

In medicine, or in other areas, the objective is not only to give the perception of the data, but also to design tools to understand the underlying and relevant information they bring [3.51]. Two classes of rendering have been widely used in medical image visualization: surface rendering and volume rendering.

Surface rendering (Fig 3.7A) relies on a previous binarization, or segmentation, of the structures of the objects of interest and the tessellation of the surface initially described by sparse or dense 3D point sets, with our without organization (scattered points or multi-planar arrays). Surface renderings can also use voxel-based techniques: surface elements are indifferently voxels, faces of voxels or triangles estimated from the examination of the voxel neighborhood topology (Marching cube algorithm [3.52]). Surface tracking is then performed within the volume, binary or not, to extract the surface components. The rendering is be carried out by using either depth shading, or depth gradient or gradient shading [3.53].

Volume rendering (Fig 3.7B), provides the ability to display either surface, gray level values or both. In this case spatial circumscription (plane cutting for example), set operations (union, intersection, difference) and multistructure transparency effects can be easily done. A well known solution for volume rendering is ray tracing scheme [3.54]. Its implementation requires assignment of classification coefficients (opacity values) to each voxel, further combined with their radiosities. Fully transmission oriented renderings (maximum intensity projection [3.55], or voxel value accumulation) are also of interest and widly used in specific situations such as in cardiovascular imaging.

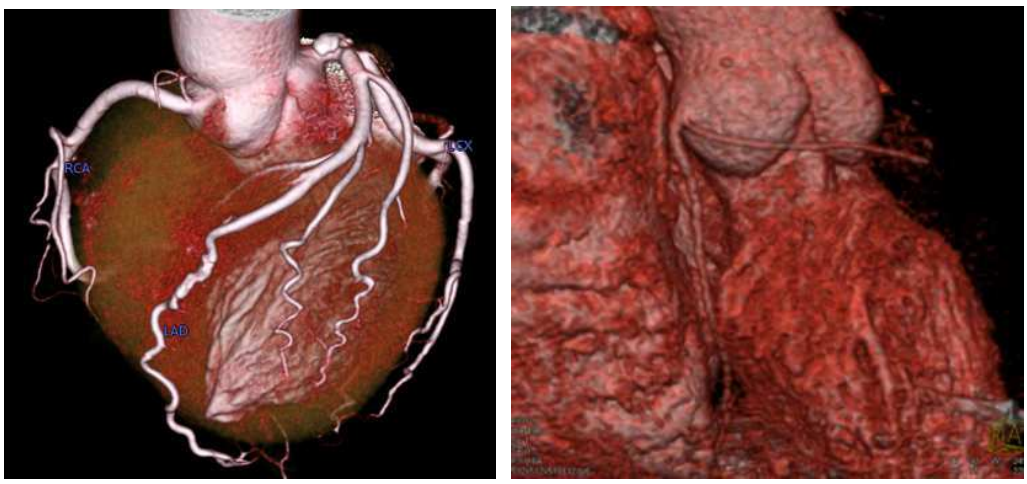

A B

Fig 3.7: Cardiac CT data visualization: surface rendering (A) and volume rendering (B).

3.7 CONCLUSION

In this chapter we tried to present the great variety of methods to obtain cardiac images, to reduce noise and to segment these images.

Looking at the clinical context we presented in chapter II, it becomes necessary to provide morphological images of aortic bioprostheses, easy to be realized and processed, in order to obtain information about anatomical images weakly contrasted.

MSCT scan images of the bioprosthesis can be easily obtained because all patients with a failing aortic bioprosthesis, waiting for reoperation or considered for a valve-in-valve procedure receive a MSCT for complementary information such as coronary assessment, cardiac structures relations or vascular assessment.

Currently, available software for CT images processing are not able to enhance prosthetic leaflets. Thus, in order to reach a morphological analysis of the bioprosthesis in aortic position we decide to improve some methods for images denoising and segmentation that we estimated able to enhance thin structures such as valve leaflets. In the next chapters we report our studied methods and their results.

3.8 REFERENCES

[3.1]. Hung J, Lang R, Flachskampf F, Shernan S.K, McCulloch M.L, Adams D.B, Thomas J, Vannan M, Ryan T. 3D Echocardiography: A Review of the Current Status and Future Directions. J Am Soc Echocardiogr 2007;20:213-233.

[3.2]. Sugeng L., Shernan S.K., Weinert L., Shook D., Raman J., Jeevanandam V., et-al. Real-time three-dimensional transesophageal echocardiography in valve disease: comparison with surgical findings and evaluation of prosthetic valves. J Am Soc Echocardiogr. 2008; 21:1347-54.

[3.3]. Hendee.W., Morgan.C., Magnetic Resonance Imaging Part I—Physical Principles. West J Med. 1984: 141 (4): 491–500.

[3.4]. Matthew J. B., Stephan A., Roger S. Blumenthal et al. Assessment of Coronary Artery Disease by Cardiac Computed Tomography. Circulation. 2006;114:1761-1791.

[3.5]. Desjardins B, Kazerooni E.A. ECG-Gated Cardiac CT. AJR:182, April 2004 : 993-1010.

[3.6]. Sun Z. Multislice CT angiography in cardiac imaging: prospective ECG-gating or retrospective ECG-gating? Biomed Imaging Interv J 2010; 6(1):e4.

[3.7]. Gardiner G W, Zoller P Quantum noise. Second Edition.

[3.8]. Bartuschat D. A parallel patch-based approach for the reduction of quantum noise in CT images. Master's Thesis of Friedrich-Alexander-Universitat Erlangen, 2008.

[3.9]. Mayer M. A variational approach for the reduction of quantum noise in ct images. Master's thesis, Friedrich-Alexander-Universitat Erlangen, 2007.

[3.10]. Veldkamp WJ, Joemai RM, van der Molen AJ, Geleijns J. Development and validation of segmentation and interpolation techniques in sinograms for metal artifact suppression in CT. Med Phys. 2010 Feb 37 (2): 620 – 628.

[3.11]. Watzke O. and Kalender W. A. A pragmatic approach to metal artifact reduction in ct: merging of metal artifact reduced images, Eur Radiol Physics, 2004; 14: 849 – 856.

[3.12]. Bertram M., Rose F., Schfer D., Wiegert J., and Aach T., Directional interpolation of sparsely sampled cone-beam ct sinogram data, in Proceedings of IEEE International

Symposium on Biomedical Imaging, 2004: 928 – 931.

[3.13]. Oehler M., Kratz B., Knopp T., Mueller J., and Buzug T. M., Evaluation of surrogate data quality in sinogram-based ct metal-artefact reduction, in SPIE Symposium on Optical Engineering - Image Reconstruction from Incomplete Data Conference, 2008:7076-07:1 – 10.

[3.14]. Zhao S., Robeltson D. D., Wang G., Whiting B., and Bae K. T., X-ray ct metal artifact reduction using wavelets: An application for imaging total hip prostheses, IEEE Transactions on Medical Imaging, 2000:19,12: 1238 – 1247.

[3.15]. Lemmens C., Faul D., and Nuyts J., Suppression of metal artifacts in ct using a reconstruction procedure that combines map and projection completion, IEEE Transactions on Medical Imaging, 2009: 28, 2: 250 – 260.

[3.16]. Yu L., Li H., Mueller J. Metal Artifact Reduction from reformatted projections for hip prostheses in multislice helical computed tomography: Techniques and Initial Clinical Results. Investigative Radiology: November 2009: 44, 11: 691-696.

[3.17]. Lorenz C., et al. Multi-scale line segmentation with automatic estimation of width, contrast and tangential direction in 2D and 3D medical images. In J. Troccaz, E. Grimson, and R. M¨osges, eds., Proc. CVRMed-MRCAS'97, LNCS, 1997:233–242.

[3.18]. Frangi A.F., Niessen W.J., Vincken K.L., and Viergever M.A.. Multiscale Vessel Enhancement Filtering. W.M.Wells et al. (Eds.): MICCAI'98, LNCS 1496, 1998: 130–137.

[3.19]. Sato Y., et al. 3D multi-scale line filter for segmentation and visualization of curvilinear structures in medical images. In J. Troccaz, E. Grimson, and R. Mösges, eds., Proc. CVRMed-MRCAS'97, LNCS, 1997: 213–222.

[3.20]. Perona P., Malik J. Scale space and edge detection using anisotropic diffusion. IEEE Transactions on Pattern Analysis and Machine Intelligence, 1990, 12(7): 629-639.

[3.21]. Catté F., Lions P., Morel J., et al. Image selective smoothing and edge detection by nonlinear diffusion. SIAM Journal on Numerical Analysis, 1992, 29: 182-193.

[3.22]. You Y., Kaven M. Fourth-order partial differential equations for noise removal. IEEE Transactions on Image Processing, 2000, 9(10): 1723-1730.

[3.23]. Ling J., Bovik A.C. Smoothing low-SNR molecular images via anisotropic median-diffusion. IEEE Transactions on Medical Imaging, 2002, 21(4): 377-384.

[3.24]. Black M.J., Sapiro G. , Marimont D.H., et al. Robust anisotropic diffusion. IEEE Transactions on Image Processing, 1998, 7(3): 412-432.

[3.25]. Yu J.H., WANG Y.Y., SHEN Y.ZH. Noise reduction and edge detection via kernel anisotropic diffusion. Pattern Recognition Letters, 2008, 29(10): 1496-1503.

[3.26]. Yezzi A. Modified Curvature Motion for Image Smoothing and Enhancement, IEEE Transaction on Medical Imaging, 1998, 7 (3).

[3.27]. Qian Y., Zhang Y., Morgan M. A comparison of medical image segmentation methods for cerebral aneurysm computational hemodynamics. Biomedical Engineering and Informatics (BMEI), 2011 4th International Conference, 2011, 2: 901-904.

[3.28]. Brassel M., Bretin E. A modified phase field approximation for mean curvature flow with conservation of the volume, Mathematical Methods in the Applied Sciences 2011, 34(10): 1157–1180.

[3.29]. Manniesing R., Viergever M.A., Niessen W.J. Vessel enhancing diffusion: A scale space representation of vessel structures. Medical Image Analysis, December 2006:10(6): 815–825.

[3.30]. Malladi R., Sethian J.A. Image Processing: Flows under Min/MaxCurvature and Mean Curvature. Graphical Models and Image Processing, March 1996:58(2): 127–141.

[3.31]. Yu H., Bennamoun M., Chua C.S. An extension of min/max flow framework. Image and Vision Computing March 2009: 27(4,3): 342–353.

[3.32]. Kalra M.K., et al. Can noise reduction filters improve low-radiation-dose chest CT images? Pilot study Radiology 2003: 228 257–64.

[3.33]. Martinsen A., Saether H., Olesen D., Wolff P. and Skaane P. Improved image quality of low-dose thoracic CT examinations with a new postprocessing software J. Appl. Clin. Med. Phys. 2010:11 250–58.

[3.34]. Chen Y. et al. Improving low-dose x-ray CT images by weighted intensity averaging over large-scale neighborhood Eur. J. Radiol. 2011: 80 e42–9.

[3.35]. Mendrik A.M. et al. Noise reduction in computed tomography scans using 3D anisotropic hybrid diffusion with continuous switch. IEEE Trans. Med. Imaging. 2009:28 1585–94.

[3.36]. L.Pham D, Xu C, L.Prince J. A Survey of Current Methods in Medical Image Segmentation. Technical Report JHU/ECE 99-01, Johns Hopkins Univ., 1998.

[3.37]. Sahoo P.K., Soltani S., Wang A.K.C., and Chen Y.C. A Survey of Thresholding Techniques. Computer Vision, Graphics and Image Processing, 1988, 41:233-260.

[3.38]. Boskamp T., Rinck D., Link, F., Kummerlen B., Stamm G., Mildenberger P. New vessel analysis tool for morphometric quantification and visualization of vessels in CT and MRI imaging data sets. Radiographics, 2004 24(1) :287–297.

[3.39]. Adams R. and Bischof L. Seeded region growing, IEEE Trans. Pattern Anal. Machine Intell. 1994, 16: 641-647.

[3.40]. Fan J., Yau D.Y., Elmagarmid A.K., Aref WG. Automatic image segmentation by integrating color-edge extraction and seeded region growing. IEEE Trans Image Process. 2001;10(10):1454-66.

[3.41]. Pohlman S., Powell K.A., Obuchowski N.A., Chilcote W.A., and Grundfest-Broniatowski S.. Quantitative classification of breast tumores in digitized mamograms. Medical Physics, 23:1337–1345, 1996.

[3.42]. Cheng J., Foo S.W., and Krishnan S.M. Watershed-Presegmented Snake for Boundary Detection and Tracking of Left Ventricle in Echocardiographic Images. Information Technology in Biomedicine, IEEE Transactions, April 2006:10 (2): 414 – 416.

[3.43]. Cristoforetti A., Faes L., Ravelli F., et al. Isolation of the left atrial surface from cardiac multi-detector CT images based on marker controlled watershed segmentation. Medical Engineering & Physics 30 (2008) 48–58.

[3.44]. Hahn H.K. and Peitgen H.O. IWT – Interactive Watershed Transform: A hierarchical method for efficient interactive and automated segmentation of multidimensional grayscale images, Proc. Medical Imaging, SPIE 5032, San Diego, Feb 2003.

[3.45]. Hamitouche C. Analyse d'images médicales tridimensionnelles, application a

l'extraction de structures anatomiques. PhD thesis, Universite de Rennes 1, mention Traitement du Signal, Telecommunication, Image, Radar, Rennes, France.

[3.46]. Reuze, P., Coatrieux, J.-L., Luo, L., and Dillenseger, J.-L. A 3d moment based approach for blood vessel detection and quantification in mra. Technology and Health Care, 1993:1 :181–188.

[3.47]. Bousse, A., Boldak, C., Toumoulin, C., Laguitton, S., and Boulmier D.. Coronary extraction and characterization in multi-slice computed tomography. ITBM-RBM, 2006: 27:217–226.

[3.48]. Kass D. A., Chen C. H., Curry C., Talbot M., Berger R., Fetics B. and Nevo, E. Improved left ventricular mechanics from acute vdd pacing in patients with dilated cardiomyopathy and ventricular conduction delay. Circulation, 1999(12):1567–1573.

[3.49]. Osher S. and Sethian, J.A. Fronts propagating with curvaturedependent speed: algorithms based on Hamilton-Jacobi formulations, J. Comput. Phys., 79(1):12–49, 1988.

[3.50]. Osher S. and Fedkiw R. Level set methods and dynamic implicit surfaces, vol. 153 of Applied Mathematical Sciences, New York, 2003.

[3.51]. Coatrieux JL, Haigron P, Dillenseger JL, Stanghellini I. From algorithms to applications in medical imaging. State of the art reports. Eurographics '96: 1 - 45.

[3.52]. Lorensen W. and Cline H. Marching cubes: A high resolution 3D surface construction algorithm. ACM SIGGRAPH Computer Graphics. July1987:21 (4): 163 – 169.

[3.53]. Luo L. Surface normal of 3D object display in cuberille environment. Engineering in Medicine and Biology Society, 1988: 1: 420-421.

[3.54]. Coatrieux JL, Toumoulin C, Hamon C, Luo LM. Future trends in 3D medical imaging. IEEE Eng Biol Magazine 1990;9(4):33–39.

[3.55]. Dillenseger J L, Rocha C, Coameux J L. Extension of the X-Image 3D Software to Epilepsy Applications. Engineering in Medicine and Biology Society, 1994. 1: 624-625.

IV - MATERIAL AND METHODS

4.1 PATIENTS SELECTION

In our study we selected patients previously submitted to surgical aortic valve replacement with a bioprosthesis, referred to our institution because of bioprosthesis degeneration and waiting for reoperation. Exclusion criteria were as follows: urgent operation, constant arrhythmia (atrial fibrillation or more than five premature heart beats per minute), New York Heart Association class IV heart failure, renal insufficiency (serum creatinine level greater than 1.4 mg/dL) and known allergy to iodinated contrast agents.

During a 3 years period, 9 patients with failing bioprosthesis and elected for reoperation were considered for the study. Among these, 4 patients were included according to selection criteria. Three patients were excluded for stable arrhythmia, 1 for heart failure with compensatory tachycardia and 1 for renal insufficiency.

Considered degenerated bioprostheses were represented by two Carpentier-Edwards Supra Annular Valve (23 and 25 mm), one 23 mm Edwards Perimount and one 23 mm Medtronic Mosaic. Bioprostheses types and echocardiographic characteristics are shown in table 4.1.

Tab. 4.1: Pre-operative echocardiographic assessment of studied bioprostheses.

Case	Bioprosthesis type	Bioprosthesis Size	Echocardiographic assessment
1 - HER	Edwards Perimount	23 mm	Mod-severe aortic regurgitation
2 - MAG	Edwards SAV	25 mm	Severe aortic steno-insufficiency
3 - BOU	Edwards SAV	23 mm	Severe aortic stenosis
4 - DAV	Medtronic Mosaic	23 mm	Normal

Depending on the case, the reoperation was performed from 7 to 19 years after implantation for different pathological reasons.

Case #1 - HER. The first case was a Edwards Perimount pericardial bioprosthesis, in which bovine pericardium is cut to reproduce aortic valve leaflets which are mounted on a complete metallic stent. Nine years after implantation the echocardiographic assessment showed a moderate-severe regurgitation (Fig. 4.1).

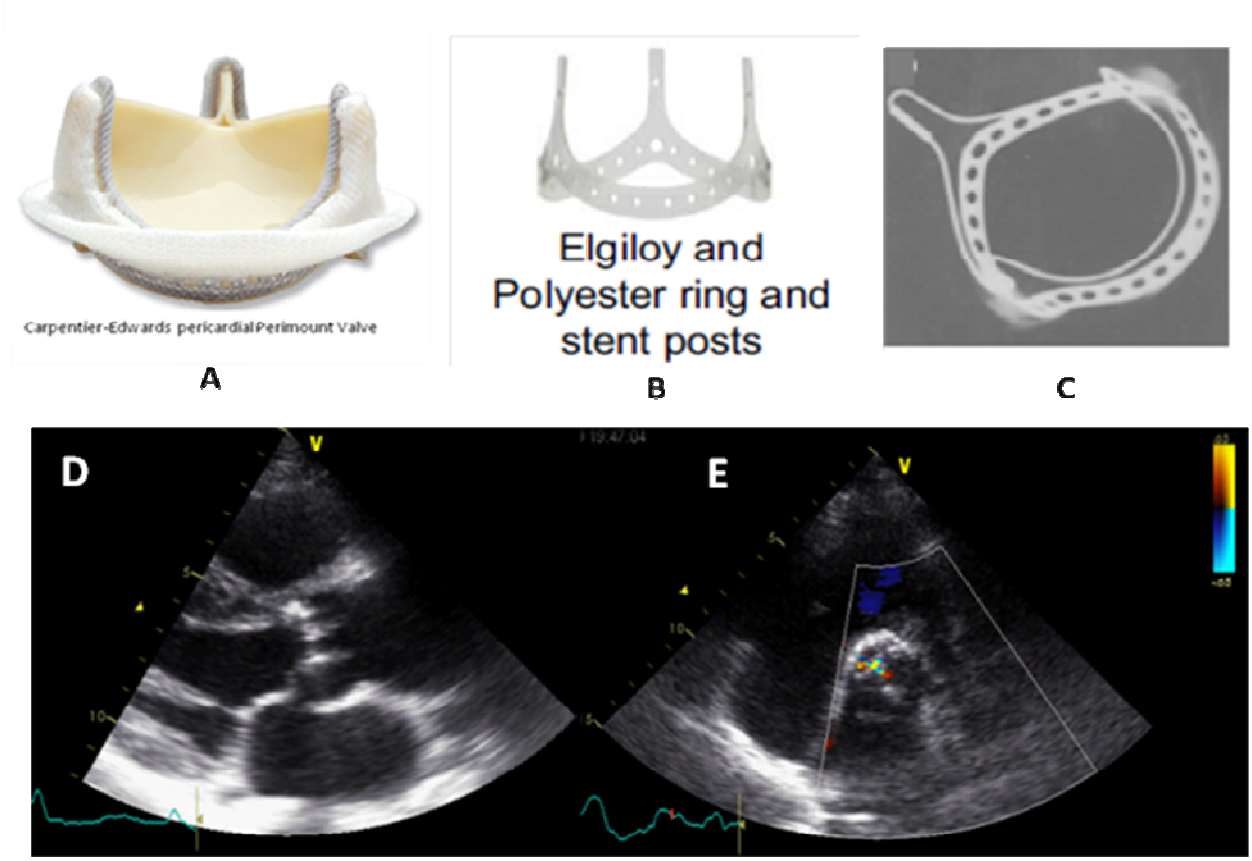

Fig. 4.1: case n°1 (A) pericardial bioprosthesis; (B) complete metallic stent; (C) stent radiology; (D) preoperative bidimensional echocardiography; (E) preoperative color Doppler echocardiography.

Case #2 - MAG. The second case was a Carpentier-Edwards SAV porcine bioprostheses in which a porcine aortic valve is mounted on a complete metallic stent. Echocardiography showed calcified leaflets associate to severe valve steno-insufficiency at 19 years from implantation (Fig. 4.2).

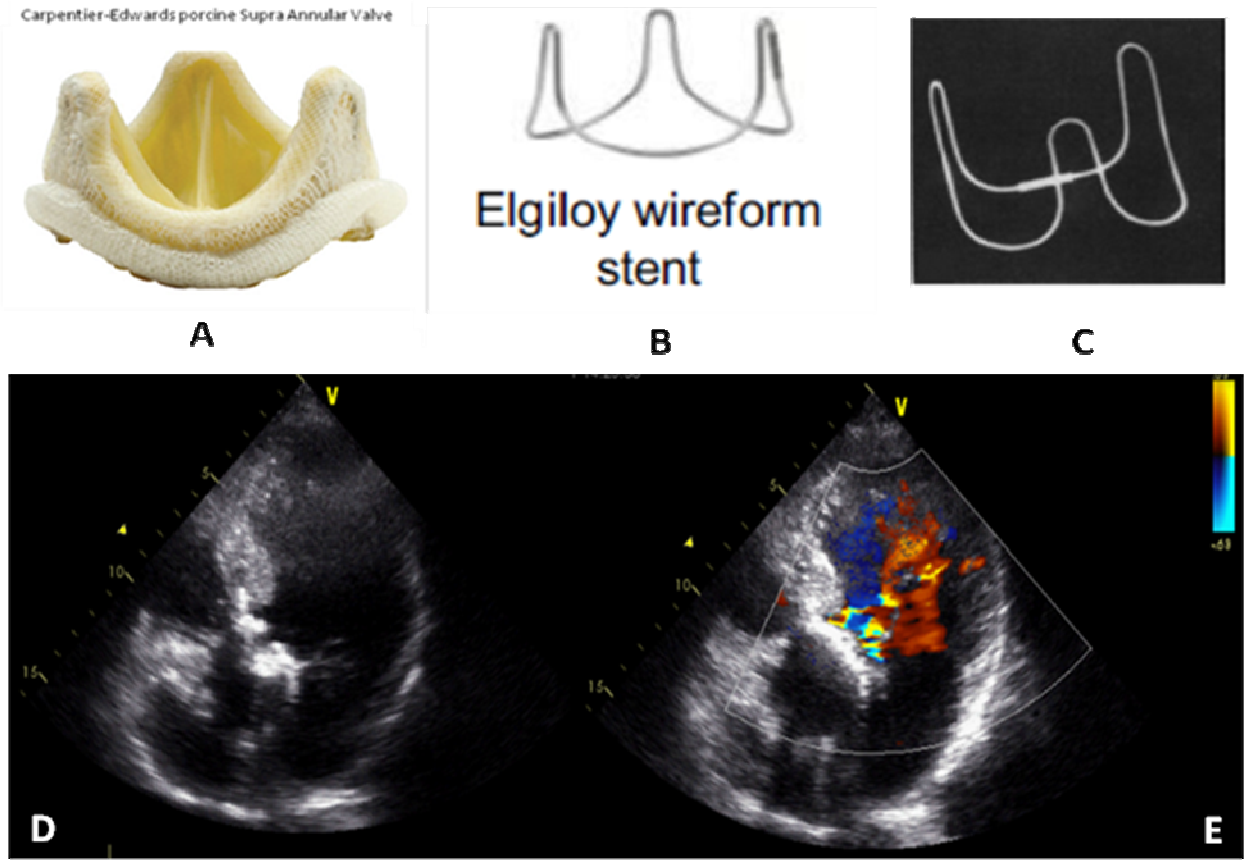

Fig. 4.2: case n°2 (A) porcine bioprosthesis; (B) complete metallic stent; (C) stent radiology; (D) preoperative bidimensional echocardiography; (E) preoperative color Doppler echocardiography.

Case #3 - BOU. The third case was a Carpentier-Edwards SAV porcine aortic valve (same as case 2 showed in Fig. 4.2 A-C) mounted on a complete metallic stent showing difficult leaflets analysis but associated to severe valve stenosis at echocardiographic assessment after 17 years (Fig. 4.3).

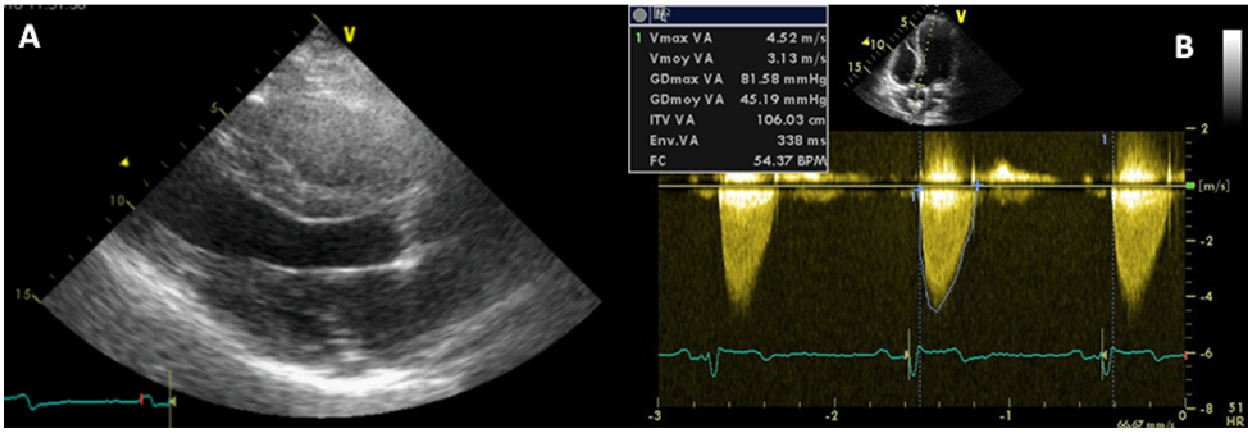

Fig. 4.3: Case n°3 (A) preoperative bidimensional echocardiography; (E) preoperative Doppler echocardiography.

Case #4 - DAV. The last case was represented by a Medtronic Mosaic porcine bioprosthesis mounted on incomplete metallic stent (Fig.4.4). This bioprosthesis was considered as normal at preoperative echocardiography and reoperation indication was represented by an infected ascending aorta pseudo-aneurysm, 7 years after implantation.

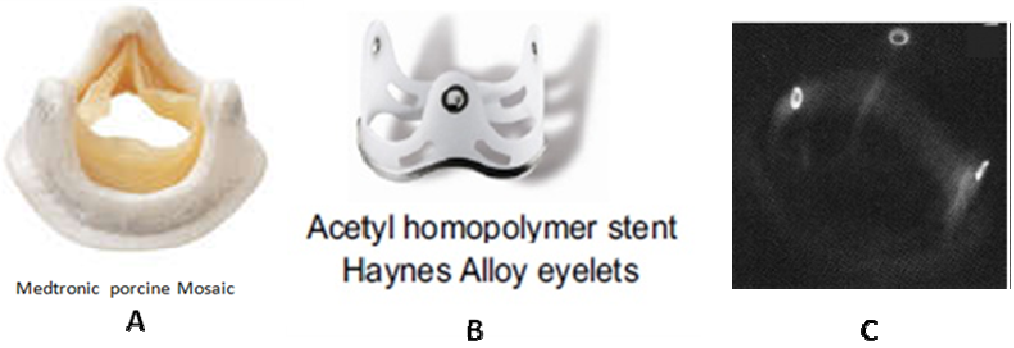

Fig. 4.4: case n°4 (A) porcine bioprosthesis; (B) incomplete metallic stent; (C) stent radiology.

4.2 ACQUISITION PROTOCOLS

The study protocol was approved by the institutional review board. Patients gave informed consent after being informed of the study, including radiation exposure information, prior to inclusion in the study.

Fig. 4.5: Discovery CT750 HD GE Healthcare

4.2.1 In-Vivo scanning protocol *(Coronary CT protocol)*

Included patients underwent preoperative ECG-gated cardiac multi-detector CT performed with a 64-section system (General Electric Medical Systems VCT 64 or Discovery 750HD (Fig4.5), GE Healthcare, Waukesha, WI). Patients with heart rate greater than 65 beats per minute received oral Bisoprolol 5 mg/day for 2 days prior to CT associated to intravenous Atenolol (intravenous bolus injection of 5 mg before exam) if they had no contraindication to beta-blocker administration.

The scanning direction was craniocaudal and extended from the level of the carina to the diaphragm. Prior to scanning, a technologist instructed all patients regarding breath holding in an effort to minimize changes in body posture during the examination.

The scanning sequence was as follows: topography was performed and was followed by a bolus tracking examination and two coronary CT angiography algorithms.

The intravenous bolus of contrast medium was tracked in the ascending aorta at the level of the pulmonary trunk every 2 seconds. The administered contrast medium was Iobitridol (Xenetix) (Guerbet Aulnay-sous-Bois, France) or Iohexol (Omnipaque) (GE Healthscare Healthcare, Inc. Princeton, NJ). The intravenous triple bolus was realized with 95 ml of contrast medium, followed by 45 ml of a mix of contrast and saline solution (50/50%) and finally rinsed by 30 ml of saline solution at 5 ml/sec. Individual body weight–adapted volume of contrast media and injection rate were not performed.

Retrospective CT angiography was performed with the following parameters:

helical scanning direction, 233-msec x-ray exposure time (two-thirds of the gantry rotation speed), 64 x 0.625-mm collimation, 0.35-second gantry rotation time, 100-kV tube voltage, 0.16–0.22 pitch and use of dose modulation (peak tube current of 750 mA during 0%– 90% of the R-R interval and minimal tube current of 300 mA) to reduce DLP (Dose Length Product in mGy x cm).

Retrospective reconstruction of multiple phases of cardiac cycle was performed. The diastole phase (70% of cardiac cycle) was considered as the best to study the aortic bioprosthesis with leaflets in their closed position.

4.2.2 Ex-Vivo scanning protocol *(Temporal bone protocol)*

After reoperation and intraoperative evaluation of the failure mechanism, CT-scan images of the isolated explanted aortic bioprosthesis were obtained using a high image resolution protocol with the following parameters:

64 x 0.3125-mm collimation, 1-second gantry rotation time, 140-kV tube voltage, 0.531 pitch and tube current of 170 mA.

4.3 VALVE PROSTHESES ANALYSIS

Multi Slice Computed Tomography (MSCT) shows a high spatial resolution and can also be used to acquire spatio-temporal data during the cardiac cycle. In this work we are interested in using MSCT data to analyse and to assess the morphology and the pathological features of aortic valve bioprosthesis including thin structures such as leaflets. Fig. 4.6 illustrates original noisy MSCT images showing stent with high density and possible artifacts (A), low contrasted leaflets (B), calcifications on leaflets (C) and pannus under stent (D).

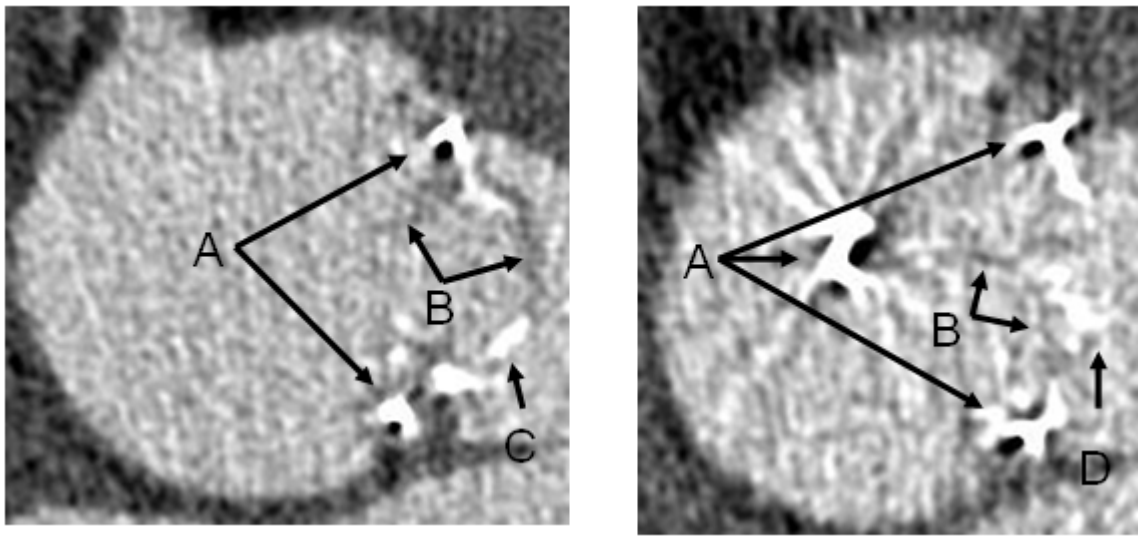

Fig. 4.6: Two MSCT slices of aortic valve prosthesis with high level noise, showing stent (A), leaflets (B), calcification (C) and pannus (D).

Because of their low density, leaflets (B) appear as dark structures in MSCT images. Due to their thin structure, they can be observed as regions of few voxels thickness in their non degenerated part. In addition images are altered by metal artifacts and noise that need to be reduced while keeping details of leaflets.

The overall approach (Fig. 4.7) proposed to analyze thin cardiovascular structures as

valve leaflets in MSCT data, is composed of: (a) the definition of a Region of Interest (ROI) depending on the type of bioprosthesis stent implanted in the patient, (b) a preprocessing step to reduce noise in the original CT images, (c) the segmentation of valve bioprosthesis components mainly based on a region growing process and (d) the visualization of the bioprosthesis components.

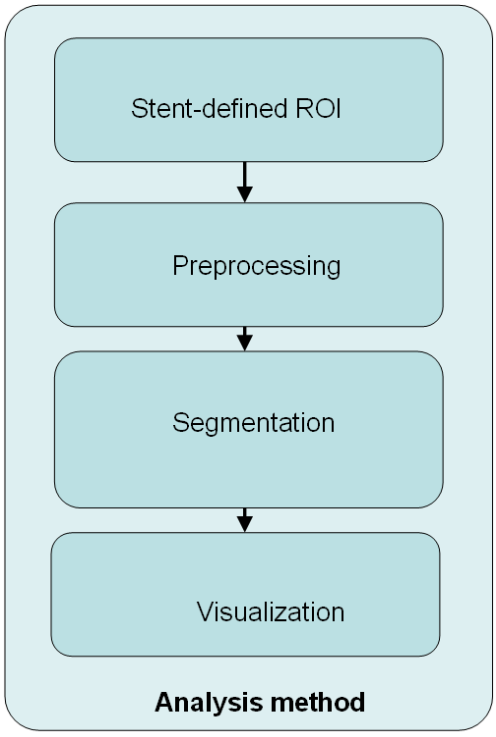

Fig 4.7: Bioprosthetic aortic valve analysis from MSCT data.

ROI definition

In order to deal with the above mentioned difficulties of segmentation in bioprosthesis CT images, we considered a region of interest (ROI). While this region should include all the structures of the bioprosthesis, it also should be as small as possible. In this region which has to fit to the bioprosthesis, decreasing the number of voxels may make denoising and segmentation much easier, and the amount of metal artifacts and false segmentations will be decreased.

We considered two kinds of shape for the ROI: a *cylindrical shape* preferentially for incomplete metallic stents (such as DAV introduced in section 4.1) and a *conformational shape* for complete metallic stents (such as HER, MAG and BOU introduced in section 4.1) (Fig. 4.8). These two kinds of ROI are both defined by the metal part of the bioprosthesis stent.(Fig. 4.9).

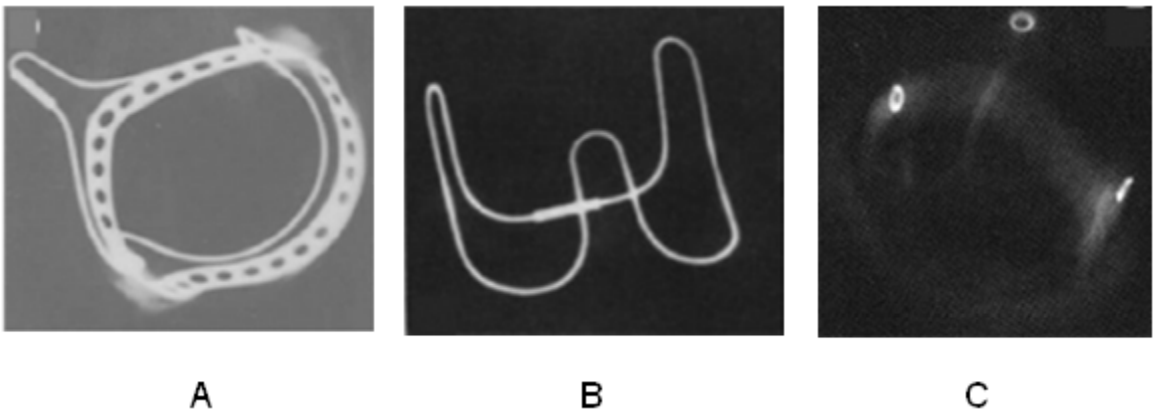

Fig. 4.8: Radiological images of bioprostheses with complete metallic stent (A and B) and incomplete metallic stent (C).

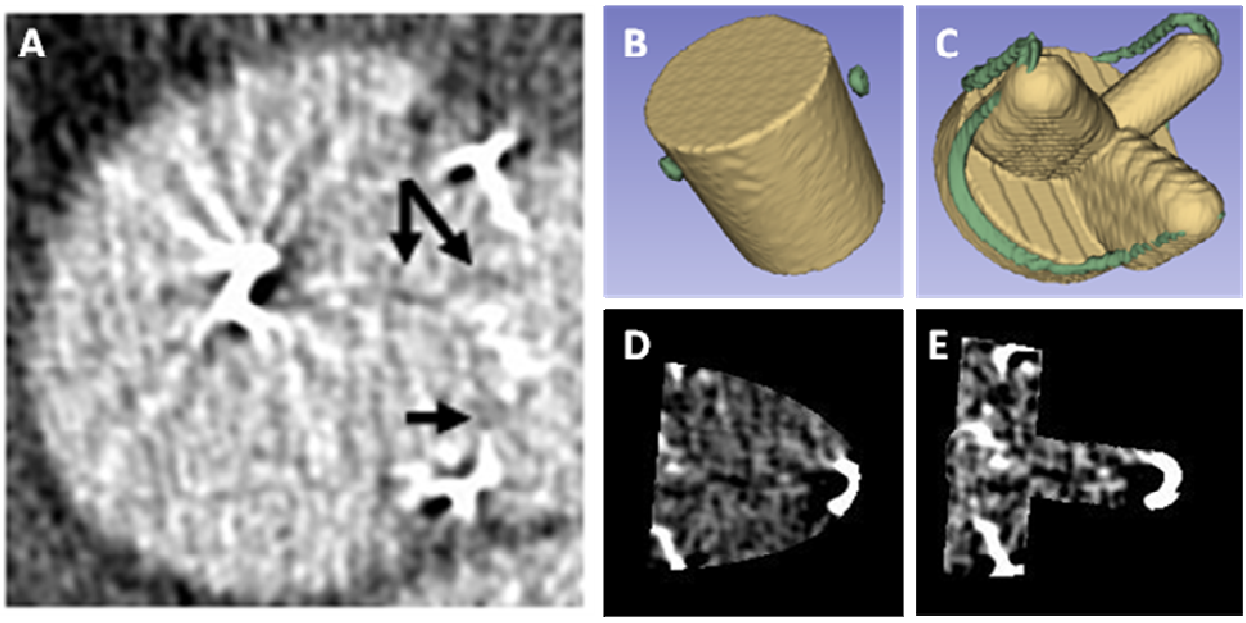

Fig. 4.9: Regions of interest: a slice in a classical cubic ROI (A), Cylindrical (B) and conformational (C) stent defined ROI, and illustration of the corresponding CT observations (D and E respectively) within one of the original CT slices.

In classical cubic ROI metal artifacts and noise textures in vascular lumen are difficult to distinguish from the leaflets (pointed by black arrows). In stent defined ROI the number of voxels is decreased. Metal artifacts outside the bioprosthesis structure are excluded by the ROI. During segmentations based on region growing, ROI can also limit the growing process in the volume image.

The parameters of the *cylindrical ROI* include the top surface position (the center of a cylindrical area), direction of the cylinder axis, radius and height of the cylinder. They are determined by the segmentation of the stent from preoperative (in-vivo) CT images. At this step, a coarse segmentation based on a simple operation of thresholding is performed.

The center of the top surface is obtained from the center of the 3 metal points of the incomplete metallic stent, and the cylinder radius is taken as the maximum distance between the metal points and the center.

The direction of the plane defined by the 3 metal points of the stent is used to determine the direction of the cylinder axis. The height of the cylinder is determined assuming a prior knowledge on the bioprosthesis features. In order to completely include the leaflets, without knowing the base of the bioprosthesis, a margin on the cylinder height was considered.

The *conformational ROI* is also estimated by considering a prior knowledge about the bioprosthesis. We assume that the type and the main geometrical features of the bioprosthesis placed in the patient are known. A simple geometrical model of the different structures is used to construct a volumetric model of the bioprosthesis. This model determines the conformational ROI. In this ROI the volume of the leaflets is expanded with spatial margins in order to take into account their alteration and their different spatial configurations resulting from their motion in in-vivo conditions.

The stent is used to fit the conformational ROI model to the bioprosthesis observed in the CT images. The metal part of the stent, which is characterized by high gray levels, is coarsely segmented thanks to a simple image thresholding operation. The parameters of the ROI, such as its size, position, direction and rotation can then be determined from the segmented stent.

A 3D Hough transform [4.1] is used to identify the bottom circle of the metallic stent (Fig.4.10), and thus to determine the position, radius, height and direction of the stent and ROI. The angular position is determined by detecting the missing parts of the basal part of the stent.

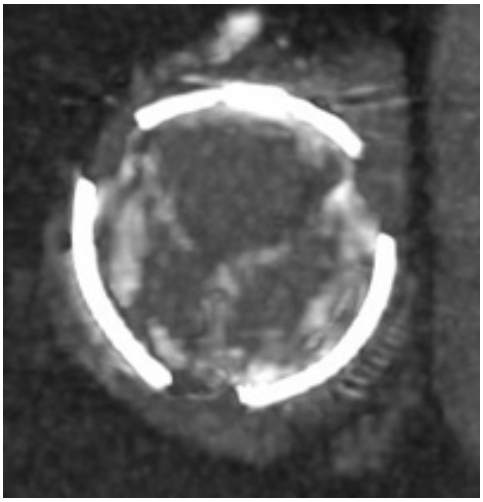

Fig 4.10: Circle of the metallic stent used to determine the features of the conformational ROI.

4.4 PREPROCESSING

As already mentionned, the level of noise in the considered MSCT images is high. The aim of the preprocessing step is to enhance the image, in other words to reduce the noise while keeping as much as possible the information on the structures of interest. To quantitatively assess this level of noise, we considered the signal-noise ratio (SNR). It is also used as a performance criterion to compare the image resulting from different image processing algorithms.

SNR shows the ratio between energy of signal and noise. Nevertheless, “energy” is difficult to define in the case of images. We used the definition given in [4.2]:

$$SNR = 10 * \log_{10}\left(\frac{Max(Var_i)}{Min(Var_i)}\right)\Big|_{i \in ROI} \quad , \qquad (4.1)$$

where Var_i is the local variance in the structures of interest. In this definition the maximum variance is assumed to be caused by the presence of an edge (energy of the signal) whereas minimum variance is caused by noise (energy of noise).

Due to their size and density, the critical components are the leaflets. Structures with high density, such as stent and calcifications, would drive to artificially high SNR values and could be un-relevant regarding valve leaflets. Thus, voxels representing stent, calcification and pannus are not considered in the computation of SNR. Voxels located at the boundary between leaflets and vascular lumen are used to obtain the maximum variance whereas voxels located in the vascular lumen are used to obtain minimum variance. Fig. 4.11 shows examples of MSCT images of bioprosthesis in four different cases: HER, MAG, BOU and DAV.

Compared with common MSCT images of the native valve, these images include a high level of noise. SNR varies from 6 to 8 in the case of bioprothesis whereas it is

about 15 in the case of the native valve.

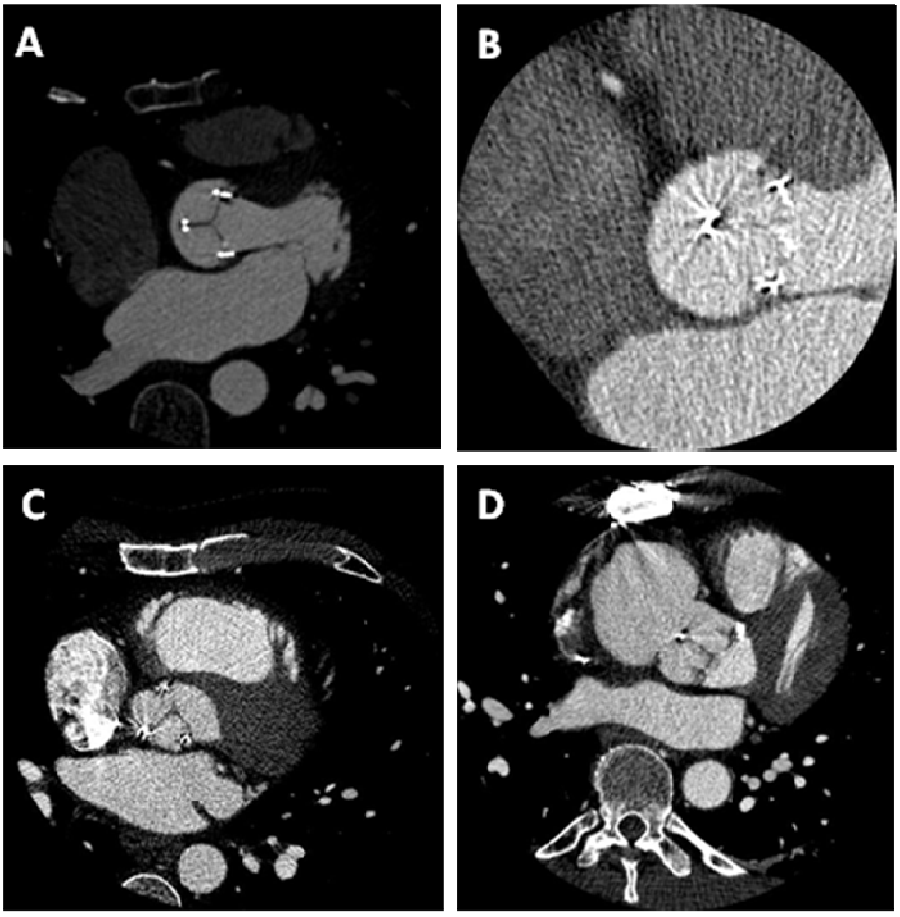

Fig 4.11: Slices form MSCT data sets: HER (A), MAG(B), BOU(C) and DAV(D).

In order to reduce noise and metal artifacts while retaining the details of thin structures like leaflets we focused on two kinds of filters thanks to their ability of directional analysis.

In Section 4.4.1, we describe how anisotropic diffusion filter can be applied and adapted to noise reduction in bioprosthesis images. Modified classifier based on Tukey's Biweight, median absolute deviation (MAD) and median filtering processes, as well as the determination of their parameters are more precisely presented.

In Section 4.4.2, we propose a new approach based on stick filter which was initially introduced to process ultrasound images. Features along sticks are used to classify voxels within different structures and different noise reducing processes are designed. Following the approach introduced by Frangi with the vesselness measure in the case of tubular structures, we introduce the notion “leafletness measure” in the stick filter.

4.4.1 ***Anisotropic Diffusion Filters***

Thanks to the ability of anisotropic diffusion filters to analyze densities in different directions, they have good performance particularly in the case of vascular images. High level of noise is a limitation of anisotropic diffusion filters. To improve their performance, robustness and impulse noise reduction, we used a modified diffusion process including Tukey’s biweight formulation, median absolute deviation (MAD) and median filtering, originally introduced in Anisotropic Median Diffusion (AMD) approach with PM model (section 3.4.2.2).

In most cases, the values of resulting voxels I_p^{t+1} in anisotropic diffusion filters can be written as:

$$I_p^{t+1} = I_p^t + \frac{\lambda}{|\eta_p|}\sum_{q\in\eta_p} c(F(I_{p,q}^t))F(I_{p,q}^t) \qquad (4.2)$$

where $F(I_{p,q}^t)$ is the operator chosen to characterize voxels values. It can be discrete gradient (PM model), Gaussian convoluted discrete gradient (Catté_PM model) or modified curvature (ACD). η_p is the neighborhood of the current voxel and $|\eta_p|$ is the number of voxels in η_p. We tipically considered a 3*3*3 cubic neighborhood. Larger

η_p may smooth edge too much, especially in image including high level noise.

c(x) is the function used to control diffusion rate (including the stop function). In all anisotropic diffusion filters we used the modified diffusion function introduced in AMD:

$c(x)=1$ when $F(I^t_{p,q}) \le k$

$$c(x)=\frac{25}{16k}(1-(\frac{\nabla I}{\sqrt{5}k})^2)^2 \text{ when } k < F(I^t_{p,q}) \le \sqrt{5}k \qquad (4.3)$$

$c(x)=0$ when. $F(I^t_{p,q}) > \sqrt{5}k$

where *k* is a parameter used to control the diffusion intensity in directions. It can be determined by the median absolute deviation:

$$k=\frac{1}{0.6745} median(F(I_i)-median(F(I_i)))|_{I_i \in ROI} \qquad (4.4)$$

where $F(I_i)$ denotes the features of all the voxels located in the ROI. Although edge voxels have features with higher values, they are much less than vascular lumen and leaflets voxels (about 5% or less). The inclusion of edge voxels in this calculating process should not affect MAD results. After each iteration, *k* should be refreshed. The number of iteration can be a critical parameter.

λ is the parameter to control overall diffusion intensity. Value of λ can be determined according to SNR. It was set at 1 (fast diffusion) for a low level of noise. In the case of images showing a high level of noise, λ was set at 0.5 (low diffusion).

In case of low SNR impulse noise may be amplified by the filtering process. All of anisotropic diffusion filters might have this drawback.

In order to reduce impulse noise (Fig. 4.12) generated by the filtering process (normally after 6 or 8 iterations), we introduced a median filter in the process:

$$I_p^{t+1} = \underset{q \in W}{Median}(I_p^{t+1}, I_q^{t+1}) \qquad (4.5)$$

where p indicates the noise voxel and q the neighboring voxel located in

neighborhood W.

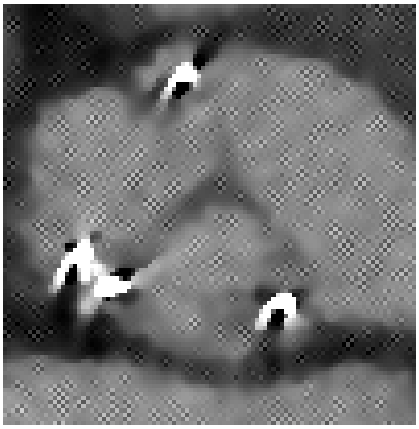

Fig. 4.12: impulse noises amplified during diffusion filtering.

Equations 4.1-4.4 introduced modified diffusion function, median absolute deviation and median filtering into anisotropic diffusion filter. In our experiments we used different models: PM, catté_PM, ACD models and min-max curvature flow.

4.4.2 Stick Filter

Original Stick filter is a non-linear filter which was presented as a boundary and line detector in 1998 [4.3]. The main idea of this filter is to divide the cubic neighborhood of the considered voxel into a set of sticks, and to use local features (variance, maximum difference between voxels, curvature) to combine intensities along the different directions of the sticks.

4.4.2.1 Original stick filter

Stick filter was first introduced to reduce strips-like noise in ultrasound images [4.4]. The neighborhood of the current voxel is divided into a set of sticks (Fig. 4.13) to perform a non-linear filtering of the image. The output I' at the current voxel is defined as:

$$I' = \frac{1}{W}\sum_{i=1}^{N} g_i \overline{I_i} \text{ and } W = \sum_{i=1}^{N} g_i \tag{4.6}$$

where $\overline{I_i}$ denotes the local mean value along the i^{th} stick, N is the number of sticks, $g_i = \frac{L}{\sum_{j=1}^{L}(I_{i,j} - \overline{I_i})^2}$ is the reciprocal of local variance along the i^{th} stick and *L* is the length of stick, used to classify edge and noise.

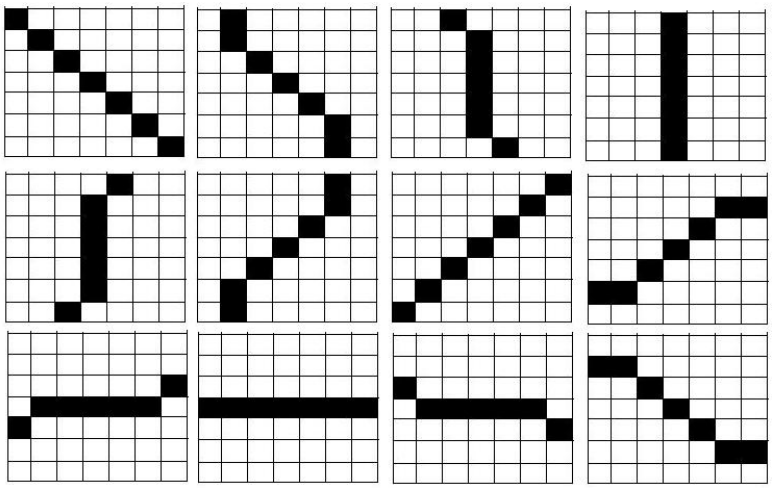

Fig. 4.13: 7 voxels-length 2D symmetric sticks set.

Stick filtering approach has also been used with a neighborhood divided into a set of asymmetric sticks (Fig. 4.14). Because of this asymmetric configuration, the filter

could get better performance in terms of keeping details of thin structure while denoising the image.

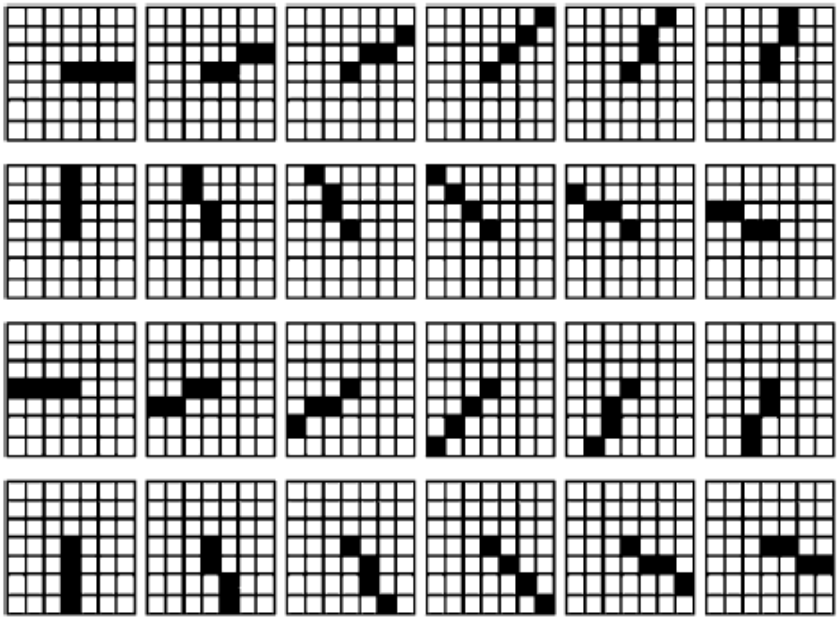

Fig. 4.14: 4 voxels-length 2D asymmetric sticks set

4.4.2.2 Stick based pre-processing

Local analysis of gray level changing along sticks could be helpful to classify the current voxels into different structures, such as leaflets, vascular lumen, noise and metal artifact. According to the measure designed to characterize the distribution of voxel values along the sticks, especially in the area of leaflets, different combinations of image values could be implemented to reduce noise and artifact and to enhance relevant information.

Classification of structures

We divided the cubic neighborhood of each voxel in the ROI into a set of asymmetric

sticks. The length of stick L should be longer than half of the thickness of leaflets observed in MSCT data, to make sure that for voxels inside leaflets, there is at least one stick crossing the edge between vascular lumen and leaflets.

Different gray level features are first measured along different configurations of sticks subsets according to prior knowledge about the morphological properties of the structures we want to classify.

In sticks set, the stick orthogonal to edge should have the shortest length inside leaflets. For the i^{th} stick we calculate the maximum MG_i of the magnitude of local differences of gray levels between the current voxel and j^{th} voxel along the stick:

$$MG_i = \max_{j=1}^{L}\left(\frac{|I_{i,j} - I_{i,1}|}{dis_{i,j}}\right) \tag{4.7}$$

where $dis_{i,j} = \sqrt{(x_{i,j} - x_{i,1})^2 + (y_{i,j} - y_{i,1})^2 + (z_{i,j} - z_{i,1})^2}$

We define S_M as the stick with the maximum *MG* value and S_m as the stick with the minimum *MG* value.

If there is no high variation of gray levels in the set of sticks, *i.e.* when MG_i is less than a threshold T_{MG}, we assume that the voxel belongs to the vascular lumen. If all of the sticks in the considered set show high variation of gray levels, *i.e*. when MG_i is higher than the threshold T_{MG}, we assume that we are in the case of an impulse noise voxel.

For the sticks with high *MG* values (sticks crossing edge), we select the stick S_M with the maximum *MG*. We assume the direction of this stick S_M is orthogonal to an edge. The current voxel and the direction given by S_M define a plane in which we consider a set of coplanar sticks S_{MC}. When the coplanar sticks S_{MC} have low *MG* values, *i.e. MG* values are less than the threshold T_{MG}, we assume that the current voxel is close to the edge of a thin structure like a leaflet. It can be located either inside this thin

structure, *i.e.* inside the leaflet, or outside the thin structure, *i.e.* inside the vascular lumen. (Fig. 4.15 A)

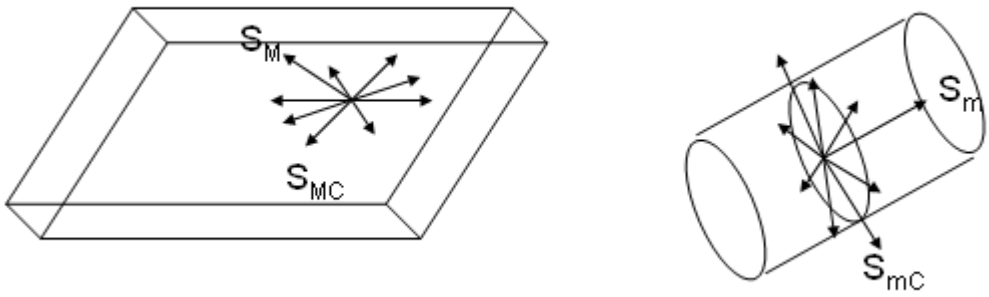

A B

Fig. 4.15: Sticks perform in thin structure (S_M /S_{MC})(A) and in tubular structure (S_m / S_{mC})(B).

Moreover small vessels or artifacts are characterized by tubular or elongated shapes. The sticks lying in this kind of structures should have low *MG* values. We consider in this case S_m, the stick with the minimum *MG* value defined previously. The current voxel and the direction given by S_m define a plane in which we consider a set of coplanar sticks S_{mC}. We assume that the current voxel belongs to a small vessel or an artifact when S_m has low *MG* value, *i.e. MG* is less than the threshold T_{MG}, while the coplanar sticks S_{mC} have high *MG* values, *i.e. MG* values are higher than the threshold T_{MG}.(Fig. 4.15 B)

The classification process can be summarized by the flowchart reported in Fig. 4.16.

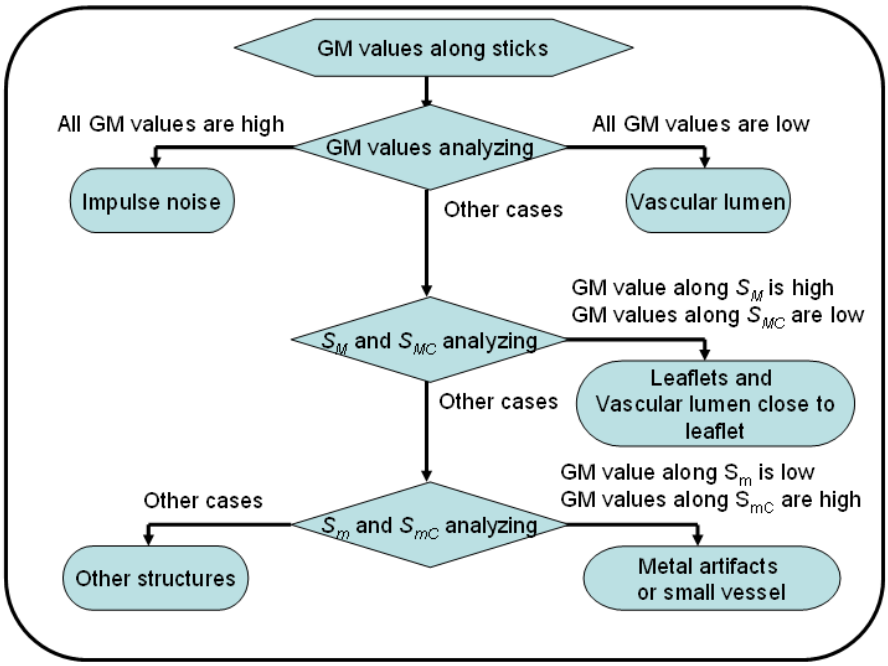

Fig. 4.16: Flowchart of classification of different structures in images.

Table 4.2 summarizes the heuristics used to design the classifier according to the features measured along the sticks: local mean along S_m, *MG* values along S_M and S_{MC}, *MG* values along S_m and S_{mC}.

Tab. 4.2: Possible structures depending on *MG* values along S_M, S_{MC}, S_m and S_{mC} sticks (H=high, L=low).

Possible structures	**Value of voxel**	***MG* values along:**			
		S_M	S_{MC}	S_m	S_{mC}
Vascular lumen	H	L	L	L	L
Leaflets	L	H	L		
Impulse noise		H	H	H	H
Small vessel or Artifacts		H		L	H
Others					

The "high" and "low" values of *MG* are fixed by the threshold T_{MG}. We propose to determine this threshold T_{MG} adaptively from the level of noise in the images. For the determination of T_{MG} we considered a cylindrical ROI. We estimate T_{MG} by calculating the median of *MG* values of all the sticks for all the voxels inside the cylindrical ROI:

$$T_{MG} = median(MG_i) \mid i \in ROIc \qquad (4.8)$$

Noise reduction

According to the classification of the structures described previously, different noise reduction processes have been implemented. We describe them for the different cases:

- Vascular lumen

The values of resulting voxels *I'* are obtained from the following Stick filter, which is a modified version of the original stick filter:

$$I' = \frac{1}{W}\sum_{i=1}^{N} g_i I_{Medi} \text{ and } W = \sum_{i=1}^{N} g_i \qquad (4.9)$$

where $I_{Medi} = \underset{j=1}{\overset{L}{median}}(I_{i,j})$ is the median value along the i^{th} stick. To reduce the staircasing due stick filtering, the weighting function g_i is given by the Tukey's biweight function:

$g_i = 1$ when $\text{var}_i \le k$

$g_i = \frac{625}{256k}(1-\frac{\text{var}_i}{5k})$ when $k < \text{var}_i \le 5k$ (4.10)

$g_i = 0$ when. $\text{var}_i > 5k$

$\mathrm{var}_i = \frac{1}{L}\sum_{j=1}^{L}(I_{i,j} - \overline{I}_i)^2$ with $I_{i,j}$, the value of the j^{th} voxel along the i^{th} stick.

The Mediane Absolute Deviation of local variances along all sticks inside the ROI is used to automatically determine k:

$k = \frac{1}{0.894} median(\mathrm{var}_i - median(\mathrm{var}_i))|_{I \in ROI}$ is given by absolute median diviation.

The filtering process is applied to the ROI. When part of stick is outside the ROI, we use original image voxels to complete it.

- Leaflets and vascular lumen close to leaflets

The stick filtering defined in equation 4.9 is applied here only on the set of S_{MC} coplonar sticks (sticks inside leaflet or vascular lumen). The stick filtering operation is then given by:

$I' = \frac{1}{W}\sum_{i=1}^{N} g_i I_{Medi}$ and $W = \sum_{i=1}^{N} g_i$ (4.11)

where I_{Medi} is the median value along the i^{th} stick, N' is the number of S_{MC} sticks ($N' = (2L-1)^2$), and gi is defined as previously.

- Impulse noise

To remove impulse noise, we use a median filter with a minimum size neighborhood (of size 3*3*3).

- Metal artifacts

We use a weighted-mean filter to reduce the metal artifacts. In Equation 4.5, we considered $g_i = 1$ for all the sticks. In this case, the stick filter became a weighted-mean filter with a cubic neighborhood η (width of 2L-1):

$$I' = \frac{\sum_{i=1}^{|\eta|} n_i I_i}{\sum_{i=1}^{|\eta|} n_i} \qquad (4.12)$$

n_i is the weight of the neighboring voxels. For a given voxel in the neighborhood, its resulting weight depends on the number of sticks including it. We tipically used 5-voxels length sticks.

This filter could also be used to enhance small vessels, like coronary vessels, but it is not the concern here.

- Other structures

For the structures not specifically identified in the classification process, and labelled as "others" we apply the filtering process expressed by Equation 4.9, which also used in the case of vascular lumen. Calcifications which are high density structures are considered, among others, in the class "other structures".

To summarize we designed a filtering process to reduce noise while keeping details of thin structures like leaflets. It is mainly based on modified stick filtering. The neighboring of the current voxel is divided in a set of asymmetric sticks along which the distribution of gray levels is used to classify this voxel into one of five categories (vascular lumen, leaflets, impulse noise, metal artifacts, other structures). This process can reduce high level noise while keeping most of details of leaflets. Thanks to the adequation between stick partitioning in 3D space and distribution of gray levels due to metal artifacts, this filtering process is well adapted to the reduction of these artifacts, with no need of interpolation in the Radon space.

4.5 SEGMENTATION

The issue of segmentation is more particularly focused on bioprosthetic leaflets and their degeneration. According to surgical expertise, four main classes of tissues were identified. They were related to Hounsfield Units (HU) measured by CT. We considered, from high to low HU, the following classes: stent, calcifications, vascular lumen and leaflets. The first element (stent), showing high CT values, can be easily segmented by thresholding.

Three kinds of region-based segmentation processes were implemented, with a decreasing level of user interactivity.

4.5.1 Interactive Region Growing

The first segmentation technique was an interactive process in order to provide a reference approach for the assessment of the results. It was based on classical isotropic Region Growing (IRG) method. Following a preprocessing step, as described above, it was applied using 3D Slicer software [4.5] (Fig. 4.17).

The bioprosthesis volume was interactively and roughly delineated from different CT slices. Multiple seed points (typically 20 seeds or more) were interactively selected for each component of the prosthesis. The region growing algorithm was started (26-neighbour connectivity) with automatic calculation of the criterion used for the aggregation of voxels. This similarity criterion was based on mean and standard deviation of the voxel values within the considered cubic neighborhood [4.5, 4.7, 4.8]. The extraction and visualization of the resulting 3D surface meshes delineating the

regions were performed by using the Marching Cube algorithm [4.6].

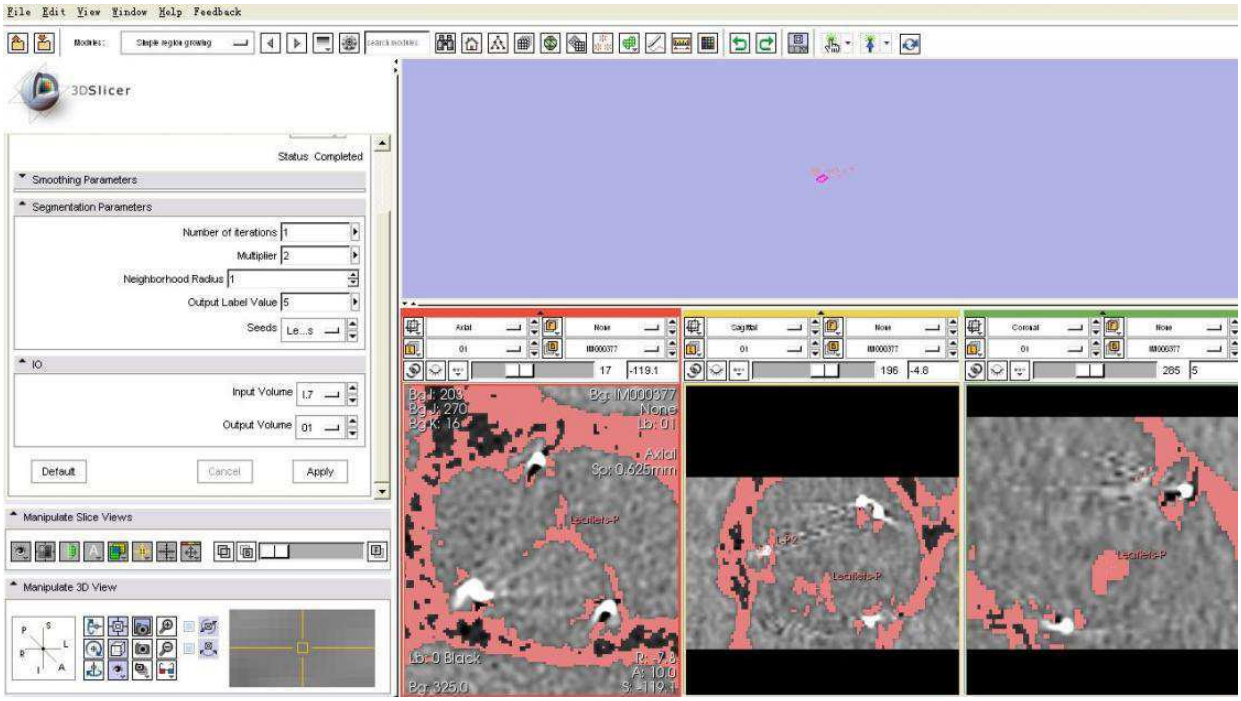

Fig. 4.17: Application example of Interactive Region Growing method by 3D slicer software.

4.5.2 Stick Region Growing

In the denoising step, we noticed that we can classify voxels inside thin structures such as aortic valve leaflets (both natural and bioprostheses) by considering gray level distribution along sticks. We also use features along sticks to determine the direction of region growing.

To deal with the segmentation of thin structures, like the components of a valve bioprosthesis and especially valve leaflets, we developed a directional region growing process based on stick neighborhood.

Some seeds were interactively selected inside the leaflets at different locations. A set of N voxels inside the leaflets was defined by considering for each seed the voxels belonging to their neighborhood.

To ensure region growth is not early stopped, or in other words to limit the number of seed points selection in some critical cases (highly noisy data), the size of the cubic neighborhood was chosen to be large enough to include space between homogeneous fragment of leaflets. We typically used a 342-connected neighborhood (7x7x7).

In order to examine each voxel in the cubic neighborhood of the seed, in the preselected and filtered ROI, the set of asymmetric sticks is analyzed.

We focus on two features, the normal direction to the edge and the mean value along stick S_m (the stick with minimum value among local maximum differences along the set of sticks).

For each voxel of the region growing cubic neighborhood we consider a stick neighborhood (as defined previously) to calulate the two features. For each stick, associated with a seed, we calculate the local maximum absolute difference MG_i (defined in section 4.4.2.2) of gray levels between the seed voxel and j^{th} voxels along the i^{th} stick:

$$MG_i = \max_{j=1}^{L}\left(\frac{|I_{i,j} - I_{i,1}|}{dis_{i,j}}\right)$$

where $dis_{i,j} = \sqrt{(x_{i,j} - x_{i,1})^2 + (y_{i,j} - y_{i,1})^2 + (z_{i,j} - z_{i,1})^2}$ is the distance between current voxel and j^{th} voxel. L is the length of stick as already defined

In the set of sticks with high MG values (sticks crossing edge), we select the stick S_{Ms} with the maximum MG value along seed's stick set and S_{ms} as the stick with the minimum MG value of seed's stick set.

As we supposed in section 4.4.2.2, the direction of this stick S_{Ms} is orthogonal to an edge, and S_{ms} lies within a thin structure. We calculate the normalized direction vector V_{Ms} corresponding to S_{Ms}, and the local mean value along S_{ms}.

Then, we select S_M and S_m for the i^{th} neighboring voxel of seed (marked as S_{Mi} and S_{mi}) and calculate normalized direction vector V_{Mi} of S_{Mi} and local mean value along S_{mi}.

We assume that a set of neighboring voxels located inside thin structures should have similar directions. According to this assumption, we calculate θ_i, which is the angle between V_{Mi} and V_{Ms}:

$$\cos\theta_i = \frac{V_{Ms} \bullet V_{M_i}}{|V_{Ms}| \bullet |V_{M_i}|} \qquad (4.13)$$

If i^{th} neighboring voxel is located in the same thin structure as its seed, this value should be close to 1, *i.e.* the neighboring voxel has similar S_M direction, or close to -1, *i.e.* the neighboring voxel has opposite S_M direction.

Leaflets don't represent an ideal thin structure: the regions with large surface curvature (*i.e.* $\cos\theta_i$ is close to 0) might stop the process of region growing (Fig. 4.18).

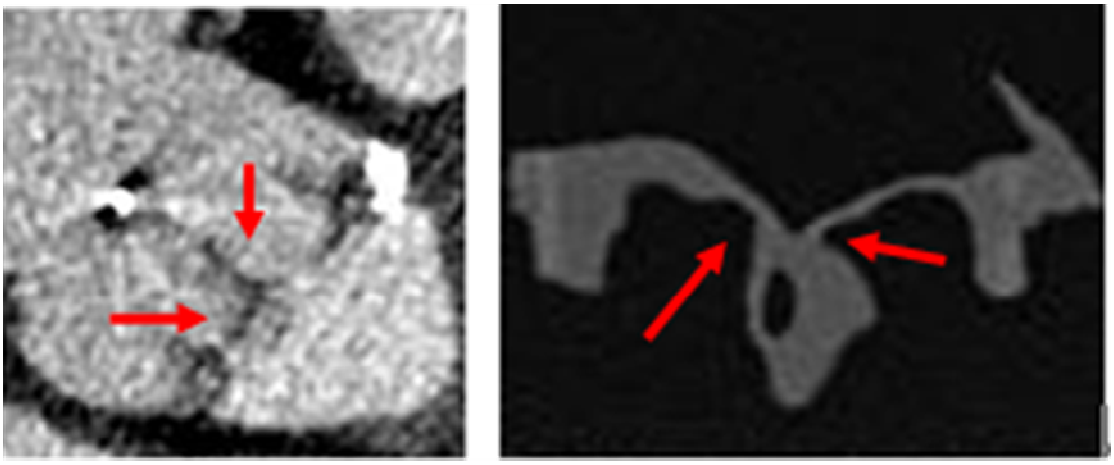

Fig. 4.18: Regions with large surface curvature (indicated by red arrows).

To ensure that the process of region growing is not stopped by this kind of regions, we set two or more seeds on each leaflet (on the commissure and bottom part).

As we discussed in section 4.4.2.2, vascular lumen voxels close to the leaflets could also show opposite directions between S_M and its seed, which is located in the leaflet. In this case, value of neighboring voxel should be considered.

Local mean values along the set of coplanar sticks $S_{MC,}$ which are used to classify structures in section 4.4.2.2, might be suitable to distinguish this kind of voxels from leaflet voxels, but it implies that all of S_{MC} sticks lye within the structure. Leaflet voxels close to edge may have a part of S_{MC} sticks crossing the edge, and may not have low local mean value. To ensure most of details on leaflet could be detected, we consider S_m rather than $S_{MC.}$

Leaflet voxels should have low local mean value $\overline{I_m}$ along S_{mi}, (S_m of the ith neighboring voxel) and vascular voxel should have high local mean value along S_{mi}.

The classification of local mean values along sticks is obtained by a thresholding operation. In this case the threshold T_{mean} is determined interactively from the histogram of local mean values along all the sticks in the conformational ROI. It is located between the modes corresponding to vascular lumen and leaflets.

By calculating these features, the neighboring voxels are classified as belonging to the region of the seed voxel (*i.e.* as a voxel of leaflet tissue) when: (i) $\overline{I_m}$ belongs to the gray level range of normal leaflets (*i.e.* lower than T_{mean}); (ii) directions (S_M) orthogonal to the edge are similar or opposed to thoses of their seeds (*i.e.* θ_i has a value close to 0 or 180 degrees). In this case they constitute new seed voxels. This process is iterated until no new voxel can be marked as a seed. This segmentation referenced as Stick Region Growing (Stick RG) in the following is preceded by a Stick filtering preprocessing step. The flowchart of Stick RG is shown in Fig. 4.19.

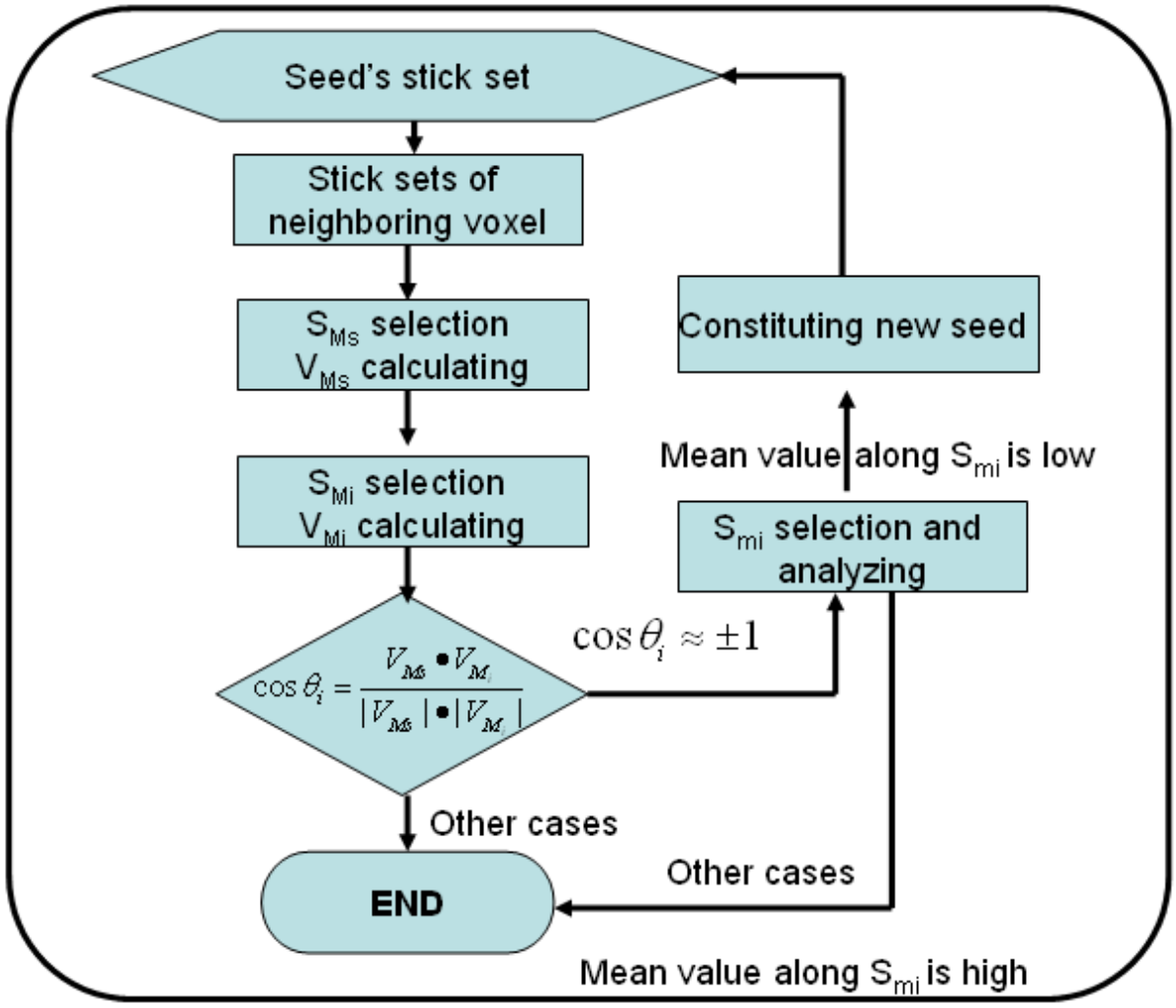

Fig. 4.19: Flowchart of stick region growing.

In the segmention of other tissues, $\cos\theta_i$ may give no contribution because of their morphology: tubular shape of stent, unknown shape of vascular lumen and of leaflet alteration. In the case of leaflet alteration, including calcification, there is a poor prior knowledge about the shape of the structure and different gray level distributions can be observed (according to the calcification degree). In the region growing process, we consider local mean value along S_m . If the stick S_m lies within the same structure, the local mean should be close to the value of the seed and the local variance should be low. The threshold parameters, concerning mean and variance, are obtained interactively from the gray levels of stent, calcifications and vascular lumen in the

preselected and filtered ROI.

We designed a region growing process to segment tissues in MSCT data of bioprosthesis. It is mainly based on the consideration of stick neighboring. Local mean values along sticks lying within structures are used in this region growing process. In addition, direction vectors orthogonal to the edge of structures are considered in the case of leaflets.

4.5.3 Stick Exhaustive Search

To further reduce the level of interactivity in the segmentation process, a systematic exploration of the ROI was implemented with no need for seed point definition. This segmentation referenced as Stick Exhaustive Search (SES) in the following was preceded by a Stick filtering preprocessing step.

We divide the neighborhood (Radius=3 pixels, 7*7*7 connected) of each voxel inside the ROI into a set of asymmetric sticks and we automatically select S_M, S_{MC}, S_m, *and* S_{mc} as we did in section 4.4.2.2. Thus, T_{MG} can be determined automatically by the median of *MG* values along all the sticks in the conformational ROI. Classification rules highlighted in Tab. 4.2 can be used to indentify voxels belonging to thin structures (including leaflets), vascular lumen, tubular structures (including complete metallic stent) and other structures (including calcifications and incomplete metallic stent).

Looking at sticks located inside ROI, we determine the thresholds T_{means}. T_{means} is a set of three thresholds used to refine the previous classification and to segment the following components of the bioprosthesis: leaflets, complete metallic stent (high local mean value along S_m), calcifications and incomplete metallic stent (higher local

mean gray level value along S_{mC} than vascular lumen). These thresholds are interactively determined from the gray level of stent, calcifications and vascular lumen in the preselected and filtered ROI.

With SES it is not necessary to re-select seeds interactively when the segmentation is not validated by the user. SES reduces interactivity but the results can be more influenced by noise than with Stick RG, especially in case of streak artifacts inside vascular lumen.

4.6 CONCLUSION

In this section we described some methods for bioprosthetic leaflets morphological analysis. Fig. 4.20 shows the proposed overall approach. The evaluation is reported in the next chapter.

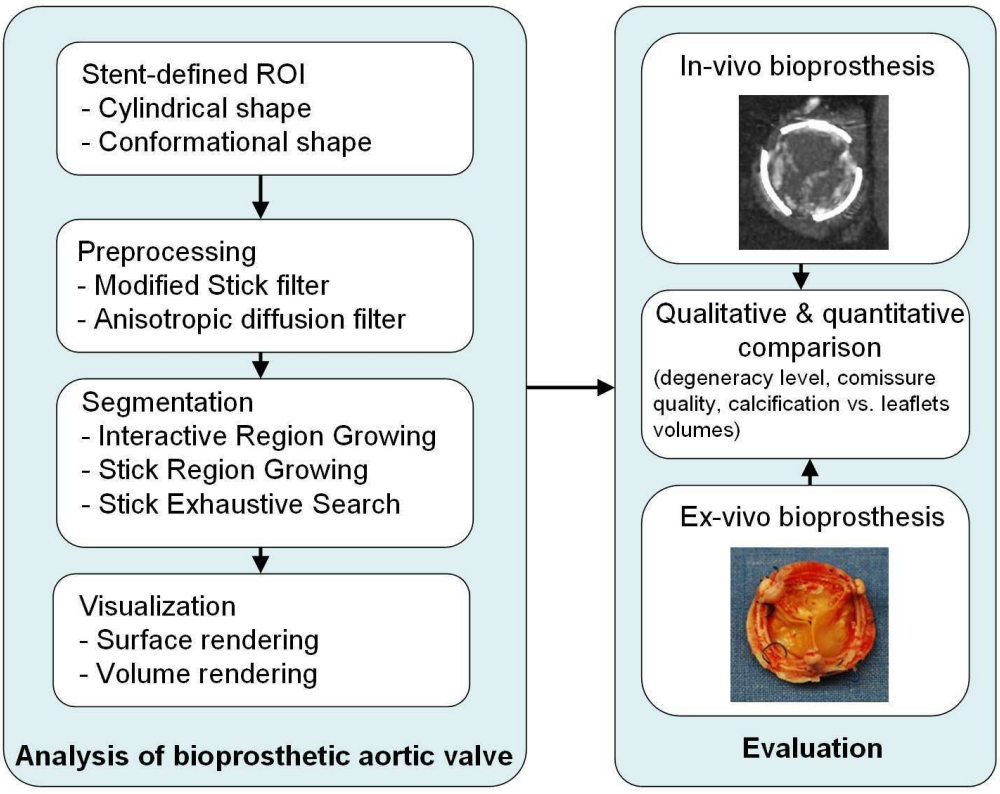

Fig. 4.20: Overall approach for bioprosthesis morphological analysis.

4.7 REFERENCES

[4.1]. Fernandes L, Oliveira M. "Real-time line detection through an improved Hough transform voting scheme," Pattern Recognition, Elsevier, Volume 41, Issue 1, pp. 299–314 (January, 2008).

[4.2]. González R C, Woods U. Digital image processing. Prentice Hall (2008).

[4.3]. Czerwinski R N, Jones D L. Line and boundary detection in speckle images, IEEE Trans. Image Processing 1998;7: 1700–1714.

[4.4]. Xiao C, Su Z, Chen Y. A Diffusion stick method for speckle suppression in ultrasonic images, Pattern Recognition Letters 2004; (25)16:1867-1877.

[4.5]. Ibáñez L. The ITK Software Guide –Second Edition November 21,2005.

[4.6]. Boskamp T, Rinck D, Link, F, K¨ummerlen B, Stamm G, Mildenberger P.. New vessel analysis tool for morphometric quantification and visualization of vessels in ct and mr imaging data sets. Radiographics, 2004 24(1) :287–297.

[4.7]. Adams R and Bischof L, Seeded region growing, IEEE Trans. Pattern Anal. Machine Intell. 1994, 16: 641-647.

[4.8]. Fan J, Yau DY, Elmagarmid AK, Aref WG. Automatic image segmentation by integrating color-edge extraction and seeded region growing. IEEE Trans Image Process. 2001;10(10):1454-66.

V – RESULTS AND DISCUSSION

In this section we firstly report peri-operative findings concerning the failure mechanism for each studied patient. Before the report of processing results we show the results, in terms of leaflet enhancement, coming from the CT workstation software. Finally we discuss segmentation results.

5.1 DEGENERATION ASSESSMENT AT REOPERATION

After reoperation explanted bioprostheses were analyzed in order to assess the real failure mechanism. Tab. 5.1 summarizes echocardiographic characteristics and failure mechanisms for studied bioprostheses.

Tab. 5.1: Echocardiographic assessment and intra-operative evaluation of failure in studied bioprostheses.

Case	Bioprosthesis type	Bioprosthesis Size	Echocardiographic assessment	Failure mechanism
1 – HER	Edwards Perimount	23 mm	Mod-severe aortic regurgitation	Calcified leaflet prolapse
2 – MAG	Edwards SAV	25 mm	Severe aortic steno-insufficiency	Calcified pannus/Leafl. tears
3 – BOU	Edwards SAV	23 mm	Severe aortic stenosis	Leaflet calcification
4 – DAV	Medtronic Mosaic	23 mm	Normal	Infection

We report the failure mechanism for each studied case.

Case #1. (HER) The pericardial degenerated bioprosthesis showed a calcified leaflet with associated prolapse as shown in Fig. 5.1 .

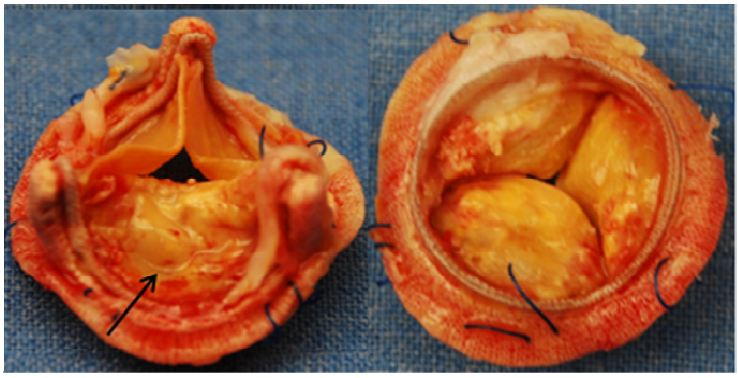

Fig. 5.1 : Case n°1 – explanted pericardial biopros thesis showing a calcified leaflet prolapse.

Case #2. (MAG): The porcine degenerated bioprosthesis was characterized by leaflet tears but also and especially by the presence of a strongly calcified subvalvular pannus overgrowth, responsible for a non structural valve dysfunction as shown in Fig. 5.2. The pannus was absolutely not detected at standard preoperative assessment.

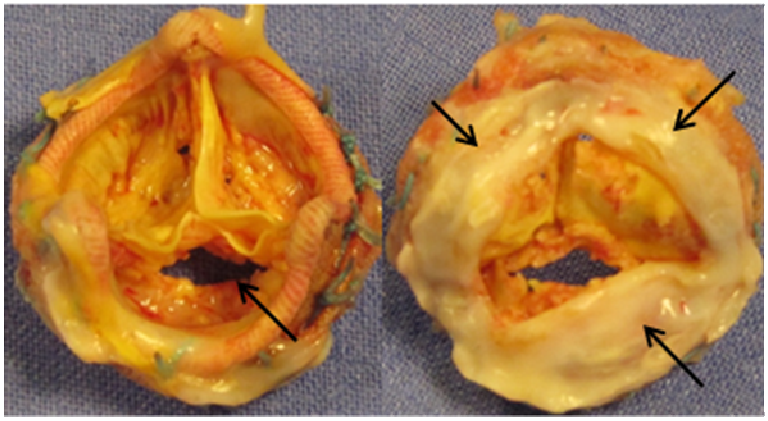

Fig. 5.2: Case n°2 – explanted porcine bioprosthesi s showing leaflet tear and calcified pannus.

Case #3. (BOU) The porcine degenerated bioprosthesis showed one leaflet calcification (Fig. 5.3) responsible for high preoperative gradients.

Fig. 5.3: Case n°3 – explanted porcine bioprosthesi s showing one leaflet calcification.

Case #4. (DAV) The porcine bioprosthesis showed leaflet thickening as starting process of infective endocarditis, absolutely not detected to preoperative assessment.

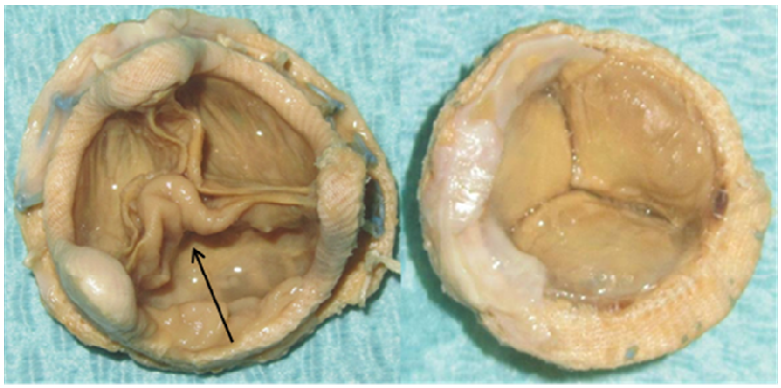

Fig. 5.4: Case n°4 – explanted porcine bioprosthesi s showing leaflet infection.

5.2 ACQUISITION AND WORKSTATION RESULTS

We obtained in-vivo and ex-vivo acquisition for all data sets. The main image resolution parameters derived from the CT acquisitions using the above mentioned protocols and retrospective reconstruction (in-vivo) are summarized in Tab. 5.2.

Tab. 5.2: image resolution parameters of in-vivo (IV) and ex-vivo (EV) acquisitions.

Patient	Observation	Image size (voxels in X,Y,Z)	Image sampling (mm in X,Y,Z)
HER	IV	512 512 281	0.3125 0.3125 0.625
	EV	512 512 198	0.3125 0.3125 0.3125
MAG	IV	512 512 105	0.318 0.318 0.312
	EV	512 512 110	0.0966 0.0977 0.312
BOU	IV	512 512 153	0.3632 0.3632 0.625
	EV	512 512 120	0.0977 0.0977 0.312
DAV	IV	512 512 290	0.418 0.418 0.635
	EV	512 512 125	0.0977 0.0977 0.3125

In-vivo original data were firstly processed using the General Electric Healthcare workstation and its software “AW Volume Share” (Advantage Workstation for Diagnostic Imaging) that showed, as known, reliable vascular and cardiac chambers reconstructions. But concerning the bioprostheses 3D analysis the workstation results were unsatisfactory, especially in terms of leaflet enhancement, because of highly noised images. Only visualization was possible. Fig. 5.5 shows some examples of volume rendering by CT workstation in studied cases. Obviously this visualization doesn’t allow a morphological characterization. Moreover, it is difficult to understand the composition of the altered leaflets.

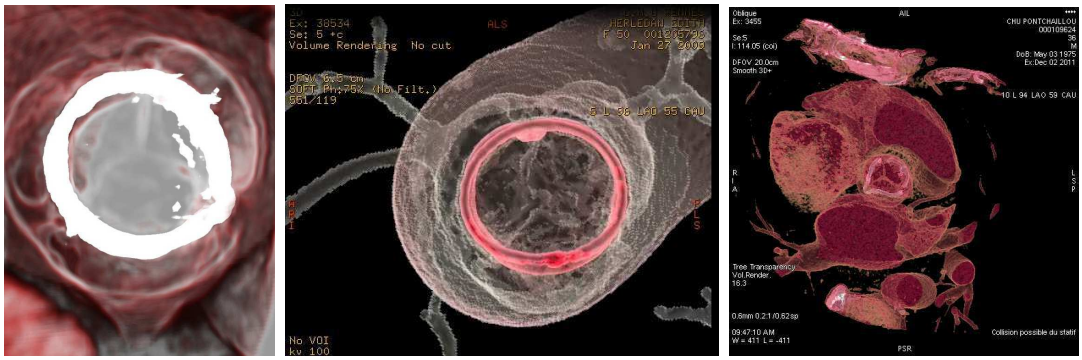

Fig. 5.5: volume rendering allows visualization but not a morphological characterization of leaflets.

Finally, in-vivo images were processed with proposed methods for noise reduction and segmentation, object of this study. In the following we report our results.

5.3 DENOISING

Preprocessing to reduce noise is necessary only for in-vivo images. The structures of interest (stent, leaflets and calcification/pannus) were well contrasted in ex-vivo images and they did not need to be preprocessed. Examples of original in-vivo images for the four considered cases are shown in Fig. 5.6.

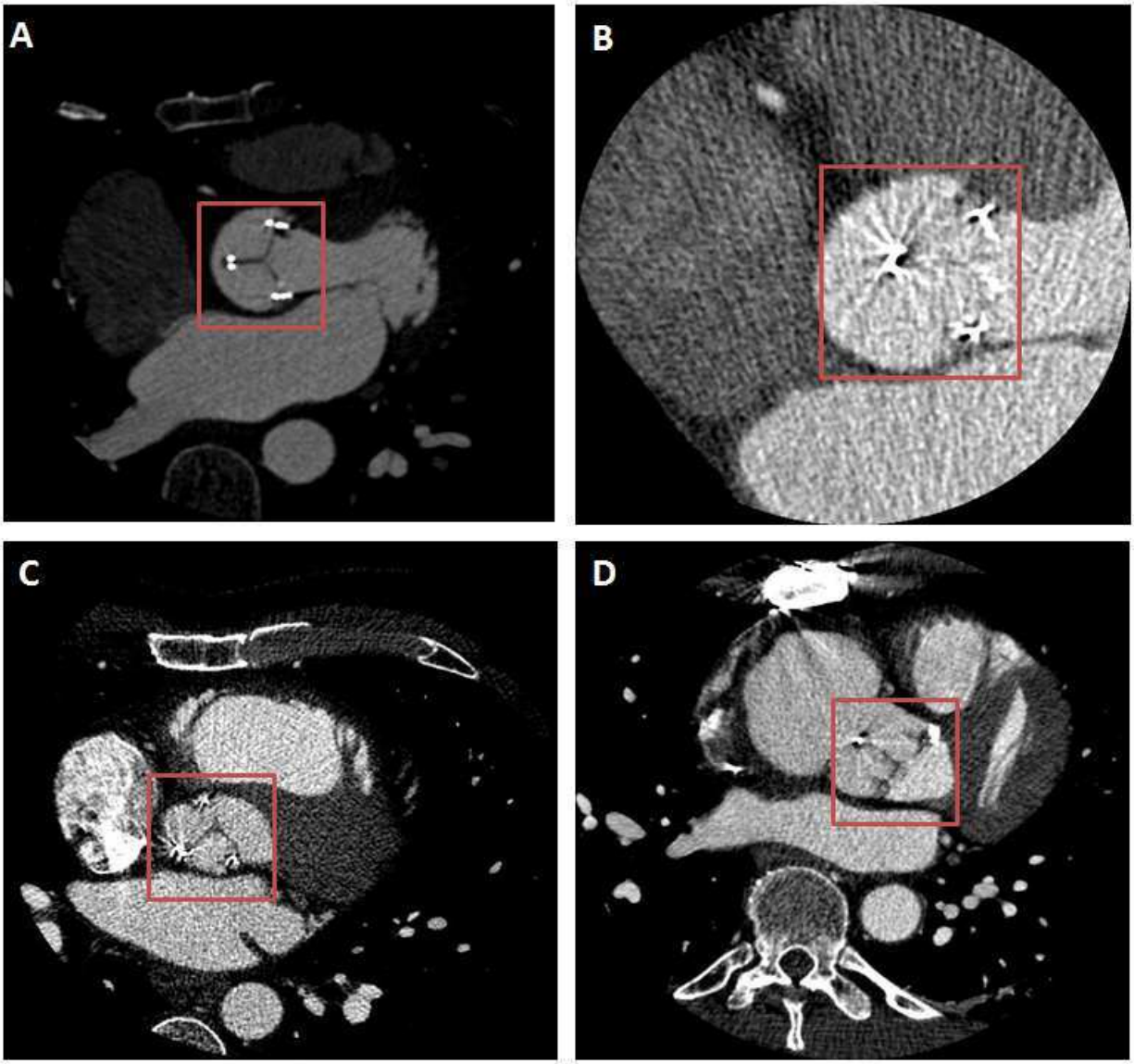

Fig. 5.6: Examples of original images: HER (A), MAG (B), BOU (C) and DAV (D). Regions located in the red square include the bioprosthesis.

The bioprosthesis volume was first isolated by considering the ROI defined by the stent in in-vivo images. Then, the preprocessing based on a simple classical median filter, on anisotropic diffusion filters (PM, Catté_PM, MmCF and ACD) and on stick filters (Original Stick, Modified Stick) was applied to the in-vivo CT volumes of the four patients. Resulting images obtained with the 7 different filters are reported in Fig. 5.7a-5.7d.

A first qualitative appreciation of the results lets appear that the approach based on the modified stick filter seems to best enhance the contrast between valve leaflets and surrounding structures.

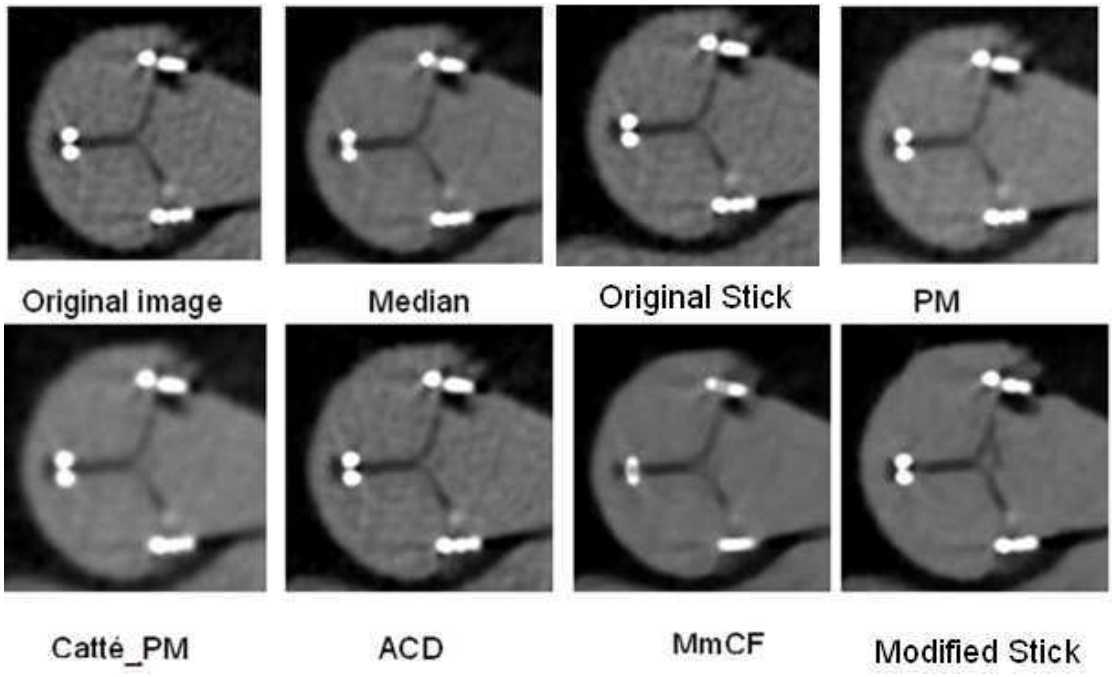

Fig. 5.7a: Filtering of case 1 - HER (original image and results obtained with the 7 different filters).

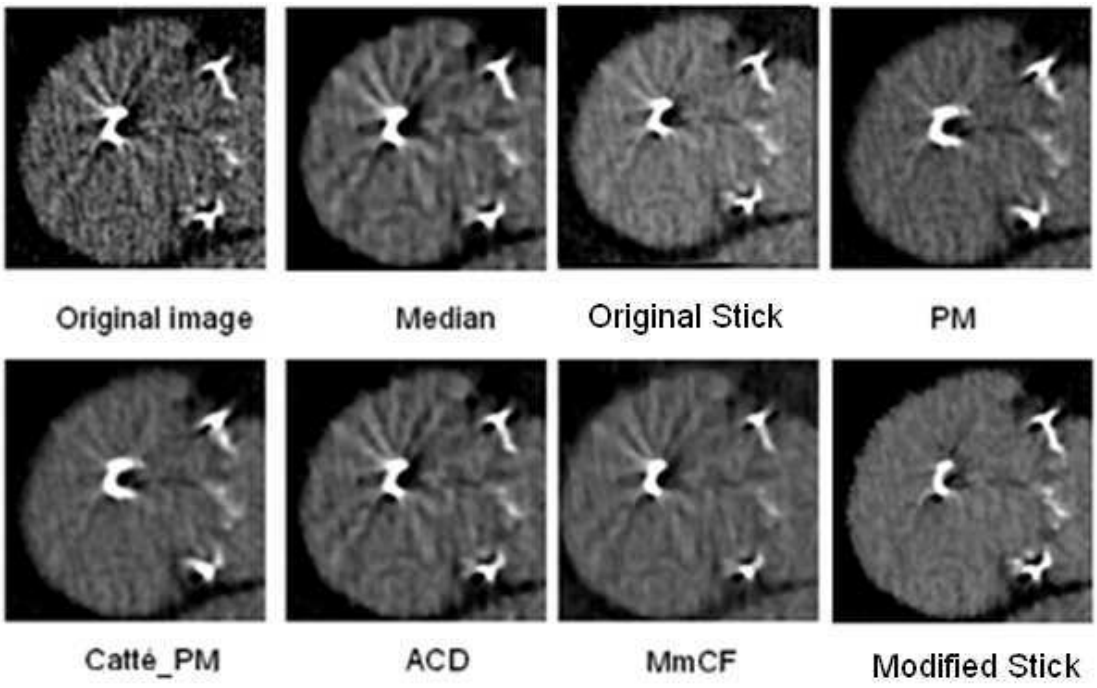

Fig. 5.7b: Filtering of case 2 - MAG (original image and results obtained with the 7 different filters).

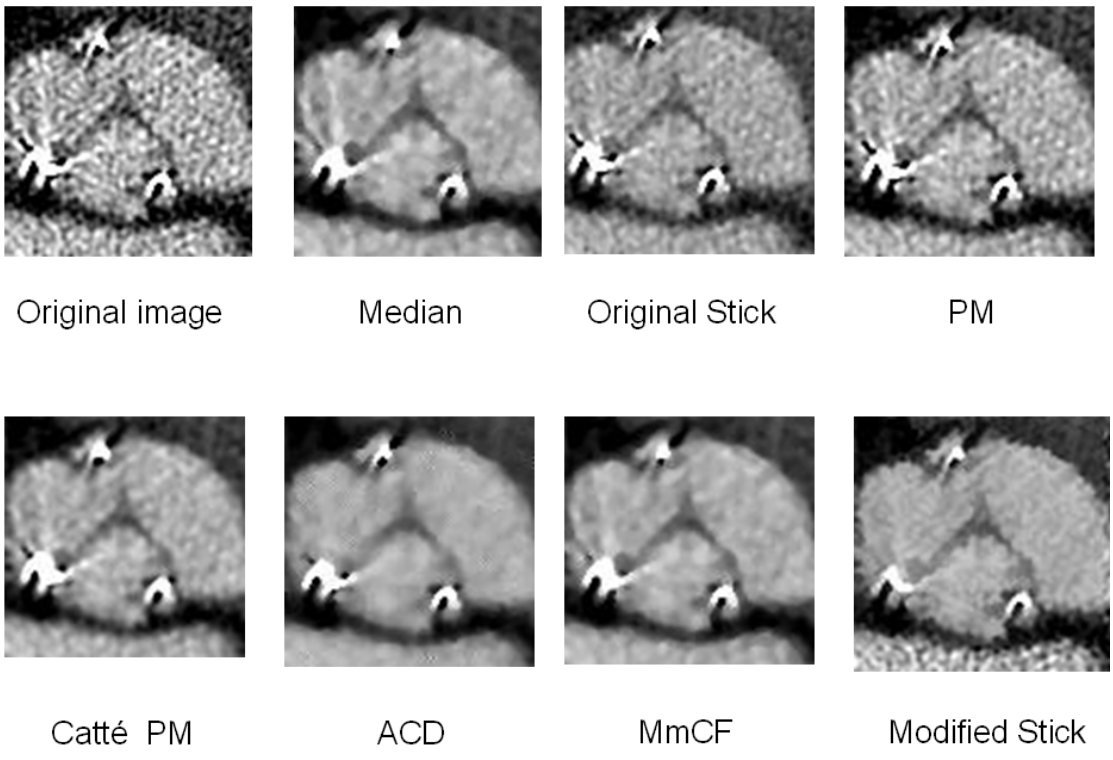

Fig. 5.7c: Filtering of case 3 - BOU (original image and results obtained with the 7 different filters).

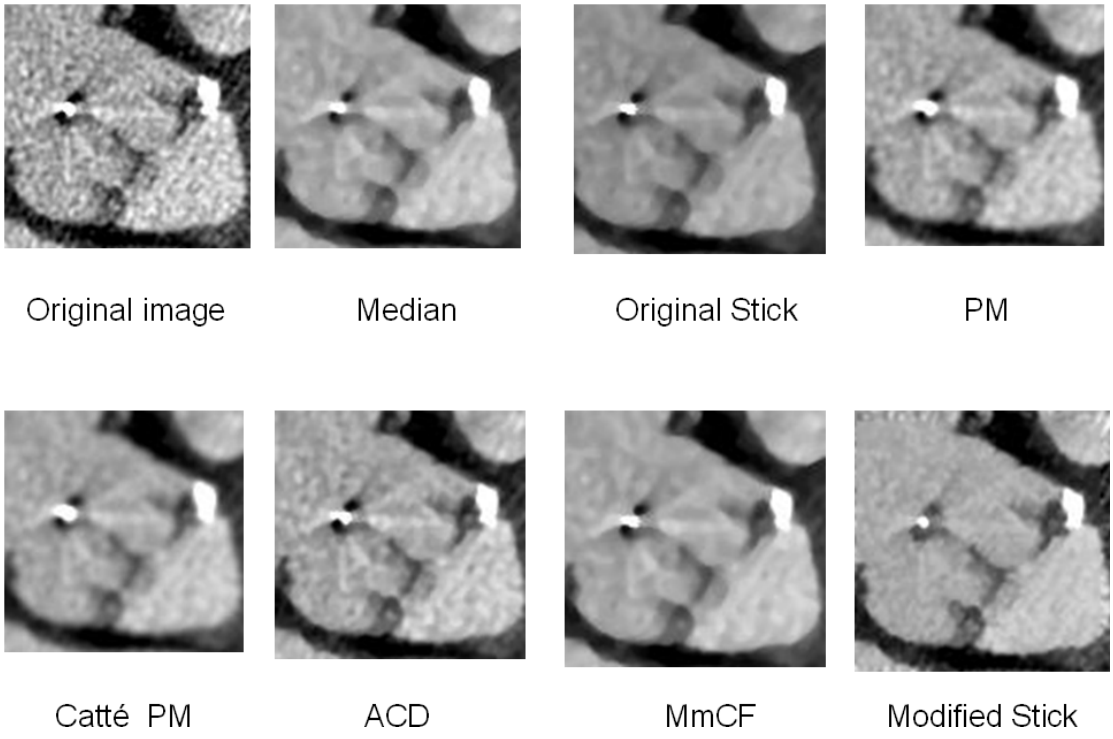

Fig. 5.7d: Filtering of case 4 - DAV (original image and results obtained with the 7 different filters).

In addition to this qualitative assessment of the results, SNR was computed on original images and resulting images (Tab. 5.3). This objective assessment shows (Fig. 5.8) that stick filtering had the best SNR for the four patients and this is consistent with the subjective appreciation.

Tab. 5.3: SNR of original images and resulting images

	Original	Median	Original Stick	PM	Catté PM	ACD	MmCF	Modified Stick
HER	12.5	27.4	27	27.2	28	27.5	27.2	28
MAG	7.5	10	14.2	11	14	14.5	13.7	15.8
BOU	5.5	6.2	7.1	6.5	7.2	7.5	7.3	13.5
DAV	7.2	14	15.9	12.6	15.8	16.5	17.2	17.5

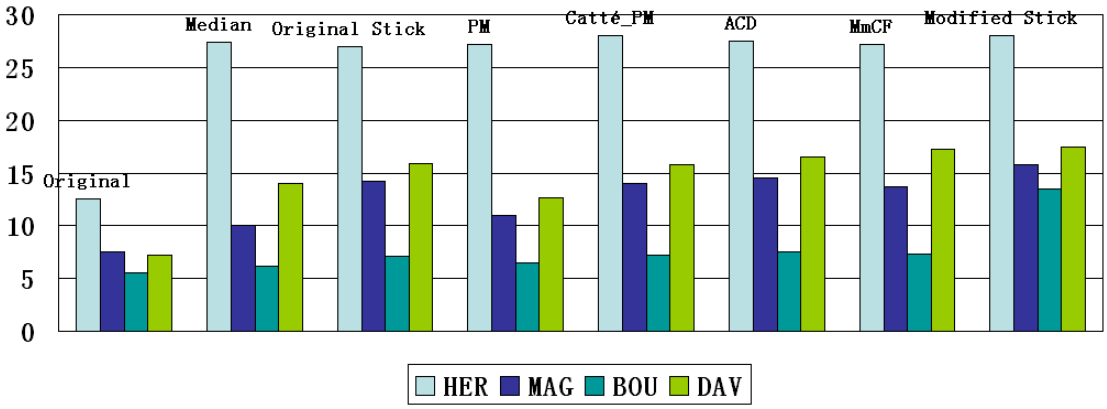

Fig. 5.8: SNR of original images and results after denoising with the different filters.

We can appreciate that in the case of high SNR images (HER) all of the filters can give good results.

The quality of filtering with Median filter depends on the size of the neighborhood. The median filter can keep object details larger than half of the considered neighborhood. Thus the best result was obtained when the size of the neighborhood was less than the thickness of leaflets (radius typically less than 3 voxels) and higher than the pattern of noise (such as in the case of DAV). This parameter is difficult to set when the thickness of leaflet is close to the thickness of noise pattern. It was the case for MAG and BOU. If a larger neighborhood is used, this may reduce the details of leaflets too much.

In the four models we considered for anisotropic diffusion filtering, the most sensitive parameter was the number of iterations. In our experiments the number of iterations was fixed according to the SNR. When SNR was not increased between two successive iterations, the filtering process was stopped. PM model have the worst performance. For instance in the case of BOU, it is difficult to appreciate the enhancement obtained on the resulting image (even after more than 20 iterations).

Catté PM model gives better results than PM model, but the size of Gaussian

convolution kernel is difficult to determine. Even when we use the smallest kernel (radius=1 voxel), details of the structures of interest are smoothed. Larger convolution kernel may cause much more smoothed result with residual noise due to the non Gaussian distribution of the original noise.

Anisotropic curvature diffusion and Min max curvature flow have similar performance, better than PM model and Catté PM model. Due to their directional filtering abilities these methods result in an undesired enhancement of metal artifacts. This drawback was also encountered with the original stick filter.

Modified stick filter show better results than others, in almost all cases. We used a stick length of 5 voxels in all cases. In the case of BOU (worst original SNR), it keeps most of the details of leaflets while reducing noise as well as ACD and MmCF. Thus, we can see that the SNR obtained with the modified stick filtering in the case of BOU is much better than the SNRs resulting from diffusion filtering. This is mainly because a “leafletness measure” was introduced in the classification process of modified stick filtering.

In addition, we can see that modified stick filter can reduce metal artifacts in the resulting images. This effect is specific to this filter.

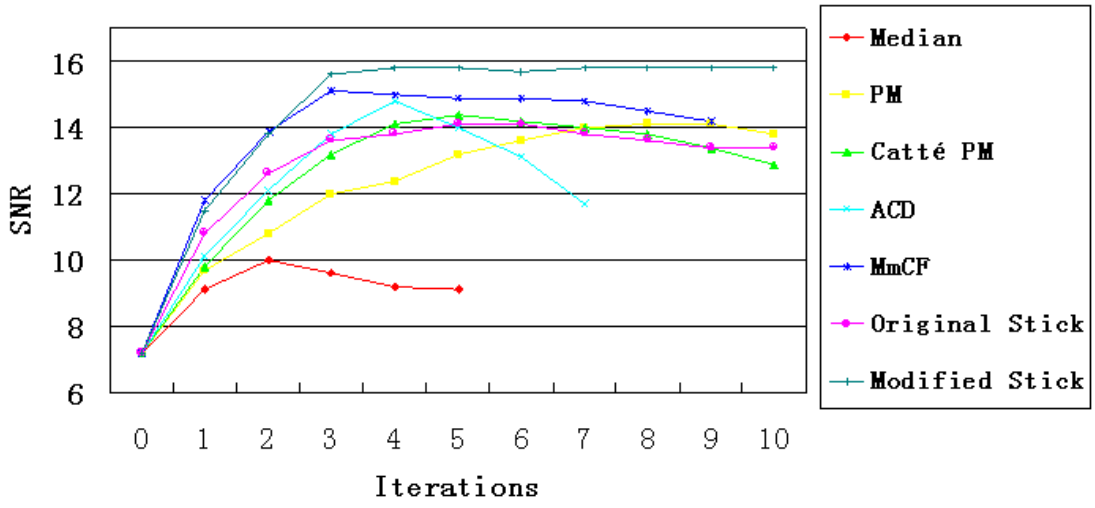

Fig. 5.9: SNR according to the number of iterations in the case n°2 - MAG.

The considered filters can be iteratively applied to the images we want to denoise. Fig. 5.9 illustrates the evolution of SNR, according to the number of iterations, during the denoising process of a low SNR image. From the curves we can see that the modified stick filter has a convergent behavior. The result converges after a few iterations (4 iterations). The same behavior was observed in the other cases (maximum of 4 iterations), with a minimum of 2 iterations in the case of HER.

The main drawback of the modified stick filter is the computation time. In the case of 5 voxels length stick, 386 sticks have to be analyzed for each voxel of the ROI. This analysis includes median value calculations which are time consuming but could be parallelized. Anisotropic diffusion filters, with same size of neighborhood, require the calculation of 728 discrete gradients or 364 curvatures, which are much less time-consuming operations.

5.4 SEGMENTATION

Following the preprocessing step, the different segmentation methods (IRG, Stick RG, and SES) were applied to in-vivo (IV) and ex-vivo (EV) images.

In the following, we present the results obtained for each patient (HER, MAG, BOU and DAV) by considering the best CT volume (optimal phase) in the cardiac cycle at the end of the diastole when the aortic valve leaflets are closed. Results obtained on slices at different locations in the CT volume are shown. Then we present the 3D visualization, with volume rendering, of the in-vivo and ex-vivo valve prosthesis description resulting from IRG, Stick RG and SES segmentations.

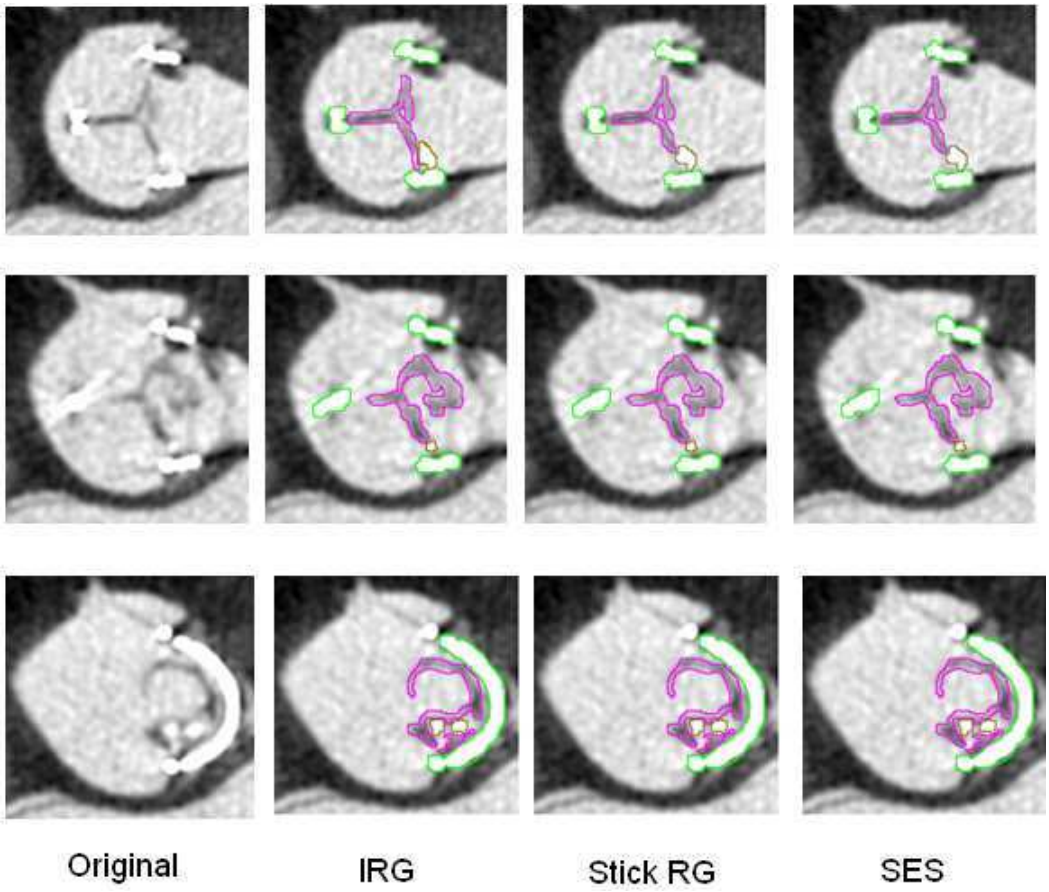

Fig. 5.10: Examples of segmented CT-Slices obtained in case 1 - HER: metallic stent, calcifications and leaflets are indicated by green, brown and purple border respectively.

The first example is reported in the case 1 of the pericardial bioprosthesis (HER). Thanks to image quality and sharp and regular boundaries of leaflet region, interactive region growing, stick region growing and stick exhaustive search give qualitatively similar and satisfactory results (Fig. 5.10).

The visualization of the segmented volume image performed by volume rendering is reported in Fig. 5.11. Morphological similarities between in-vivo and ex-vivo data, as the shape of the leaflets and the presence of a slight degeneration of these leaflets, can be easily appreciated. The leaflet prolapse resulting in no perfect coaptation appears as commissure lost (indicated in blue circle) in the segmented images.

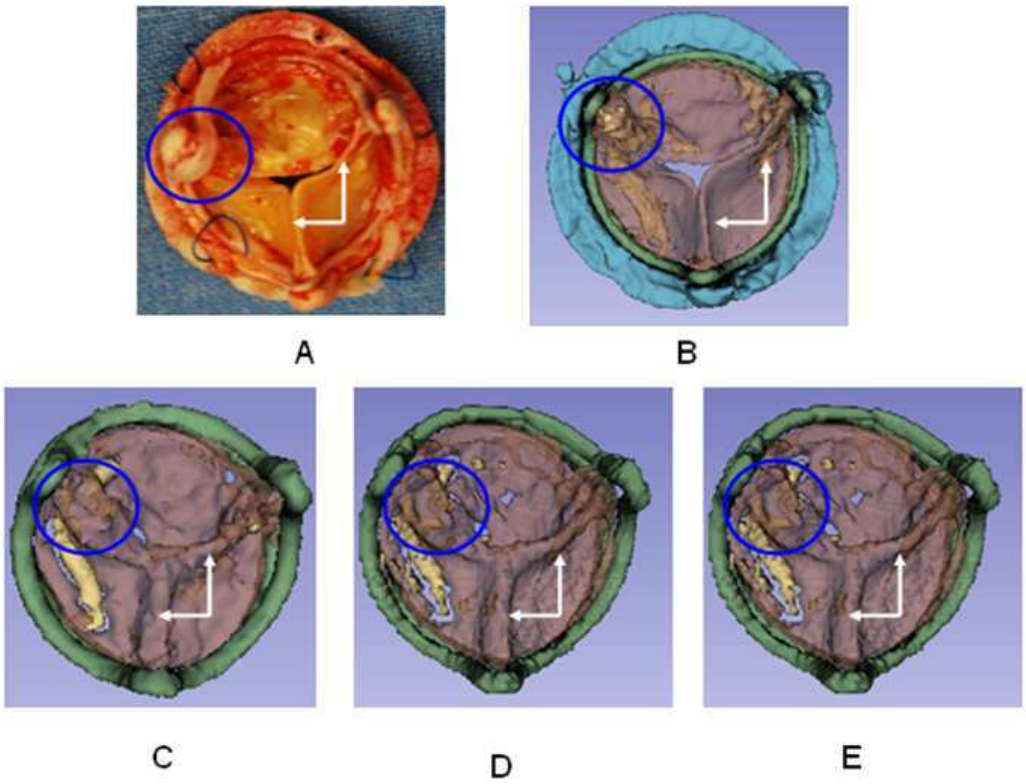

Fig. 5.11: Visualization of the segmentation results obtained in case 1 - HER. Explanted bioprosthesis (A), ex-vivo segmented bioprosthesis (B), in-vivo segmented bioprosthesis with methods IRG (C), Stick RG (D) and SES (E). The commissure lost is indicated with blue circle and good leaflets cooptation with white arrows.

The second example illustrates the results obtained in the two cases of porcine bioprothesis (case 3 - BOU and case 4 - DAV). Although the contrasts of images are low, the leaflet boundaries seem to be detected (Fig. 5.12, Fig. 5.13). Nevertheless, compared to interactive segmentation (IRG), stick based segmentations (Stick RG, SES) do not allow in these cases a complete description of the leaflets, especially in the case BOU (Fig. 5.14).

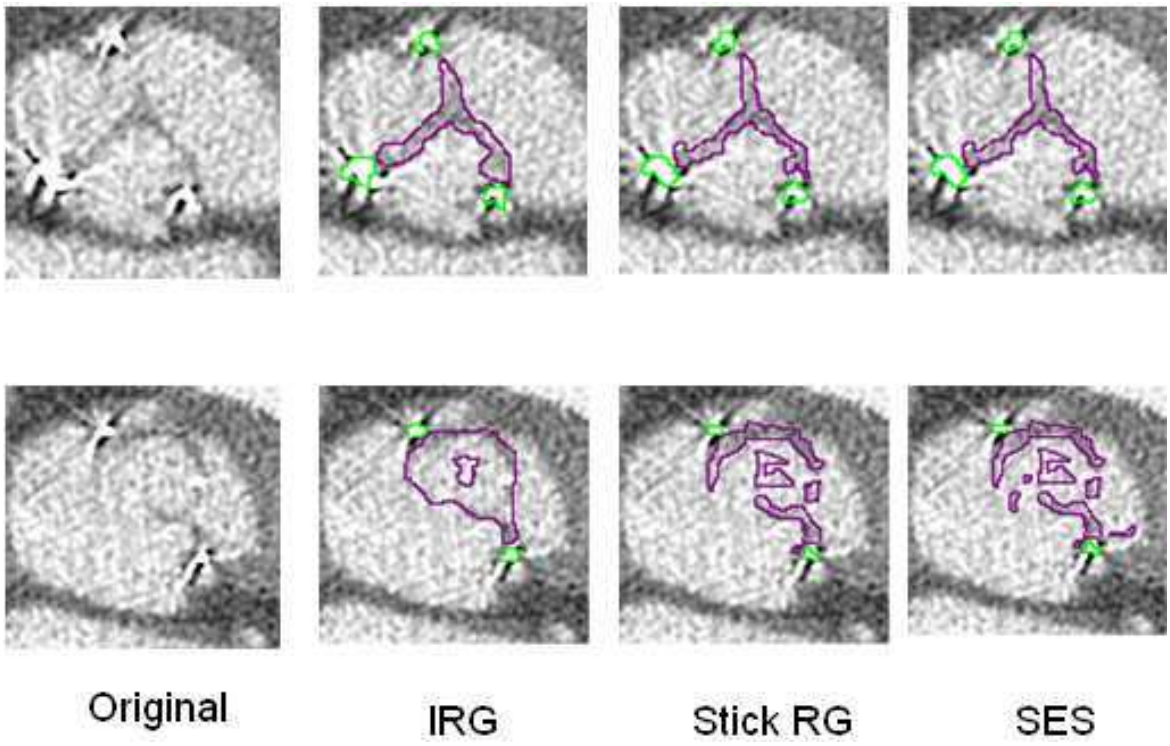

Fig. 5.12: Examples of segmented CT-Slices obtained in case 3 - BOU: metallic stent, calcifications and leaflets are indicated by green, brown and purple border respectively.

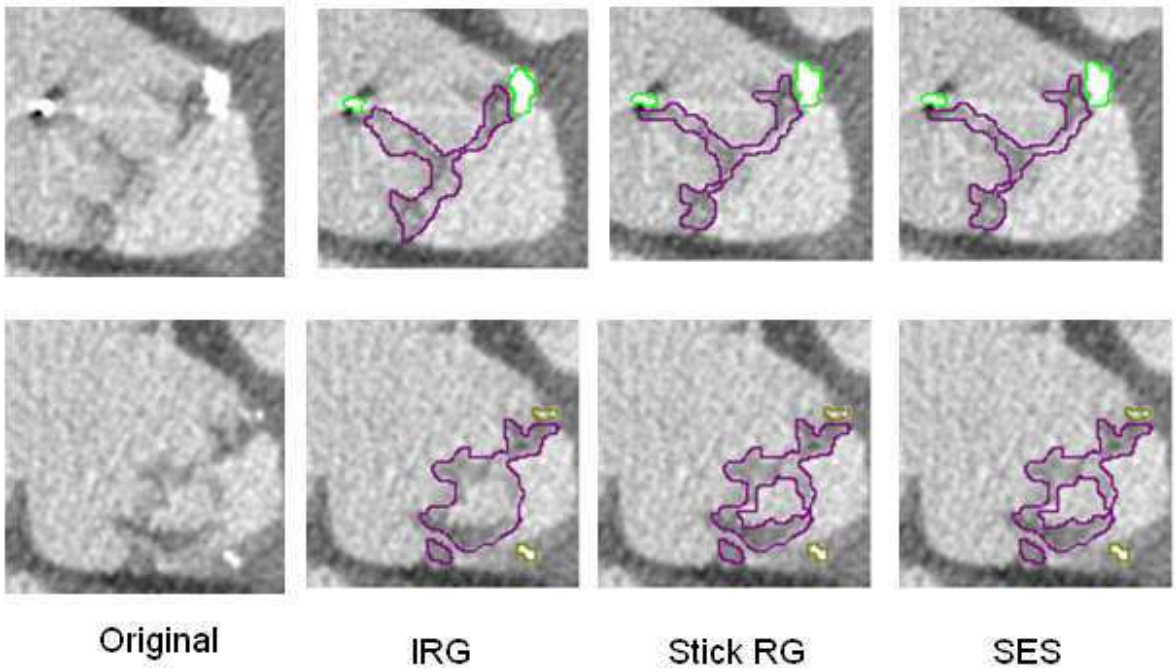

Fig. 5.13: Examples of segmented CT-Slices obtained in case 4 - DAV: metallic stent, calcifications and leaflets are indicated by green, brown and purple border respectively.

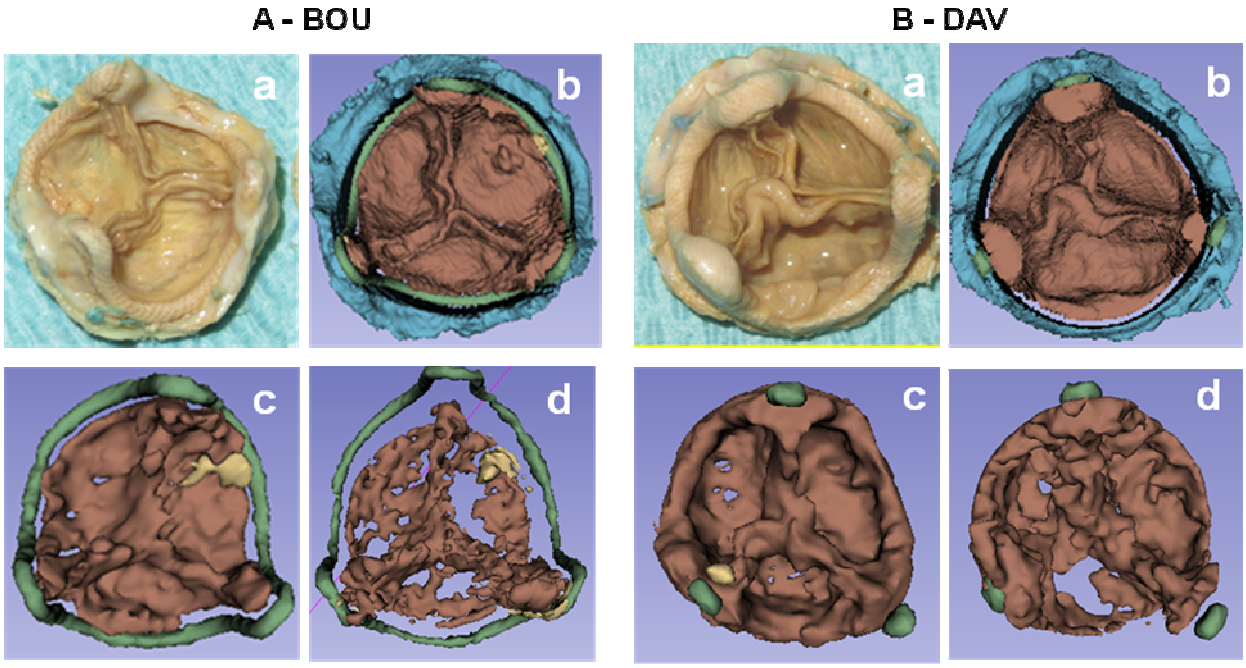

Fig. 5.14: Visualization of the segmentation results obtained in case 3 – BOU (A) and 4 – DAV (B). Explanted bioprosthesis (a), segmented ex-vivo bioprosthesis (b), segmented in-vivo bioprosthesis with methods IRG (c) and Stick RG (d).

From these results (BOU and DAV), we observed that leaflets were not fully segmented: they appear with holes or missing parts. The reason might be related to:

- Calcifications.

In some cases, calcifications are not developed too much (in HER, MAG and BOU). Their density, and therefore the value of the corresponding voxels in CT images, may have value close to that of voxels located in vascular lumen. Segmentations might classify these voxels into vascular lumen structure.

- Partial volume effect

Due to their orientation and their small thickness, compared to original CT inter-slices distance, leaflets can be affected by partial volume effect, especially for the parts located in the axial planes.

To overcome this segmentation default in some cases, the workflow could be composed of two steps:

- Automatic segmentation based on stick RG (or SES) to describe the main components of the structures.
- Interactive segmentation (based on IRG for instance) to complete the description of the missing parts of the leaflets.

Examples of results of BOU and DAV (Fig. 5.15 and Fig. 5.16) obtained with this two-steps approach are reported.

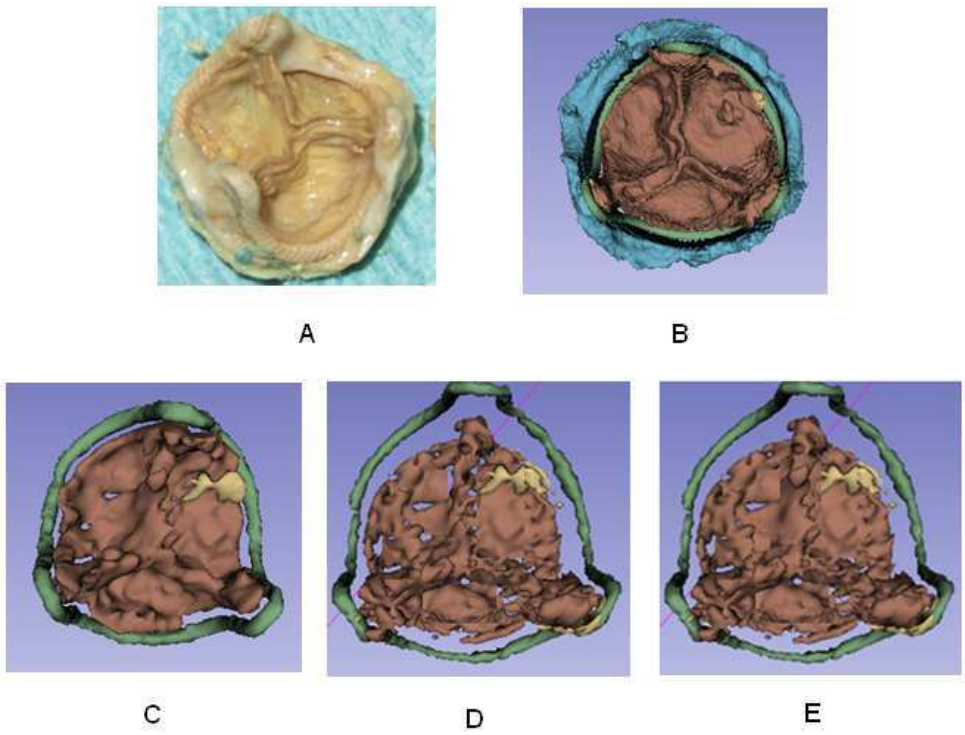

Fig. 5.15: Visualization of the segmentation correction performed in case 3 - BOU. Explanted bioprosthesis (A), ex-vivo segmented bioprosthesis (B), in-vivo segmented bioprosthesis with methods IRG (C), Stick RG with correction (D) and SES with correction (E).

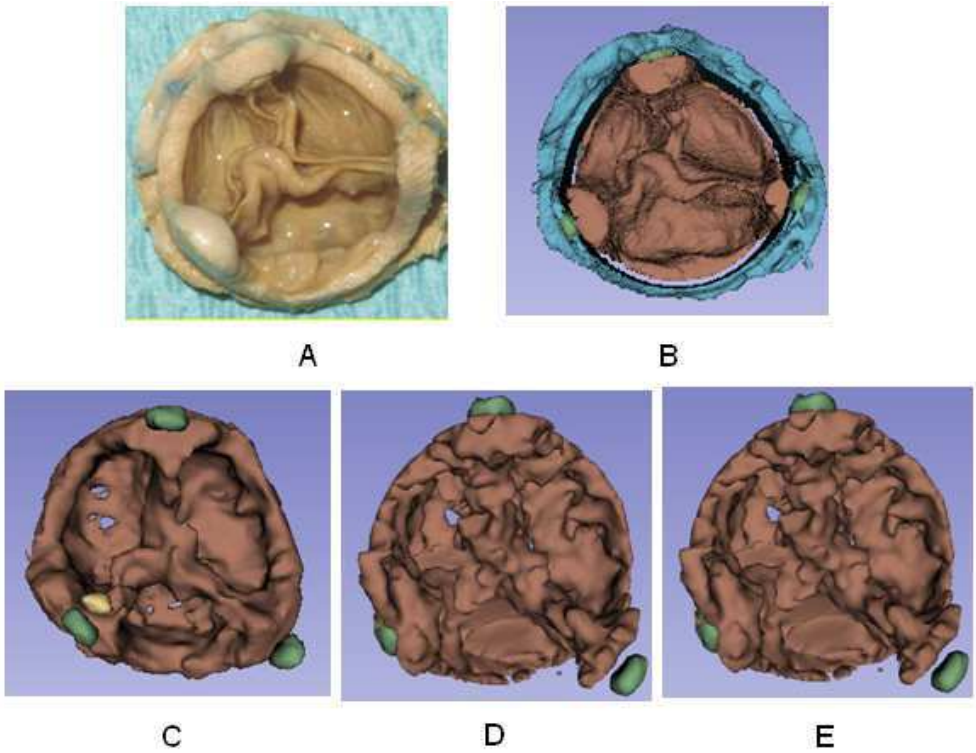

Fig 5.16: Visualization of the segmentation correction performed in case 4 - DAV. Explanted bioprosthesis (A), ex-vivo segmented bioprosthesis (B), in-vivo segmented bioprosthesis with methods IRG (C), Stick RG with correction (D) and SES with correction (E).

The last example illustrates the results obtained in case 2 (MAG) of a porcine bioprothesis. Due to the very-low-contrast structures, segmentation of leaflet was difficult. IRG gave the best but unsatisfactory results in this case. It had to be completed by a manual delineation.

The main difficulty of this kind of data sets is the high level of noise and weak (somewhere missing) boundaries. All dark voxels located in the ROI have been classified as leaflets (Fig. 5.17). In addition, there are many incomplete regions in the leaflets.

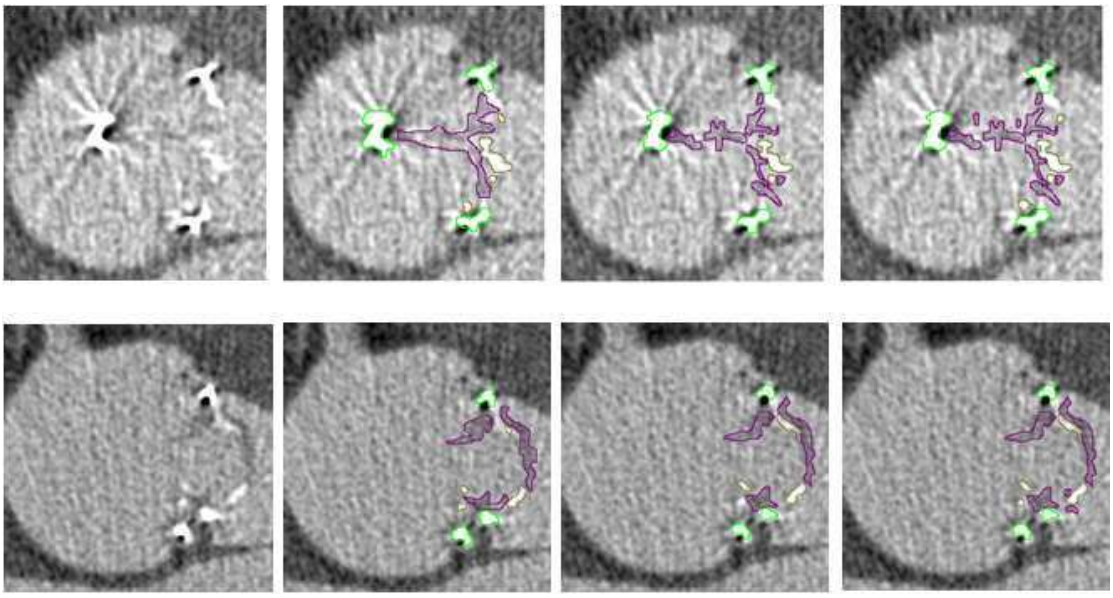

A B C D

Fig. 5.17: Examples of segmented CT-Slices obtained in case 2 - MAG. Original slices (A), results of segmentation performed by IRG (B), Stick RG (C) and SES (D). Metallic stent, calcifications and leaflets are indicated by green, brown and purple border respectively

The visualization of front and back sides of the bioprosthesis was performed by volume rendering with transparency effect (Fig. 5.18). A calcified pannus (indicated by black arrows) is characteristic in this case and responsible for valve obstruction. Leaflet tears

(indicated by green arrows) was also observed and found in reconstructions.

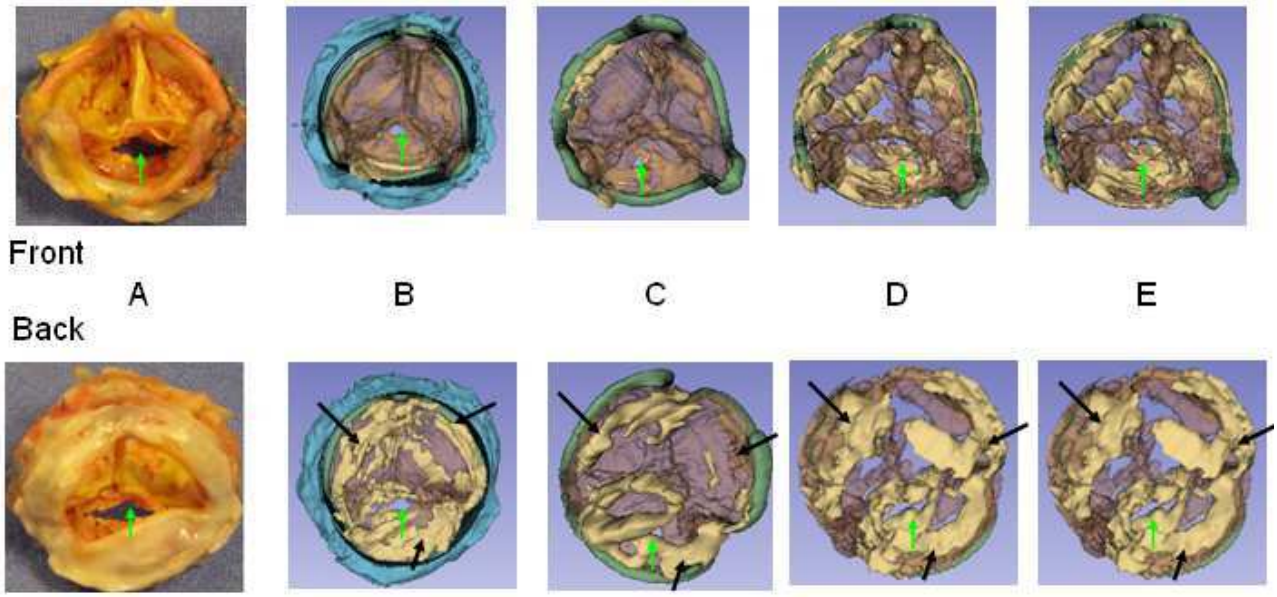

Fig 5.18: Visualization of the segmentation results obtained in case 2 - MAG (Front, i.e. view from aorta and Back, i.e. view from left ventricle). Explanted bioprosthesis (A), segmented ex-vivo bioprosthesis (B), in-vivo segmented bioprosthesis by IRG (C), Stick RG (D) and SES (E). Calcified pannus (indicated by black arrows) and leaflet tears (indicated by green arrows) are observed.

5.5 VOLUMETRIC ANALYSIS

A quantitative analysis was conducted to objectively compare the results obtained respectively by IRG, Stick RG, and SES on in-vivo (IV) and ex-vivo (EV) images. It was performed as following: the voxel volume was computed for each dataset (considering CT acquisition parameters showed in Tab. 5.2) and multiplied by the number of voxels of each bioprosthestic component resulting from the segmentation step. No correction was applied after Stick RG or SES.

The criterion used to evaluate the results was the volume of bioprothesis components. Results of this analysis are shown in Fig. 5.19 (volumes are expressed in mm^3).

This analysis seems to show that the 3 segmentation methods (IRG, Stick RG, SES), more or less automatic, allow to enhance bioprosthetic components including leaflets with similar results. In-vivo volumes are generally bigger than ex-vivo and it can be explained mostly by the moving artifacts. For sure, ex-vivo results are more reliable than in-vivo and represent the reference to assess the in-vivo results.

When we compare the results between in- vivo and ex-vivo for each method, the differences in volumes are generally less than 20%. Nevertheless, we can note that in the case HER, the in-vivo volumes are over-estimated for all the components, including stent, whereas the segmentation results were qualitatively (visually) considered better than those obtained in the other cases.

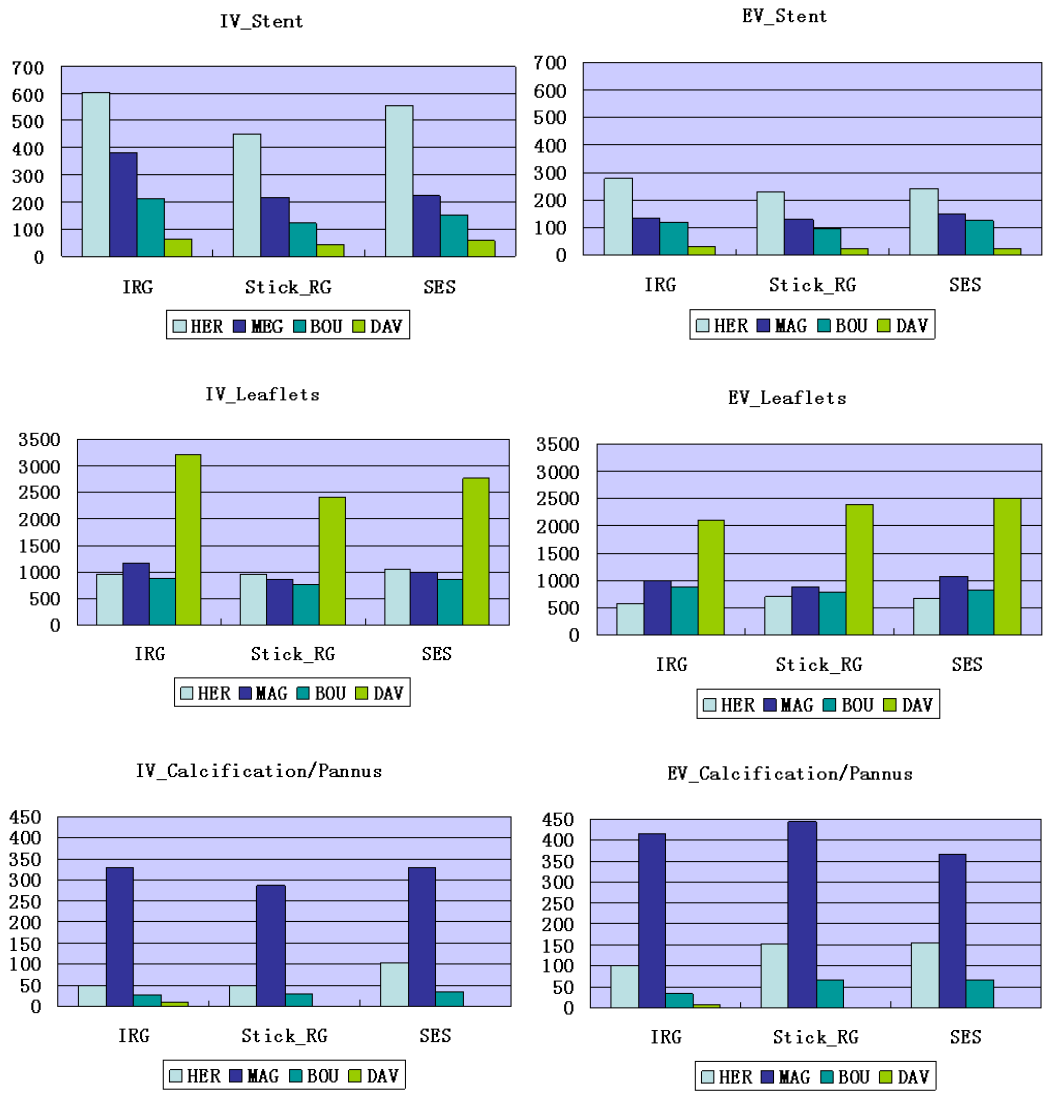

Fig 5.19: Volume analysis of bioprosthesis components

The over estimation of the volumes of the bioprosthesis components could be corrected by considering the stent as a reference structure in in-vivo data. We just suggest here a possible way to perform such a correction. Thus, a volume correction ratio could be computed as follows:

$$K = V_{RS} / V_{IV-S}$$

where V_{RS} is the volume of the real stent, which could be known from stent manufacturer data, and V_{IV-S} is the volume of the segmented stent. The application of

this correction ratio in case HER seems to reduce the differences between the in-vivo and ex-vivo volumes of leaflets (Fig. 5.20).

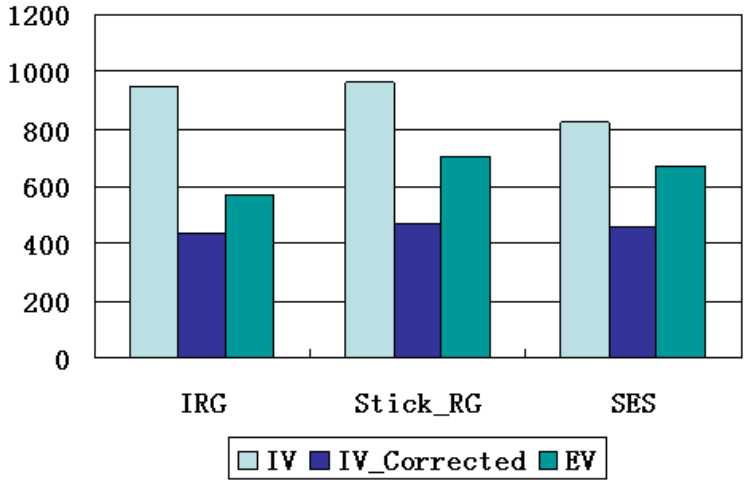

Fig 5.20: Stent based correction of leaflet volume in case HER.

5.6 DISCUSSION

An aortic bioprosthesis can have functional degradation and prosthesis dysfunction over time [5.1, 5.2]. In more recent bioprostheses, the rate of structural failure appears to be somewhat lower [5.3, 5.4] than with the first generation, but it is still occurring. The number of patients referred for reoperation because of bioprosthesis failure is quiet limited at the moment. In fact bioprostheses have been implanted for several years in elderly patients that usually don't survive to bioprostheses durability. But with the increased implantation of biological prostheses, even in younger patients, associated to the improved patients' life expectancy, we will probably assist in the next future to the advent of a new population of very elderly patients at high or prohibitive surgical risk.

Obstruction in aortic bioprosthesis may be caused by the presence of thrombus on the leaflets or stents, by fibrous or calcified pannus or by the structural deterioration of leaflets due to tears or calcification. Prosthetic thrombosis may be suspected clinically when the bioprosthesis shows acute deterioration. Fibrous pannus and structural deterioration develop slowly over time. Treatment is different: thrombosis may reverse with anticoagulation treatment. Structural deterioration and fibrous pannus are irreversible and typically require reoperation with replacement of the bioprosthesis, which can be at high risk of surgical morbidity and mortality, especially in elderly patients with associated comorbidities.

On the other hand, in the next future, high or prohibitive risk patients suffering from a structural valve deterioration of their bioprosthesis, could benefit from the new minimally

invasive techniques of transcatheter aortic valve implantation (valve-in-valve procedure) [5.5].

Understanding the precise mechanism of bioprosthesis dysfunction would thus be important to direct clinical management. Yet, it can often be difficult to identify these entities in clinical practice. Indeed, both TTE and transesophageal echocardiography with 3D application have limited usefulness for detection of the mechanism of stenotic bioprostheses, because of the acoustic shadowing from valve stents or annulus.

Multi detector CT images, thanks to their high spatial resolution, would potentially allow better visualization of the bioprosthetic valve leaflets after aortic valve replacement. Tridimensional analysis of structures, possible by MDCT images, has shown its usefulness to improve and accelerate the general understanding of vascular pathologies and allows a more realistic preoperative planning of surgery/interventional procedure.

In the same way, the tridimensional analysis of degenerated bioprostheses should improve the understanding of the failure mechanism and facilitate the medical decision about the therapeutic option.

At the moment, MDCT available softwares don’t allow 3D analysis of bioprostheses and in particular the tridimensional leaflets enhancement. So, the starting idea of this study was to assess the feasibility to 3D analyze the leaflets of degenerated bioprosthesis.

In order to validate our processing results based on pre-operative (in-vivo) images, we decided to select patients showing degeneration of their aortic bioprosthesis to echocardiography and waiting for reoperation. In this way MDCT images obtained by the explanted bioprosthesis, after redo surgery, would be used as reference.

The choice to analyze preoperative data sets and to obtain a standard reference from explanted bioprostheses to compare results has strongly limited patients inclusion.
Multiple patient related factors, mainly represented by ECG-gated CT contra-indications, participate to patients' exclusion from the study: in particular, image quality is strictly related to the heart rate during the exam. Patient clinical conditions can be responsible for high heart rate and contra-indicate medical therapy as beta-blockers to reduce it. Moreover the number of patients referred for reoperation of degenerated bioprosthesis is quite small at the moment, but it probably increase in the future, for the above mentioned reasons.

In this study we have tested three different methods for CT images segmentation of degenerated aortic bioprostheses. Considered methods, even if different in their approach, seem to be similar in terms of results. They are considered as semiautomatic segmentation methods.

The mean difference among these methods is that the Interactive Region Growing method is performed using software for image analysis (3D Slicer), relatively easy to use, but needing heavy interaction by the user (manual selection of different seed points for the different components of the bioprosthesis). On the other hand, Stick Region Growing and Stick Exhaustive Search methods need, at this time, to be performed by means of specifically designed software tools, but their interactivity is lower. The reduced interactivity level results in some differences in terms of voxels volumes. It seems difficult to replace the user ability to recognize bioprosthesis different structures in CT transverse sections (IRG) by the automatic criteria based on CT density (Stick RG and SES).

Quantitative analysis shows these differences among the methods, but we can't consider them significant because of the inability to perform a statistical analysis on few data sets. Moreover, we don't know at the moment if these small differences (generally less than 20%) could have a real interest for practical application. The aim of this study was first to assess the feasibility to reconstruct leaflet morphology by preoperative CT images segmentation.

Looking at CT preoperative images the problem was mainly represented by noise and artifacts. For this reason the pre-processing step to improve image quality represents a key point in the analysis of in-vivo data sets. Different filters have been tested and proposed to reach the best leaflets enhancement. Among these, the modified Stick filter has shown the best results, confirmed by quantitative SNR analysis. This is certainly thanks to its better applicability to thin structures such as leaflets. Stick filter is performed using MatLab software and it can take time to be realized. In order to reduce its computing time, the selection of a region of interest, that takes into account only the bioprosthesis stent region including the leaflets, seems to represent a good and easy strategy.

Some comments have to be done concerning segmentations results. Among the analyzed datasets the best results have been obtained in the case of the pericardial bioprosthesis (Case #1 – HER). In this specific case the reason can be partially attributed to the thickness of the valve tissue. Pericardial leaflets are largely thicker than porcine with consequent better detection by CT. Results of all segmentation methods were

satisfactory in this case and less interactive/more automatic methods based on stick segmentation should be considered and preferred for their efficacy.

The porcine bioprostheses (Case #2,#3,#4 – MAG, BOU, DAV) showed in general worst results. Porcine leaflets are quit thin and their thickness could be not the same along the leaflets because of their natural origin. The incomplete detection by CT results in leaflets defects in 3D reconstructions. In these cases interactive method allows manual adjustments to complete undetected leaflets and should be preferred.

Looking at quantitative analysis, there are different factors that could explain the volumes differences observed between in-vivo and ex-vivo reconstructions. Firstly, the image resolution is not the same. In-vivo acquisition protocol is represented by the standard protocol used for ECG gated coronary CT and specific acquisition for bioprosthesis analysis doesn't exist at the moment. Concerning the ex-vivo images we chose a high resolution acquisition protocol (temporal bone) to be as close as possible to reality and to use these images as reference. Other than image resolution, we can consider the presence of the heart motion and of blood superposition as important factor for volumes differences. To deal with this problem we propose a correction factor that could represent an interesting way to reduce the volume differences but need to be validate in larger series.

Computing of leaflets volumes can also be altered by the non-metallic part of bioprosthesis stent. Only the metallic stent can be used as spatial limitation for the leaflets because the non metallic part has the same density of the leaflets. For this reason leaflet volumes are higher than normal in the only case of bioprosthesis with incomplete

metallic stent (Case #4 DAV). This problem can be translated to stentless bioprostheses analysis and need to be considered to avoid confusion in results.

Another point is that, in all studied cases, we observed in-vivo underestimation of leaflets degeneration. It should be said that, in these particular studied cases, leaflets are not severely calcified and most part of degeneration consists in leaflets thickening. These mild alterations of the leaflets don't appear strongly dense such as calcifications and can be difficult to detect in in-vivo images. This results in a consequent underestimation of degeneracy compared to ex-vivo images, in which smaller differences in density can be easily appreciated.

This study had a number of limitations. Firstly the limited studied cases and their heterogeneity don't allow full validation of results. Moreover data sets were obtained with two different CT systems: the new one dispose of a specific process to reduce radiation dose maintaining the same diagnostic accuracy. Quantitative analysis is conducted on in-vivo and ex-vivo data of bioprostheses in different experimental conditions which can explain the volumetric deviations. Finally, the correction factor proposed to adjust leaflets volume differences is based on stent volumes coming from ex-vivo images treated with the same methods and not from manufacturers.

Our study suggests that preoperative 3D analysis of degenerated bioprosthesis is feasible but CT images could need additional processing. Improved images can be segmented and resulting reconstructions can help to directly visualize leaflets morphology and could play a role in clarifying the mechanism of bioprosthesis dysfunction. Furthermore, we demonstrated the ability of these methods to identify

bioprosthesis leaflet thickening, calcifications as well as presence of pannus under bioprosthetic leaflets.

5.7 REFERENCES

[5.1] Bloomfi eld P , Wheatley DJ , Prescott RJ , Miller HC . Twelve-year comparison of a Bjork-Shiley mechanical heart valve with porcine bioprostheses . N Engl J Med 1991 ; 324 : 573 – 579 .

[5.2] Hammermeister KE, Sethi GK, Henderson WG, Oprian C, Kim T, Rahimtoola S. A comparison of outcomes in men 11 years after heart-valve replacement with a mechanical valve or bioprosthesis. Veterans Affairs Cooperative Study on Valvular Heart Disease . N Engl J Med 1993 ; 328 : 1289 – 1296 .

[5.3] Puvimanasinghe JP , Steyerberg EW , Takkenberg JJ , et al . Prognosis after aortic valve replacement with a bioprosthesis: predictions based on meta-analysis and microsimulation. Circulation 2001; 103 : 1535 – 1541.

[5.4] Ruggieri VG, Flecher E, Anselmi A, et al. Long-Term Results of the Carpentier-Edwards Supraannular Aortic Valve Prosthesis. Ann Thorac Surg. 2012 Jul 7.

[5.5] Piazza N, Bleiziffer S, Brockmann G, et al. D. Transcatheter aortic valve implantation for failing surgical aortic bioprosthetic valve: from concept to clinical application and evaluation (part 2). JACC Cardiovasc Interv. 2011 Jul;4(7):733-42.

VI – CONCLUSION AND PERSPECTIVES

Echocardiography remains the gold standard for functional analysis of bioprosthesis failure. In the last years an increasing number of groups are looking with particular interest at CT images for anatomo-morphological analysis of the aortic valve.

In this study we proposed a new approach for the morphological analysis of degenerated aortic valve bioprostheses by CT scan images segmentation. Our preliminary results suggest the feasibility to enhance aortic bioprosthesis leaflets applying the proposed processing methods for noise reduction and segmentation to preoperative CT images. Because today such visualization of bioprosthesis leaflet morphology is intricate to impossible with other imaging techniques, we believe that in the next future high resolution CT images segmentation may play an important role to improve the understanding around the mechanism of dysfunction in patients with a degenerated aortic valve bioprosthesis.

Additional studies are necessary to improve and validate these results. Subject to further validation of the proposed image processing methods, presumably accompanied by an adaptation of the acquisition protocols, the analysis of the degeneration in bioprostheses could be considered in larger series.

It is also important, in our opinion, to characterize the mechanical properties of the leaflets either normal or degenerated for the different types of bioprostheses. This will allow to create a reference data set. In this way, 3D reconstructions of bioprostheses could represent in next future an important tool to improve the planning of the valve-in-valve procedure or could be used to preoperatively simulate this procedure (Fig. 6.1).

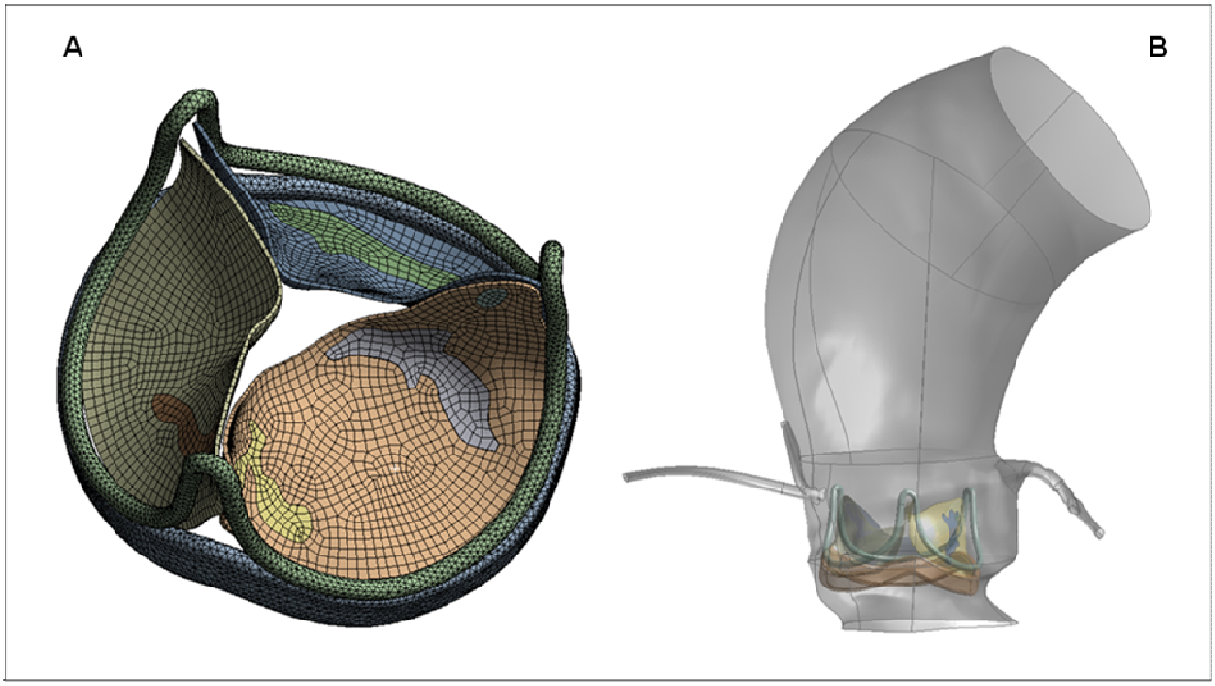

Fig. 6.1: Mesh describing valve geometry and tissue properties (A), as well as surrounding structures (B), in case 1 - HER.

In order to anticipate the impact of some actions (such as balloon dilation, prosthesis deployment) during a valve-in-valve procedure, the proposed approach for the analysis of the bioprosthetic valve components could be used to provide patient-specific input data to a numerical simulation process. The morphology of the bioprosthesis could be expressed through a geometrical mesh where the node attribute, obtained from pre-operative CT analysis, is the class of tissue (calcification, healthy tissue, ...) determining the material mechanical properties to consider in the simulation, as illustrated in Fig. 6.1. This simulation could then provide a way to predict the outcome of the gesture and could be useful for case selection and procedure planning.

Appendix 1 - Figures legends

Appendix 2 - Tables legends

Appendix 3 - Publications and Grants

JOURNAL ARTICLES

Ruggieri VG, Wang Q, Esnault S, Luo L, Leguerrier A, Verhoye JPh, Haigron P. **Analysis of degenerated aortic valve bioprosthesis by segmentation of preoperative CT images.**
IRBM (Recherche et Ingénierie Biomédicale) 2012. Article in press.

Ruggieri VG, Anselmi A, Wang Q, Esnault S, HaigronP, Verhoye JPh.
CT scan images processing to detect the real mechanism of bioprosthesis failure. Implication for valve-in-valve implantation.
J Heart Valve Dis 2012. Article in press.

Ruggieri VG, Haigron P, Wang Q, Esnault S, Madeleine R, Heautot JF, Leguerrier A, Verhoye JPh.
CT-scan images preprocessing and segmentation to improve bioprosthesis leaflets morphological analysis.
Medical Hypotheses 2012 – Under revision

PROCEEDINGS

V.G. Ruggieri, Q. Wang, R. Madeleine, S. Esnault, P. Haigron, J-Ph. Verhoye
CT scan images processing by semi-automatic segmentation to analyse aortic bioprostheses
Proceedings of the 47th Congress of the European Society for Surgical Research. June 2012 – Lille (France).

Q. Wang, V.G. Ruggieri, J-Ph. Verhoye, A. Lucas, B. Miguel, H. Shu, L. Luo, P. Haigron
A Method for Narrow Vascular Structure Segmentation in CT Data
Proceedings of RITS - Recherche en Imagerie et Technologie pour la Santé – April 2011 - Rennes (France).

JOURNAL PUBLISHED ABSTRACTS

V.G. Ruggieri, A. Anselmi, Q. Wang, R. Madeleine, P. Haigron, J-Ph. Verhoye.
Improved pre-procedural assessment of failing bioprostheses by CT scan. Implications for valve-in-valve procedure.
61st E.S.C.V.S. International Congress, Dubrovnik, Croatia – Avril, 2012.
Abstract n. 548.
J Cardiovasc Surg 2012, 53 (Suppl I to N.2): 35.

MEETINGS POSTERS

Analyses tomodensitométriques pré-opératoires de bioprothèses aortiques défaillantes; intérêt pour les procédures « valve dans valve ».
V.G. Ruggieri, Q. Wang, R. Madeleine, S. Rouze, P. Haigron, J-Ph. Verhoye.
65ème Congrès de la Société Francaise de Chirurgie Thoracique et Cardiovasculaire (Nice – Mai 2012).

Morphological assessment of failing aortic bioprostheses by CT scan images processing.
V.G. Ruggieri, A. Anselmi, Q. Wang, S. Esnault, P. Haigron, J.P. Verhoye
26th National Congress of Italian Society of Cardiac Surgery, 10-13 November, 2012 Rome, Italy

MEETINGS COMMUNICATIONS

V.G. Ruggieri, Q.Wang, R. Madeleine, S. Esneault, P. Haigron, J-Ph. Verhoye
CT-scan assessment of failing bioprostheses. Implications for valve-in-valve implantation.
6th Congress of Asian Society of Cardiovascular Imaging (ASCI 2012) June 2012 - Bangkok, Thailand.

Ruggieri VG., J-Ph. Verhoye
Interactive segmentation of degenerated aortic bioprosthesis.
BIT's 3rd Annual International Congress of Cardiologiy. December 2011. Beijing, China.

Ruggieri VG, J-Ph. Verhoye
Interactive segmentation of degenerated aortic bioprosthesis.
OMICS San Francisco July 2011. USA.

ACADEMIC AWARDS

Nomination for Young Surgical Talent Award – French National Academy of Surgery

2012 – Best Young Researcher Award - French Society of Thoracic and Cardiovascular Surgery **(sponsored by St. Jude Medical Society)**

FINANCIAL GRANTS

2009 and 2011 - **ADETEC Society** (Association chirurgicale pour le développement et l'amélioration des techniques de dépistage et de traitement des maladies cardio-vasculaires).

Analysis of degenerated aortic valve bioprosthesis by segmentation of preoperative CT images

Analyse de bioprothèse valvulaire aortique dégénérée par segmentation d'images TDM préopératoires

V. G. Ruggieri[1,2,3,*], Q. Wang[1,2], S. Esneault[4], R. Madeleine[4], L. Luo[5,6], A. Leguerrier[3], J. P. Verhoye[1,2,3], P. Haigron[1,2]

[1]*LTSI, université de Rennes 1, campus de Beaulieu, bâtiment 22, 35000 Rennes, France*
[2]*Inserm U1099, campus de Beaulieu, bâtiment 22, 35000 Rennes, France*
[3]*Department of Thoracic and Cardiovascular Surgery, University Hospital Pontchaillou, 35000 Rennes, France*
[4]*Therenva, CIC-IT, Rennes, France*
[5]*LIST, Southeast University, Nanjing, China*
[6]*CRIBs, Centre de Recherche en Information Biomedicale sino-francais, Rennes / Nanjing, France / China.*

Abstract
In the next future, transcatheter aortic valve implantation could represent a minimally invasive option in case of bioprosthesis failure for patients at high surgical risk. CT based preoperative planning of this procedure could be useful to optimize valve-in-valve implantation. In this context, bioprosthesis 3D analysis seems to be necessary, particularly for leaflets.
The goal of this study was to propose different methods to segment and characterize a degenerated bioprosthesis using standard preoperative CT scan images in order to map structural injury of bioprosthesis and, ultimately, to plan the best positioning for valve-in-valve implantation. We report our preliminary results on segmentation of a degenerated bioprosthesis in aortic position. Three different methods have been tested and all allowed obtaining segmentation of the different bioprosthesis components. Results were compared by means of quantitative criteria. Explanted bioprosthesis CT images were used as reference. Semi-automatic segmentation seems to provide an interesting approach for the morphological characterization of degenerated bioprosthesis.

Résumé
Dans le futur prochain, l'implantation percutanée de prothèse valvulaire aortique pourrait représenter une option mini-invasive dans le cadre de la dégénérescence de bioprothèse chez les sujets à haut risque chirurgical. La planification préopératoire basée sur les images scanner pourrait être utile pour optimiser l'implantation de la valve dans la valve. Dans ce contexte, une analyse tridimensionnelle de la bioprothèse dégénérée paraît nécessaire, surtout en ce qui concerne les feuillets prothétiques.
Le but de l'étude est de proposer différentes méthodes pour segmenter et caractériser une bioprothèse dégénérée en utilisant les images scanner préopératoires à fin de mapper l'endommagement structurel de la bioprothèse et, en dernière hypothèse (dans une optique future), de planifier le positionnement adapté de la valve percutanée dans la bioprothèse. Nous reportons les résultats préliminaires de la segmentation de bioprothèse valvulaire aortique. Trois différentes méthodes ont été testées et toutes ont permis d'obtenir une segmentation des différentes composantes de la bioprothèse. Les résultats ont été comparés par des critères quantitatifs. Les images scanner des bioprothèses explantées lors du ré-intervention ont servi de référence. La segmentation semi-automatique représente une approche intéressante pour la caractérisation morphologique des bioprothèses dégénérées.

Keywords: Aortic valve bioprosthesis analysis, valve-in-valve, stick based segmentation, aortic valve implantation
Mots-clés: Analyse de bioprothèse de valve aortique, valve dans valve, segmentation basée "stick", implantation de valve aortique.

*Auteur correspondent
Adresse e-mail : vito-giovanni.ruggieri@chu-rennes.fr (V.G. Ruggieri)

I. Introduction

Aortic valve stenosis remains the most common valvular disease [1,2]. The gold standard for treatment is surgical aortic valve replacement [3]. The combined effects of an aging population and the prevalence of aortic stenosis in this cohort have led to increasing numbers of elderly patients being referred for valvular surgery. The valve of choice in these patients is usually a bioprosthetic device, to avoid the need for anticoagulation with its associated complications [4]. Moreover, with the good long term results in durability of the new generation devices, bioprosthesis implantation is going to increase also in younger patients in the next years.

As a result, there is an increasing prevalence of failing bioprosthetic aortic valve replacements. Concurrently, the spectrum of comorbidities in these patients grows more complex, and therefore the risks of re-do surgery increase. Absolute surgical risk for re-do aortic valve operations might be raised by up to 15% compared with initial implants [5,6].

Trans-catheter aortic valve implantation (TAVI) has entered the mainstream as a viable treatment option for patients with symptomatic, severe aortic stenosis, who are at prohibitively high surgical risk. The initial success in 2002 [7] has been followed by a surge of interest, strengthened by encouraging medium-term results with both the self-expanding CoreValve (Medtronic, Luxembourg) [8,9] and balloon-expandable Edwards Sapien (Edwards Lifesciences, Irvine, California) systems [10,11].

Although not initially designed for this purpose, TAVI is also an option for patients with a degenerative aortic valve bioprosthesis who would be at high surgical risk from repeat thoracotomy. The feasability of implanting a trans-catheter valve into a surgical bioprosthesis was first demonstrated in a pig model in 2007 [12]. The investigators used the Cribier-Edwards system to transapically implant 23-mm devices into 5 Carpentier Edwards porcine aortic valve prostheses to good effect. A case report of successful treatment of a severely regurgitant aortic valve bioprosthesis with the CoreValve (Medtronic) system has also been described—with retention of good function and no complications at 1-year follow-up [13].

Until now, some reports about valve-in-valve implantation are available [14], but the implanting technique remains empiric and modified for each different case and prosthesis. In next future, preoperative patient-specific simulation of endovascular procedure could be useful to optimize valve-in-valve implantation in order to predict intra-operative fitting and to reach the best positioning of the new prosthesis. In order to realize a preoperative planning of valve-in-valve implantation, 3D analysis and characterization of the structures of interest are necessary.

Nowadays, automatic processing segmentation of preoperative vascular CT images is feasible and provides relatively accurate results. This is no more the case for valvular prosthesis, specifically for prosthetic leaflets and their degeneration. To our knowledge there are some methods reported in the literature dealing with coronary ostia and valve leaflets detection [15, 16]. None of them deals with the issue of CT analysis of failing aortic bioprosthesis. The difficulties come from the combination of different factors: inhomogeneities of contrast product distribution used for the acquisition of CT images of cardiovascular structures, low contrast between the structures of interest (leaflets, calcifications, contrast) and image resolution compared with structure thickness (leaflets).

The goal of this study is to propose a new segmentation-based approach to characterize a degenerated bioprosthesis. We show and discuss our preliminary results. Results of the preoperative segmentation could, ultimately, be useful to discuss about the valve-in-valve procedure indication and to plan the best positioning for trans-catheter implantation.

II. Analysis of Degenerated Valve

A. Degenerated valve leaflets analysis

Multi Slice Computed Tomography (MSCT) shows a high spatial resolution and can also be used to acquire spatio-temporal data during the cardiac cycle. In this work we are interested in using MSCT data to assess pathological features of cardiovascular structures such as aortic valve leaflets. Figure 1 illustrates original noisy MSCT images showing stent with high density and possible artifacts (A), low contrasted leaflets (B), calcifications on leaflets (C) and pannus under stent (D). The range of grey level in vessel lumen was typically about [1300 HU, 1550 HU], and in leaflets about [1150 HU, 1420 HU].

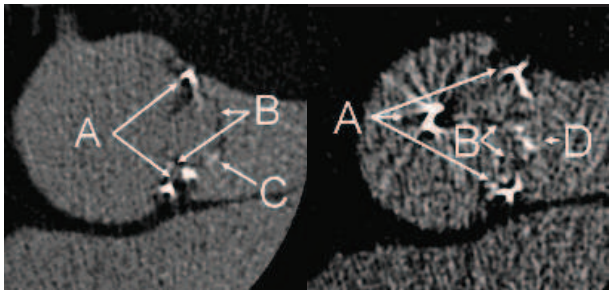

Figure1: Two noisy MSCT slices of aortic valve prosthesis showing stent (A), leaflets (B), calcification (C) and pannus (D).

The overall framework (Fig.2) proposed to analyze thin cardiovascular structures as valve leaflets from MSCT data, is composed of : (i) the definition of a Region of Interest (ROI) depending on the type of bioprosthesis stent implanted in the patient, (ii) a preprocessing step to denoise the original image, (iii) the segmentation of valve bioprosthesis components mainly based on a region growing process and (iv) the visualization process. Two approaches were considered for the preprocessing and three for the segmentation. In the preprocessing step anisotropic Diffusion curvature filter and Stick filter were implemented. In the segmentation process, the first approach was based on a classical isotropic region growing approach, the second on a directional (stick) region growing process and the third on a stick exhaustive search. In order to evaluate the performance of the segmentation of "in-vivo" images (preoperative images), the proposed

approach was also applied to the "ex-vivo" images (explanted bioprosthesis) after patient reoperation.

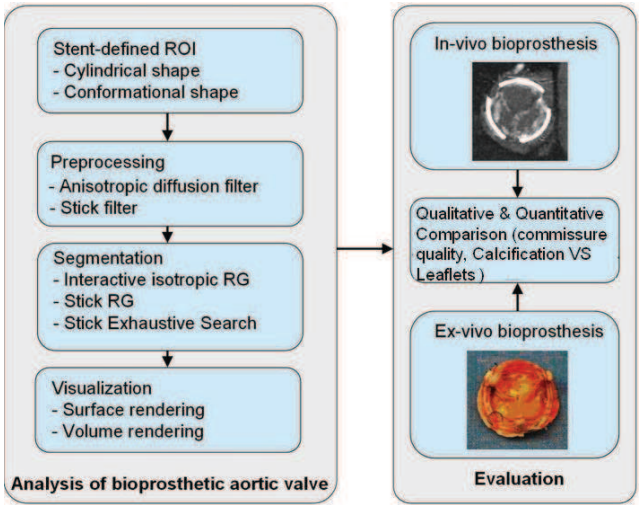

Figure 2: Framework of bioprosthetic aortic valve analysis from MSCT data.

B. *Stent defined ROI*

In order to deal with the difficulties of segmentation of the CT images of the bioprosthesis mentioned above (metal artifacts, thickness of leaflets compared with image resolution, density of valve components compared to stent) we considered a region of interest (ROI) defined by the stent. This ROI can have different shapes according to the type of stent implanted in the patient. We considered two kinds of shape for the ROI: a cylindrical shape preferentially for incomplete metallic stents and a conformational shape for complete metallic stents (Fig. 3).

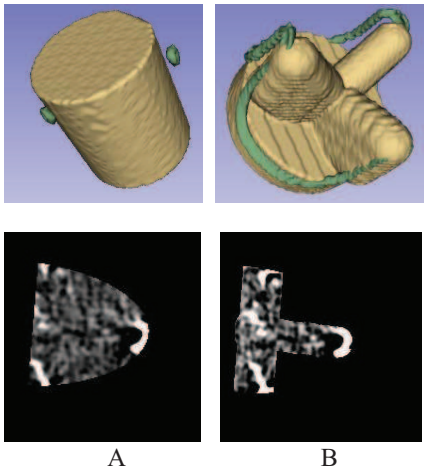

Figure 3: Shapes (A cylindrical, and B conformational) of stent defined ROI and illustration of the corresponding CT observations (within one of the original CT slices).

C. *Preprocessing*

In order to reduce the noise in CT images a preprocessing step is implemented. The preprocessing goal is to increase the signal to noise ratio (SNR) as well as to increase the contrast of the structures of interest, especially the valve leaflets. We considered methods based on Diffusion filters (curvature and anisotropic Diffusion filter) as well as an adaptation of Stick filters to reduce noise and keep details in thin structures. To select the most appropriate approach before the segmentation step, we considered the SNR as the performance criterion. To compute the SNR we used the definition given in [19]:

$$SNR = 10 * \log_{10}\left(\frac{Max(Var_i)}{Min(Var_i)}\right)\Big|_{i\in ROI} \quad , \qquad (1)$$

where Var_i is the the local variance in the neighborhood of leaflets and vascular lumen voxels located in the ROI. Voxels located at the boundary between leaflets and vascular lumen are used to obtain the maximum variance whereas voxels located in the vascular lumen are used to obtain minimum variance. Due to their high value, voxels representing stent, calcification and pannus are not considered in the computation of SNR.

1 - Anisotropic Diffusion filter

The Diffusion filters are non-linear filters based on partial differential equations. They have been proposed for noise reduction and segmentation, particularly for vascular images.

In classical Perona-Malik (**PM**) model [20], the values of resulting voxels I_p^{t+1} are calculated as:

$$I_p^{t+1} = I_p^t + \frac{\lambda}{|\eta_p|}\sum_{q\in\eta_p} c(\nabla I_{p,q}^t)\nabla I_{p,q}^t \quad , \qquad (2)$$

where η_p is the neighborhood of the current voxel and $|\eta_p|$ is the number of voxels in η_p. I_p^t is the current value of the voxel. $\nabla I_{p,q}^t$ is the discrete gradient along the q[th] direction (defined by the current voxel and a voxel of the neighborhood). *c(x)* is the classifier between edge and noise. *c(x)* can take different expressions such as:

$$c(x) = \frac{1}{1+(x/k)^2} \text{ or } c(x) = \exp(-(x/k)^2), \qquad (3)$$

λ and *k* are two parameters to control Diffusion intensity.

$k = \frac{1}{0.6745} median(|\nabla I_i| - median(\nabla I_i))|_{I\in ROI}$ represents the absolute median value [21] of discrete gradient of all voxels inside ROI.

Classical Anisotropic Diffusion operators such as PM model can enhance edge while denoising the image. Nevertheless, they may enhance both edge and noise in low SNR conditions. Anisotropic Curvature Diffusion, which is based on a Modified Curvature Diffusion Equation [22-24], has been introduced to overcome this problem and to be less sensitive to noise.

Discrete Gradient $\nabla I_{p,q}^t$ used in PM model was replaced by Gaussian Curvature of the voxel in the Anisotropic Curvature Diffusion:

$$I_p^{t+1} = I_p^t - \frac{\lambda}{N}\sum_{q\in\eta_p} c(Curv(P_{p,q}^t))Curv(P_{p,q}^t), \qquad (4)$$

where $P^t_{p,q}$ is the plane defined by the current voxel and a direction given by a voxel of the neighborhood η_p. $Curv(P^t_{p,q})$ is the Gaussian Curvature at the voxel. $N = 3L^2 - 6L + 4$, L is the length of side of cubic neighborhood.

In the proposed CT data preprocessing approach, we chose $|\eta_p| = 26$ and N=13 (3*3*3 cubic neighborhood). Higher values of η_p may smooth edge and increase computational complexity too much. $c(x) = \frac{1}{1+(x/k)^2}$ was selected thanks to its simple computational complexity. Values of λ and k were set at 1 for a low level of noise (high SNR). In the case of images showing a high level of noise (SNR<=8), λ were set at 0.5.

2 – Stick filter

Stick filter is also a non-linear filter. It was originally introduced to deal with strips-like noise in US images [17-18]. With Stick filtering approach, the neighborhood of the considered voxel is divided into a set of asymmetric sticks to perform a non-linear filtering of the image (Fig. 4). Because of its asymmetric stick, the filter could get better performance in terms of keeping details of thin structure, as valve leaflets, while denoising the image.

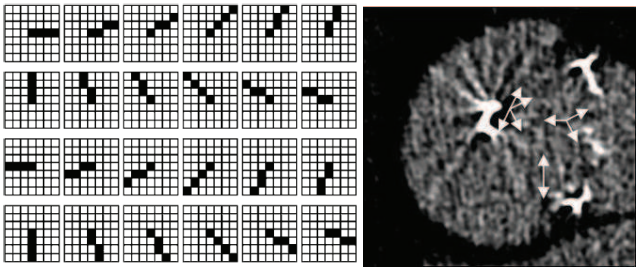

A B

Figure 4 : A, 4 voxels-length 2D asymmetric sticks set [18] and B, 5 voxel-length sticks (white arrows) which give the higher output in 4 positions inside leaflets (SNR of this image is 7.54).

The filter output I' at the current voxel was originally defined as:

$$I' = \frac{1}{W}\sum_{i=1}^{N} g_i \bullet \overline{I}_i \text{, and } W = \sum_{i=1}^{N} g_i \text{,} \qquad (5)$$

where $\overline{I}_i$ denotes the local mean value along the i^{th} stick, N is the number of sticks, and g_i is the reciprocal of local variance along the i^{th} stick, used to classify edge and noise.

This filter was adapted to preprocess CT images of degenerative aortic valve bioprosthesis. In order to improve the results of the original stick filter applied to CT images, we tested different parameters (including local median). At the end of the tests, we found that local median could keep more details of thin structures both visually and in terms of SNR.

In our approach, we used 3D asymmetric sticks set and the resulting value of the filtering process was considered as the sum of voxel median values normalized by the standard deviation along 4 voxels length sticks defined in the neighborhood (Fig. 5). The values of resulting voxels *I'* were more precisely defined as:

$$I' = \frac{1}{W}\sum_{i=1}^{N} g_i \bullet I_{Mi} \text{, and } W = \sum_{i=1}^{N} g_i \text{,} \qquad (6)$$

where I_{Mi} denotes the local median value along the i^{th} stick, N is the number of sticks ($N = 24L^2 - 48L + 26$ in 3D conditions), L is the number of voxels along the stick.
L, the length of stick, is the main parameter of this filter. It is determined by SNR of original CT images. When SNR<=8, *L*=5; 8<SNR<=10, *L*=4; SNR>10, *L*=3.
The process of filtering is applied to the ROI. When part of stick is outside of the ROI, we use original image voxels to complete it.

Besides, the number of iteration is not a critical issue unlike Diffusion filter. Stick filter shows a convergent behavior after several iterations. Typically, in a low SNR condition (SNR<=8), the result converged after 5 iterations (after 3 iterations when SNR>10). It was not necessary to limit the number of iterations to avoid an over-smoothing of edges.

Although both Stick filter and Diffusion filter are "anisotropic" filter, Diffusion often use a small mask (3*3*3) or add a median filter process between 2 iterations to avoid making impulse noise. Stick filter can use much larger mask to get a better result.

The drawback of Stick filter is its high computation complexity. A 5 voxels-length Stick filter (*i.e.* a 9*9*9 cubic neighborhood), requires for each voxel and at each iteration, the calculation of 386 local medians and local variances. The time of calculation can be decreased by the stent-defined ROI. The number of voxels located in the ROI is much less than in the cubic volume encompassing the aortic valve bioprosthesis. Cylindrical ROI typically decreases the number of voxels to 40% and conformational ROI to 16%.

D. Valve segmentation

According to surgical expertise, four main classes of tissues were identified. They were related to HU measured by CT. We considered, from high to low HU, the following classes: stent, calcification, vascular lumen and leaflets. The first two elements, showing high CT values, can be segmented by thresholding easily; the issue of segmentation is more particularly focused on bioprosthetic leaflets.

Three kinds of region-based segmentation processes were implemented, with a decreasing level of user interactivity.

1- Isotropic Region Growing

The first one was an interactive process in order to provide a reference approach for the assessment of the results. It was based on classical Isotropic Region Growing (**IRG**) method.

Following a preprocessing based on Diffusion filtering, as described above, it was applied using 3D Slicer software [25].

The bioprosthesis volume was selected using three different CT slices. Multiple seed points were interactively selected for each component of the prosthesis. The region growing algorithm was started (26-neighbour connectivity) with automatic calculation of the criterion used for the aggregation of voxels. This similarity criterion was based on mean and standard deviation of the voxel values within the considered cubic neighborhood [26-28]. The extraction and visualization of the resulting 3D surface meshes delineating the regions were performed by using the Marching Cube algorithm [19, 25].

2 - Stick Region Growing

To better deal with the segmentation of thin structures, like the components of a valve bioprosthesis and especially valve leaflets, we developed a directional region growing process based on stick neighborhood. The segmentation was thus performed by the stick region growing algorithm applied to a previously selected region of interest (ROI), either cylindrical or conformational, passing through the metallic stent.

Some seeds were interactively selected inside the leaflets at different locations (typically 4 to 6 seeds). A set of N voxels inside the leaflets was defined by considering for each seed the voxels belonging to their neighborhood. The similarity criterion was locally based on mean and standard deviation of the CT voxel values along the directions defined by the sticks. This approach was implemented using MatLab development tools.

In order to examine each voxel in the cubic neighborhood of the seed, we specifically computed the stick variances in the set of sticks defined by each of these voxels:

$Var = \frac{\sum_{j=1}^{L}(I_{i,j} - \overline{I}_i)^2}{L}$, where $I_{i,j}$ is the grey level of j^{th} voxel in i^{th} stick.

L was chosen to be less than the thickness of the leaflets. Typically L was between 3 and 5 voxels (about 1mm).

To ensure region growth is not early stopped, or in other words to limit the number of seed points selection in some critical cases (highly noisy data), the size of the cubic neighborhood was chosen to be large enough to include space between homogeneous fragment of leaflets. We typically used a 342-connected neighborhood (7x7x7).

We also defined $\overline{I_m} = \frac{1}{L}\sum_{j=1}^{L} I_{m,j}$, the local mean of the stick with minimum local variance.

The voxels were classified as belonging to the region of the seed voxel (*i.e.* as a voxel of normal leaflet tissue) when: (i) $\overline{I_m}$ belongs to the grey level range of normal leaflets and (ii) minimum local variance along stick is lower than a variance threshold (VTH). VTH was determined by the difference of local cubic neighborhood variances of leaflets voxels and boundary voxels. These variances have been previously calculated in SNR computation (for image preprocessing). When this voxel belongs to ROI, it constitutes new seed voxels. This process was iterated until no new voxel can be marked as a seed. This segmentation referenced as Stick Region Growing (**Stick RG**) in the following was preceded by a Stick filtering preprocessing step.

3 - Stick Exhaustive Search

To further reduce the level of interactivity in the segmentation process, a systematic exploration of the ROI was implemented with no need for seed point definition. This segmentation referenced as Stick Exhaustive Search (**SES**) in the following was preceded by a Stick filtering preprocessing step.

Looking at the grey level of leaflets/vascular lumen in the preselected and filtered ROI, we manually set the range of grey level thresholds about mean and variance. We divide neighborhood (Radius=3 pixels) of all voxels inside ROI into an asymmetric sticks sets and we automatically calculate local means and local variances along sticks. If the stick values were inside the range we set, the neighborhood voxel was classified as leaflets or vascular lumen. The exploration of the ROI is completely automatic.

III. RESULTS

A. Experimental data

As preoperative assessment, we obtained CT scan images (General ElectricTM Lightspeed® VCT 64) from four patients (HER, MAG, BOU, DAV) presenting a degeneration of aortic bioprosthesis. Depending on the case, the reoperation was performed from 7 to 19 years after implantation. Acquisition protocol was a multi-slice coronary angio-CT-scan ECG gated in 3D + T mode.

We analyzed 4 databases of aortic bioprostheses, explanted for different pathological reasons. In one case it was a pericardial bioprosthesis (HER), in which bovine pericardium is cut to reproduce aortic valve leaflets that are sewn on a complete metallic stent. Three more cases were represented by porcine bioprostheses, in which a porcine aortic valve is mounted on a complete metallic stent (2 cases: MAG and BOU) or incomplete metallic stent (1 case: DAV).

CT-scan sequences were preprocessed and segmented (as described in Fig. 2) to describe the vascular structure as well as the bioprosthesis metallic stent. After reoperation, CT-scan images of isolated explanted aortic bioprosthesis were obtained using the highest image resolution protocol. The main parameters derived from the CT acquisitions of in-vivo (IV) and ex-vivo (EV) aortic bioprosthesis, for each of the four cases, are summarized in Table I.

TABLE I: MAIN PARAMETERS OF IN-VIVO (IV) AND EX-VIVO (EV) ACQUISITIONS.

Patient	Observation	Image size (voxels in X,Y,Z)	Image sampling (mm in X,Y,Z)
HER	IV	512 512 281	0.3125 0.3125 0.625
	EV	512 512 198	0.3125 0.3125 0.3125
MAG	IV	512 512 105	0.318 0.318 0.312
	EV	512 512 110	0.0966 0.0977 0.312
BOU	IV	512 512 153	0.3632 0.3632 0.625
	EV	512 512 120	0.0977 0.0977 0.312
DAV	IV	512 512 290	0.418 0.418 0.635
	EV	512 512 125	0.0977 0.0977 0.3125

B. Preprocessing

The preprocessing based either on Diffusion filter or on Stick filter was applied to the in-vivo CT volumes of the four patients. The bioprosthesis voxels were first isolated by considering the ROI defined by the stent. Ex-vivo images do not need preprocessing. Differences in grey level between stent, leaflets and calcification/pannus are very clear in ex-vivo data.

Examples of original images and resulting images obtained with the two different filters are reported in Figure 5. A first qualitative appreciation of the results let appears that Stick filter based approach seems to better enhance the contrast between valve leaflets and surrounding structures.

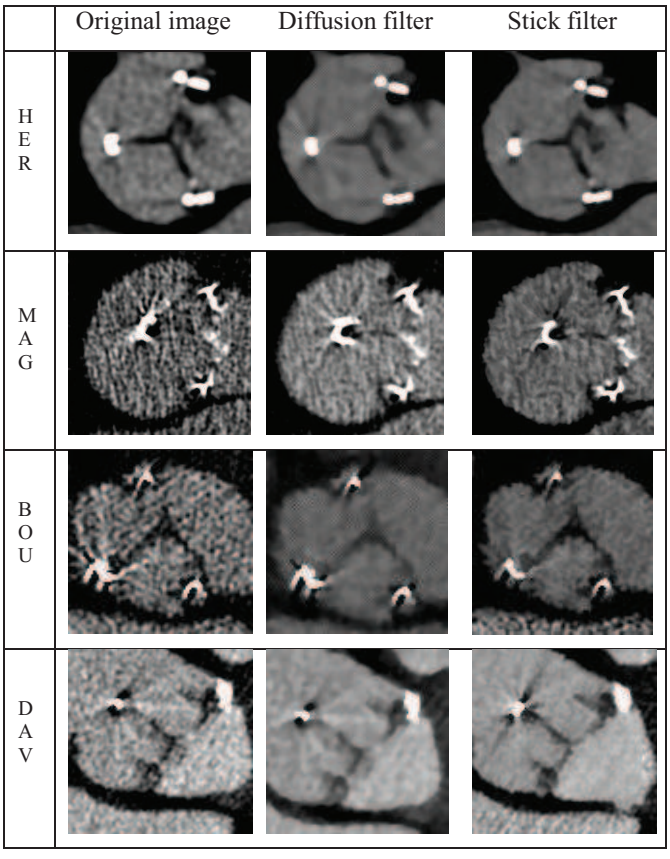

Figure 5: Results of CT images preprocessing by Diffusion and Stick filters.

In addition to this qualitative assessment of the results, SNR was computed on original images and resulting images (Fig. 6). This objective assessment let appear that Stick filtering shows the best SNR for the four patients, and this is consistent with the subjective appreciation.

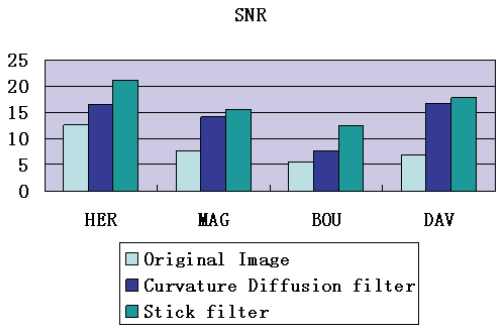

Figure 6: Results of preprocessing (SNR) with Stick filter and Curvature Diffusion filter for each of the four cases (HER, MAG, BOU and DAV).

C. Segmentation

Following the ad hoc preprocessing step, the different segmentation methods (IRG, Stick RG, and SES) were applied to in-vivo (IV) and ex-vivo (EV) images. A qualitative analysis is reported in Fig. 8-9 comparing the methods used in- and ex-vivo to enhance bioprosthetic leaflets and the explanted bioprosthesis.

The first example is reported in the case of the pericardial bioprosthesis (HER). The visualization was performed by surface rendering. Some anatomical similarity as the shape of the leaflets and the presence of minimal leaflet degeneration can be easily appreciated (Fig.7). The leaflet prolapse resulting in no perfect coaptation appears as commissure lost (indicated in blue circle) in the segmented images.

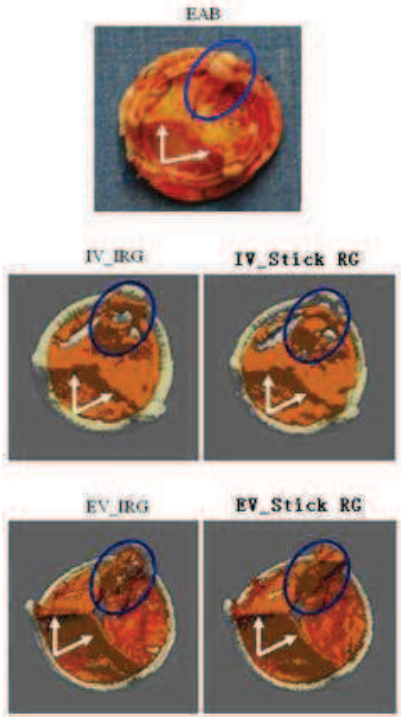

Figure 7: Visualization of the segmentation results obtained in case HER: explanted aortic bioprosthesis (EAB), in-vivo bioprosthesis (IV) and ex-vivo bioprosthesis (EV), segmented with methods IRG and Stick RG. The commissure lost is indicated with blue circle and good leaflets coaptation with white arrows.

The second example illustrates the results obtained in the case of a porcine bioprothesis (MAG). The visualization of front and back side of bioprosthesis was performed by volume rendering with transparency effect (Fig. 8). A calcified pannus (indicated by black arrows) is characteristic in this case and responsible for valve obstruction. Leaflet tear (indicated by green arrows) was also observed and found in reconstructions.

The results on the back side of EV_IRG and EV_SES are not exactly the same. In fact, in this case, when the valve is closed (closed position of leaflets), the pannus developed under the bioprosthesis is in contact with a part of the leaflets (partially calcified). Automatic enhancement of these 2 tissues in contact is quiet difficult. This is the reason why the results show some differences between the methods.

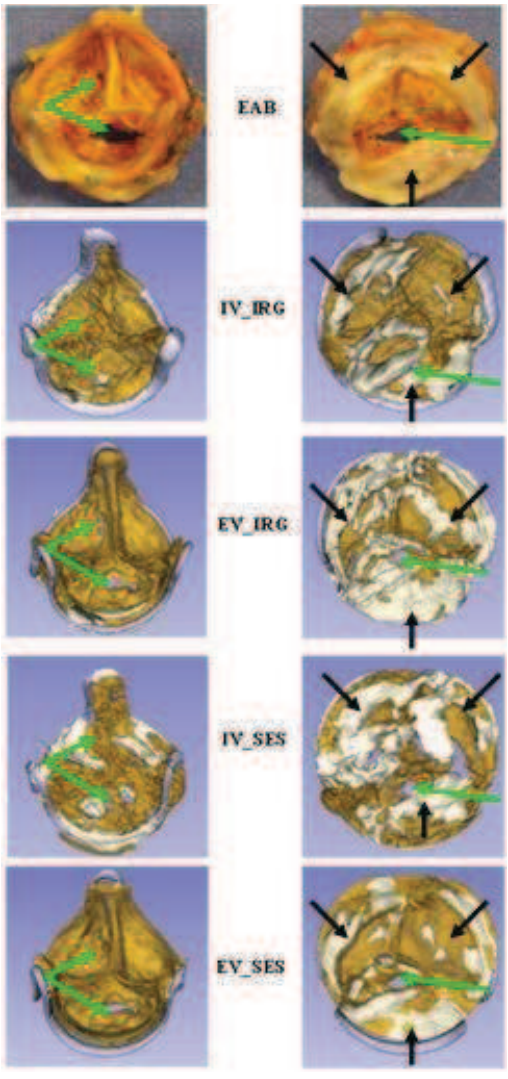

Figure 8: Visualization of the segmentation results obtained in case MAG (Front and Back side) explanted aortic bioprosthesis (EAB), in-vivo bioprosthesis (IV) and ex-vivo bioprosthesis (EV), segmented with methods IRG and SES. Calcified pannus (indicated by black arrows) and leaflet tears (indicated by green arrows) are observed and found.

A quantitative analysis was then conducted to objectively compare the results obtained respectively by IRG, Stick RG, and SES on in-vivo (IV) and ex-vivo (EV) images. It was performed as following: the voxel volume was computed for each database (considering CT acquisition parameters showed in Tab. I) and multiplied by the number of voxels of each bioprosthestic component.

The criterion used to evaluate the results was the volume of bioprothesis components. Results of this analysis are shown in Fig. 9 (volumes are expressed in mm^3). The goal of the quantitative analysis was to show that all these 3 different methods, more or less automatic in their approach, allow to enhance bioprosthetic components including leaflets with similar results. Indeed, looking at computed volumes, differences in values are very similar. In-vivo volumes are generally bigger than ex-vivo and it can be explained mostly by the moving artifacts. For sure, ex-vivo results are more reliable than in-vivo and represent the reference to compare the in-vivo results. But, when we compare the results between in- and ex-vivo for each method, the differences in voxels volumes are always less than 20%.

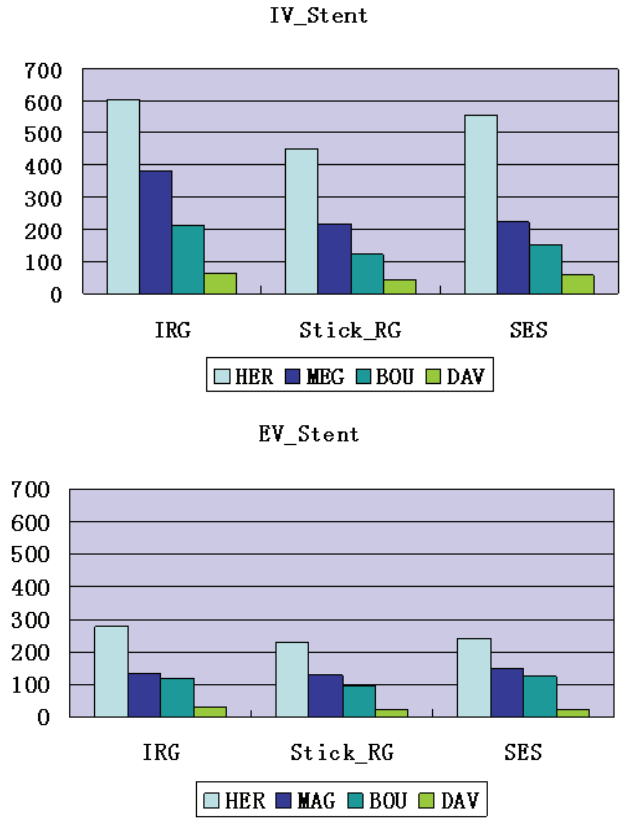

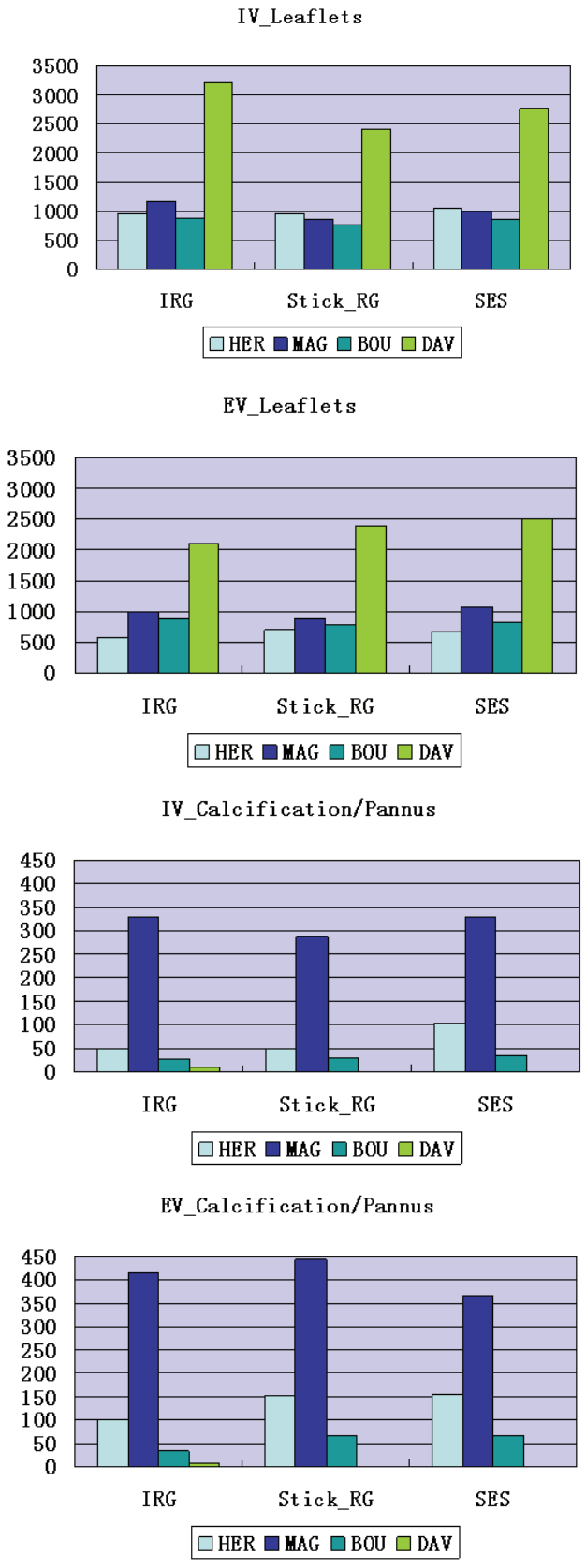

Figure 9: Volume analysis of bioprosthesis components

IV. Discussion

In recent years, multi-detector computed tomography has emerged as a promising tool to provide precise diagnostic information in different clinical situations, such as noninvasive evaluation of coronary disease [29-34], ventricular morphology and function [35], and myocardial viability [36-38]. CT images can also help visualize the morphology and motion of native and diseased stenotic aortic valves and precisely measure aortic valve opening areas. Several studies [39-45] suggest that multi-detector CT can help assess mechanism of dysfunction in mechanical prosthetic heart valve disorders.

An aortic bioprosthesis can have functional degradation and prosthesis dysfunction over time. In more recent bioprostheses, the rate of structural failure appears to be somewhat lower than with the first generation [46], but it is still occurring. Understanding the precise mechanism of bioprosthesis dysfunction would thus be important to direct clinical management. Yet, it can often be difficult to identify these entities in clinical practice. Indeed, both transthoracic and transesophageal echocardiography have limited usefulness for detection of the mechanism of stenotic bioprostheses, because of the acoustic shadowing from valve stents or annulus.

CT images would potentially allow better visualization of the bioprosthetic valve leaflets after aortic valve replacement, but at the moment CT scan softwares don't allow automatic leaflets enhancement. So, additional methods have to be considered to improve leaflets characterization and visualization.

In this study we have tested three different types of segmentation applied to CT images of degenerated aortic bioprosthesis. Considered methods, even if different in their approach, seem to be similar in terms of results. They are considered as semiautomatic segmentation methods.

The mean difference among these methods is that the Isotropic Region Growing method is performed using software for image analysis (3D Slicer), relatively easy to use, but needing heavy interaction for the user (manual selection of different seed points for the different components of the bioprosthesis) . On the other hand, Stick Region Growing and Stick Exhaustive Search methods need, at this time, to be performed by professionals of Matlab development tools, but their interactivity is lower.

The reduced interactivity level results in some differences in terms of voxels volumes. In fact it is difficult to replace the user ability to recognize bioprosthesis different structures in CT transverse sections (IRG) by the automatic criteria based on grey level density (Stick RG and SES).

Quantitative analysis shows these differences among the methods, but we can't consider them significant because of the inability to perform a statistical analysis on these few databases. Moreover, we don't know at the moment if these small differences (always less than 20%) could have a real interest for clinical application. In fact, the goal of

segmentation is to approximately reconstruct leaflet morphology and to detect some failing mechanism as pannus formation that could represent a contraindication to the endovascular procedure.

A key point of the analysis is represented by the preprocessing. In fact, bioprostheses CT images need to be denoised before to be segmented because of metallic stent artifacts. Different filters have been tested in order to improve images with the best leaflets enhancement. Stick filtering, modified in order to be applied to CT images, showed the best visual results and this was confirmed by SNR analyses. This filtering process was performed by MatLab software and it takes time to be finalized. To reduce this computing time it is important to select a ROI that takes into account only the bioprosthesis stent region with its leaflets.

Concerning segmentations results, some considerations have to be done. Among analyzed databases the best results have been obtained in the case of the pericardial bioprosthesis (HER). The reason is attributed to the thickness of valve tissue. In fact pericardial leaflets are largely thicker than porcine with consequent better results for CT images.

The higher bioprosthesis components' volumes observed in some cases for in-vivo images comparing to ex-vivo can be explained by different factors. Firstly, image resolution is not the same. In-vivo acquisition protocol represents the standard protocol used for coronary ECG gated angio-CT-scan. Acquisition parameters cannot be changed and specific acquisition for bioprosthesis analysis doesn't exist at the moment. For ex-vivo we chose the highest resolution protocol to be close to reality and to use these images as reference. Other than image resolution, we can consider heart motion and blood superposition as important factor of volumes differences.

Computing of leaflets volumes can be altered by the non-metallic part of bioprosthesis stent (DAV). Only the metallic stent can be used as spatial limitation for the leaflets because the non metallic part has the same density of the leaflets. For this reason leaflet volumes are higher than normal, especially in the case of incomplete metallic stent.

Another factor that plays a fundamental role for the quality of in-vivo images (preoperative images) is the heart rate during the exam. It should be as low as possible and not more than 80 bpm. Patient preoperative clinical conditions can be responsible for higher heart rate and contra-indicate medical therapy as beta-blockers to reduce it.

In all cases, we observed also in-vivo underestimation of leaflets degeneration. This is only partially true. In fact, in the study cases, leaflets are not so calcified and most part of degeneration consists in leaflets thickening. These leaflets modifications do not appear with the same density of calcifications and are difficult to detect in in-vivo CT images. Only actual calcifications can be detected with consequent underestimation compared to ex-vivo images, in which smaller differences in density can be easily appreciated.

Our study suggests that segmentation of CT images could play a role in clarifying the mechanism of bioprosthesis dysfunction. Indeed, we demonstrated that segmentation can help directly visualize leaflet morphology.
Furthermore, we demonstrated the ability of these methods to identify bioprosthesis leaflet thickening, calcification as well as presence of pannus under bioprosthetic leaflets.

V. Conclusion

Echocardiography remains the gold standard for functional analysis of bioprosthesis failure. In the last years an increasing number of groups are looking with particular interest at CT images for anatomo-morphological analysis of the aortic valve.

Segmentation could be useful in the next future to better understand the morphology of the failing bioprosthesis. Moreover segmentation allows to better visualize some non structural valve dysfunction like subvalvular pannus, difficult to visualize by echocardiography and to recognize by transverse CT scan sections. Finally, it could be interesting to integrate 3D reconstructions into planning tools to optimize the valve-in-valve procedure.

In order to further validate the preliminary results, we are testing the three presented methods for different patients datasets.

Moreover additional types of segmentation approaches are going to be evaluated. Results among different techniques will be compared in order to determine the best method for a relevant 3D bioprosthesis segmentation.

References

[1] Lindroos M, Kupari M, Heikkila J, Tilvis R. Prevalence of aortic valve abnormalities in the elderly: an echocardiographic study of a random population sample. J Am Coll Cardiol 1993;21:1220-1225.

[2] Iung B, Baron G, Butchart E G, Delahaye F, Gohlke-Barwolf C, Levang O W, et al. A prospective survey of patients with valvular heart disease, in Europe: The Euro Heart Survey on Valvular Heart Disease. Eur Heart J 2003;24:1231-1243.

[3] Kojodjojo P, Gohil P, Barker D, Youssefi P, Salukhe T V, Choong A, et al. Outcomes of elderly patients aged 80 and over with symptomatic, severe aortic stenosis: impact of patient's choice of refusing aortic valve replacement on survival. QJM 2008;101:567-573.

[4] Accola KD, Scott ML, Palmer GJ, Thompson PA, Sand ME, Suarez-Cavalier JE, et al. Surgical management of aortic valve disease in the elderly: a retrospective comparative study of valve choice using propensity score analysis. J Heart Valve Dis 2008;17:355-364.

[5] Eitz T, Fritzsche D, Kleikamp G, Zittermann A, Horstkotte H, Korfer R, et al. Reoperation of the aortic valve in octogenarians. Ann Thorac Surg 2006;82:1385-1390.

[6] Jamieson W R, Burr L H, Miyagishima R T. Re-operation for bioprosthetic aortic structural failure—risk assessment. Eur J Cardiothorac Surg 2003;24:873-878.

[7] Cribier A, Eltchaninoff H, Bash A, Borenstein N, Tron C, Bauer F, et al. Percutaneous transcatheter implantation of an aortic valve prosthesis for calcific aortic stenosis: first human case description. Circulation 2002;106:3006-3008.

[8] Grube E, Laborde JC, Gerckens U, Felderhoff T, Sauren B, Buellesfeld L, et al. Percutaneous implantation of the CoreValve self-expanding valve prosthesis in high-risk patients with aortic valve disease: the Siegburg first-in-man study. Circulation 2006;114:1616-1624.

[9] Grube E, Schuler G, Buellesfeld L, Laborde J C, Gerckens U, Felderhoff T, et al. Percutaneous aortic valve replacement for severe aortic stenosis in high-risk patients using the second- and current

third-generation self-expanding CoreValve prosthesis: device success and 30-day clinical outcome. J Am Coll Cardiol 2007;50:69-76.
[10] Cribier A, Eltchaninoff H, Tron C, Bauer F, Agatiello C, Sebagh L, et al. Early experience with percutaneous transcatheter implantation of heart valve prosthesis for the treatment of end-stage inoperable patients with calcific aortic stenosis. J Am Coll Cardiol 2004;43:698-703.
[11] Cribier A., Eltchaninoff H, Tron C, Bauer F, Agatiello C, Sebagh L, et al. Treatment of calcific aortic stenosis with the percutaneous heart valve: mid-term follow-up from the initial feasibility studies: the French experience. J Am Coll Cardiol 2006;47:1214-1223.
[12] Walther T, Falk V, Dewey T, Kempfert J, Emrich F, Pfannmuller B, et al. Valve-in-a-valve concept for transcatheter minimally invasive repeat xenograft implantation, J Am Coll Cardiol 2007;50:56-60.
[13] Wenaweser P, Buellesfeld L, Gerckens U, Grube E. Percutaneous aortic valve replacement for severe aortic regurgitation in degenerated bioprosthesis: the first valve in valve procedure using the Corevalve Revalving system. Catheter Cardiovasc Interv 2007;70:760-764.
[14] Webb J G, Wood D A, Ye J, Gurvitch R, Masson J B, Rodes-Cabau J, et al. Transcatheter Valve-in-Valve Implantation for Failed Bioprosthetic Heart Valves. Circulation. 2010;121:1848-1857.
[15] Zheng Y, Matthias J, Rui L. Automatic Aorta Segmentation and Valve Landmark Detection in C-Arm CT: Application to Aortic Valve Implantation. MICCAI 2010, Part I, LNCS 6361, 2010: 476–483.
[16] Waechter I, Kneser R, Korosoglou G. Patient Specific Models for Planning and Guidance of Minimally Invasive Aortic Valve Implantation. MICCAI 2010, Part I, LNCS 6361, 2010: 526–533.
[17] Czerwinski R N, Jones D L. Line and boundary detection in speckle images, IEEE Transactions Image Processing 1998;7: 1700–1714.
[18] Xiao C, Su Z, Chen Y. A Diffusion stick method for speckle suppression in ultrasonic images. Pattern Recognition Letters 2004; (25)16:1867-1877.
[19] González R C, Woods U. Digital image processing. Prentice Hall (2008).
[20] Perona P, Malik J. Scale space and edge detection using anisotropic Diffusion. IEEE Transactions on Pattern Analysis and Machine Intelligence, 1990, 12(7): 629-639.
[21] Black M J, Sapiro G. Marimont D H, Heeger D. Robust anisotropic Diffusion. IEEE Transactions Image Processing, 1998, 7(3): 412-432.
[22] Yezzi A. Modified Curvature Motion for Image Smoothing and Enhancement. IEEE Transactions Image Processing, 1998, 7 (3):345-352.
[23] Qian Y, Zhang Y, Morgan M. A comparison of medical image segmentation methods for cerebral aneurysm computational hemodynamics. Biomedical Engineering and Informatics (BMEI), 2011 4th International Conference, 2011, 2: 901-904.
[24] Brassel M, Bretin E. A modified phase field approximation for mean curvature flow with conservation of the volume, Mathematical Methods in the Applied Sciences 2011, 34(10): 1157–1180.
[25] Ibáñez L. The ITK Software Guide –Second Edition November 21,2005.
[26] Boskamp T, Rinck D, Link F, Kümmerlen B, Stamm G, Mildenberger P. New vessel analysis tool for morphometric quantification and visualization of vessels in ct and mr imaging data sets. Radiographics, 2004 24(1):287– 297.
[27] Adams R and Bischof L. Seeded region growing. IEEE Transactions. Pattern Anal. Machine Intell. 1994, 16: 641-647.
[28] Fan J, Yau DY, Elmagarmid AK, Aref WG. Automatic image segmentation by integrating color-edge extraction and seeded region growing. IEEE Transactions Image Processing. 2001;10(10):1454-66.
[29] Vanhoenacker PK, Heijenbrok-Kal MH, Van Heste R, Decramer I, Van Hoe L R, Wijins W, et al. Diagnostic performance of multidetector CT angiography for assessment of coronary artery disease: metaanalysis. Radiology 2007 ; 244 : 419 – 428.
[30] Miller JM, Rochitte CE, Dewey M, Arabab-Zadeh A, Ninuma H, Gottlieb I, et al. Diagnostic performance of coronary angiography by 64-row CT . N Engl J Med 2008 ; 359 : 2324 – 2336.
[31] Sun Z, Jiang W . Diagnostic value of multislice computed tomography angiography in coronary artery disease: a meta-analysis. Eur J Radiol 2006 ; 60 : 279 – 286.
[32] Hausleiter J, Meyer T, Hadamitzky M, Zankl M, Gerein P, Dorrler K, et al. Non-invasive coronary computed tomographic angiography for patients with suspected coronary artery disease: the Coronary Angiography by Computed Tomography with the Use of a Submillimeter resolution (CACTUS) trial. Eur Heart J 2007 ; 28 : 3034 – 3041.
[33] Budoff MJ, Dowe D, Jollis JG, Gitter M, Sutherland J, Halamert E, et al. Diagnostic performance of 64-multidetector row coronary computed tomographic angiography for evaluation of coronary artery stenosis in individuals without known coronary artery disease: results from the prospective multicenter ACCURACY (Assessment by Coronary Computed Tomographic Angiography of Individuals Undergoing Invasive Coronary Angiography) trial. J Am Coll Cardiol 2008; 52 : 1724 – 1732.
[34] Mowatt G, Cook JA, Hillis GS, Walker S, Fraser C, Jia X, et al. 64-slice computed tomography angiography in the diagnosis and assessment of coronary artery disease: systematic review and meta-analysis. Heart 2008 ; 94 : 1386 – 1393 .
[35] Juergens KU, Fischbach R. Left ventricular function studied with MDCT. Eur Radiol 2006 ; 16 : 342 – 357.
[36] Mahnken AH, Koos R, Katoh M, Wildberger J E, Spuentrup E, Buecker A, et al. Assessment of myocardial viability in reperfused acute myocardial infarction using 16-slice computed tomography in comparison to magnetic resonance imaging. J Am Coll Cardiol 2005 ; 45 : 2042 – 2047.
[37] Gerber BL, Belge B, Legros GJ, Lim P, Poncelet A, Pasquet A, et al. Characterization of acute and chronic myocardial infarcts by multidetector computed tomography: comparison with contrastenhanced magnetic resonance. Circulation 2006; 113: 823 – 833.
[38] Lardo AC, Cordeiro MA, Silva C, Amado L C, George R T, Slaiaris A P, et al . Contrast-enhanced multidetector computed tomography viability imaging after myocardial infarction: characterization of myocyte death, microvascular obstruction, and chronic scar. Circulation 2006; 113: 394 – 404.
[39] Teshima H, Aoyagi S, Hayashida N, Shojima T, Takagi K, Arinaga K, et al. Dysfunction of an ATS valve in the aortic position: the first reported case caused by pannus formation. J Artif Organs 2005; 8: 270 – 273.
[40] Teshima H, Hayashida N, Fukunaga S, Tayama E, Kawara T, Aoyagi N, et al . Usefulness of a multidetector-row computed tomography scanner for detecting pannus formation. Ann Thorac Surg 2004; 77 : 523 – 526.
[41] Teshima H, Hayashida N, Enomoto N, Aoyagi S, Okuda K, Uchida M. Detection of pannus by multidetector-row computed tomography. Ann Thorac Surg 2003; 75 : 1631 – 1633.
[42] Aoyagi S, Fukunaga S, Arinaga K, Shojima T, Ueda T . Prosthetic valve obstruction: diagnostic usefulness of cineradiography and multidetector-row computed tomography. Thorac Cardiovasc Surg 2007; 55: 517 – 519.
[43] Kim RJ, Weinsaft JW, Callister TQ, Min JK . Evaluation of prosthetic valve endocarditis by 64-row multidetector computed tomography . Int J Cardiol 2007 ; 120 : e27 – e29 .
[44] Tsai IC, Lin YK, Chang Y, Fu YC, Wang CC, Hsieh SR, et al. Correctness of multi-detector-row computed tomography for diagnosing mechanical prosthetic heart valve disorders using operative findings as a gold standard. Eur Radiol 2009 ; 19 : 857 – 867.
[45] Konen E, Goitein O, Feinberg MS, Eshet Y, Raanani E, Rimon U, et al. The role of ECG-gated MDCT in the evaluation of aortic and mitral mechanical valves: initial experience . AJR Am J Roentgenol 2008 ; 191 : 26 – 31 .
[46] Ruggieri VG, Flecher E, Anselmi A, Lelong B, Corbineau H, Verhoye JPh et al. Long-Term Results of the Carpentier-Edwards Supraannular Aortic Valve Prosthesis. Ann Thorac Surg. 2012 Jul 7 [Epub ahead of print].

Decision Letter

[Return to Queue]

To: Vito Giovanni Ruggieri <gianvito_ruggieri@libero.it>
From: jhvd.edstaff@hotmail.com
Subject: JHVD/2012/001446 -- Manuscript Decision
Cc:

MS ID#: JHVD/2012/001446
MS TITLE: CT scan images processing to detect the real mechanism of bioprosthesis failure. Implication for valve-in-valve implantation

Dear Dr. Ruggieri,

We are pleased to inform you that the above manuscript has been accepted for publication, in the Journal of Heart Valve Disease.

If you have not submitted your Copyright Transfer Agreement electronically during submission, please contact the editor at gino.gerosa@unipd.it to request a copy. Your manuscript will not be processed further without a signed Copyright Agreement form.

Best regards,

Gino Gerosa

Journal of Heart Valve Disease
ICR Publishers
Crispin House
12A South Approach, Moor Park,
Northwood HA6 2ET, Phone:44 1923 836 871
Fax:44 1923 836 872
jhvd.edstaff@hotmail.com

CT scan images processing to detect the real mechanism of bioprosthesis failure.

Implication for valve-in-valve implantation

Short title: Enhanced CT in bioprosthesis failure

Vito Giovanni RUGGIERI, MD, Amedeo ANSELMI, MD,
Qian WANG, MD, Simon ESNEAULT, MD, Pascal HAIGRON, MD,
Jean-Philippe VERHOYE, MD PhD

Department of Cardiovascular and Thoracic Surgery, Pontchaillou University Hospital, Rennes, France

KEY WORDS: Biological bioprosthesis; Transcatheter valve implantation; Imaging

Address for correspondence:

Vito Giovanni RUGGIERI, MD

Service de Chirurgie Thoracique et Cardiovasculaire

Hopital Pontchaillou

2, rue Henri Le Guilloux

35003 Rennes Cedex 9, France

Tel# 0033-299-28-91-64

Fax# 0033-299-28-24-96

Email: gianvito_ruggieri@libero.it

Abstract

Background and aim: The valve-in-valve is an emerging transcatheter option for patients structural deterioration of aortic bioprosthesis and excessive surgical risk. We illustrate a case which underlines the need for dedicated imaging to accurately understand the mechanism of valve failure and the feasibility of valve-in-valve procedure.

Materials and Methods : A patient with structural bioprosthetic deterioration at echocardiography was studied using CT scan with the novel 3D slicer software. The findings were compared with intraoperative pathology.

Results : Post-processed CT scan images revealed that the bulk of calcifications were located at the subvalvular level, suggesting the presence of calcified pannus. Pathology of the explanted valve confirmed that the valve stenosis was due primarily to the pannus. Misdiagnosed calcified pannus is a threaten during valve-in-valve procedure due to embolic risk.

Conclusions : The 3D slicer elaboration of CT scan could be invaluable to precisely define the mechanism of valve failure and establish the indication to either valve-in-valve procedure or conventional surgery.

Introduction

Transcatheter implantation of an expandable aortic valve prosthesis within a failed surgical bioprosthesis (TAV-in-SAV) is an emerging option for patients at high surgical risk for redo cardiac surgery [1]. The planning of this procedure includes not only the knowledge of the mechanical properties of the bioprostheses [2], but also a precise understanding of the modality of failure in each individual patient who is candidate to TAV-in-SAV. Herein we describe the case of a patient whose failing bioprosthesis was evaluated with the use of a dedicated method for CT scan images processing. We discuss the potential implications of such methodology in the assessment of feasibility and planning of the TAV-in-SAV procedure.

Case presentation

A 63-years-old male patient with no major comorbidities was referred to our Institution for NYHA class II dyspnea. Nineteen years earlier he underwent surgical aortic valve replacement with a Carpentier (Edwards, Irvine, CA, USA) 25 mm porcine bioprosthesis. At physical examination he presented a systo-dyastolic murmur in the aortic position. Preoperative transthoracic echocardiography revealed the presence of important leaflet calcifications and hypomobility, responsible for moderate-to-severe stenosis (mean transvalvular gradient 44 mmHg) and associated moderate regurgitation. No further valve anomalies could be evidenced (Figure 1). Multislice EKG-gated coronary angio-CT-scan was also performed during the preoperative assessment to exclude coronaropathy; the patient had no major risk factors and normal coronary arteries at first operation. The plasma creatinine concentration and creatinine clearance were 101 mmol/L and 79 ml/min, respectively, which therefore did not pose contraindication to administration of contrast agent. The logistic EuroSCORE I was 9.57%, and the EuroSCORE II was 2.97%. At first analysis, CT-scan images confirmed the presence of important calcifications at the level of prosthetic leaflets. The

images were then processed using 3D slicer software. 3D Slicer is a open source software for visualization and image analysis. CT scan images have been filtered to reduce noise and processed with a method called interactive segmentation that applies the region growing algorithm to segmentate and reconstruct the bioprosthesis in all its components (Figure 2).

The post-processing results showed a different mechanism of failure: the major bulk of calcifications was positioned underneath the bioprosthesis in the form of a compactly calcified pannus.

Re-operation was performed. Mild intrapericardial adhesions were found. Under cardio-pulmonary bypass and cardioplegic arrest (cold cristalloid St. Thomas solution), an oblique aortotomy was performed and the failing bioprosthesis exposed. We discovered multiple tears on thick but not calcified leaflets. Leaflets were only mildly hypomobile. During prosthesis excision, a thick and calcified pannus became evident on the ventricular side, corresponding to the entire circumference of the sewing ring (Figure 3). The pannus showed a stony consistence, covered approximately 40% of the inner valve orifice and was deemed responsible for hemodynamic stenosis. The native aortic annulus was rinsed and a new Perimount (Edwards, Irvine, CA, USA) 25 mm pericardial bioprosthesis was implanted. The postoperative course was uneventful.

Discussion

Although still considered an off-label indication, the TAV-in-SAV procedure represents an alternative to reoperation for patients at high surgical risk with dysfunctioning aortic bioprosthesis [2, 3]. Though it is most frequent in the presence of a mechanical prosthesis, pannus overgrowth is a mechanism for nonstructural bioprosthetic dysfunction which may represent an unexpected intraoperative finding. In the majority of cases its extent is mild, but in some instances it can be exuberant and contribute significantly to the valve failure. [4]. Additionally, overtime pannus may calcify and, therefore, become non-distensible at the time of transcatheter valve implantation or even represent a potential source of emboli during pre-deployment balloon aortic valvuloplasty. In the largest published review of TAV-in-SAV procedures [1], it is reported that failure of the TAV-in-SAV procedure and the instances of periprocedural death were due to device migration in one case, post-deployment obstruction of the left main ostium in one case and myocardial dysfunction likely due to coronary obstruction in two cases. Such findings emphasize the need to improve the preoperative imaging and evaluation of these complex patients. To such purpose, we are evaluating the contribution of preoperative CT-scan images processing.

Preprocedural CT scan is now believed mandatory for the planning of any transcatheter aortic valve implantation. In the setting of bioprosthetic dysfunction, the processing method we have used may play a major role in procedure planning by achieving a precise picture of both the inner prosthetic dimension and of the lesion responsible for failure. Additionally, excessive pannus growth may determine a mismatch between the nominal and the factual measures of the internal diameter of stented bioprostheses, with following implications on the size of the transcatheter valve to be deployed. Evidence has been collected that the current transcatheter devices are unreliable for relieving stenosis in the context of landing areas having smaller dimensions [5, 6]. Therefore, a relative contraindication to the TAV-in-SAV procedure may arise after insightful CT scan-guided assessment of the mechanisms of failure, of the factual diameter and morphology of the landing

zone by means of volume rendering or interactive segmentation. As underscored by the review of the present case, were echocardiography failed to identify the mechanism of bioprosthetic dysfunction (Figure 1), this imaging modality is unreliable in adequately addressing such issues. Consistently, previous investigations have indicated the limits of both transthoracic and transesophageal echocardiography in detecting prosthetic failure due to pannus overgrowth, mainly with respect to aortic bioprostheses [7]. In a systematic analysis of evaluation of prosthetic valve dysfunction, echocardiography (any modality) failed in the majority of cases to identify subvalvular pannus as the mechanism for the observed valve dysfunction in both mechanical and biological aortic prostheses [4]. Therefore, we believe that the routine preoperative multislice EKG-gated CT scan images processing by interactive segmentation using 3D Slicer software could be useful to avoid unexpected intraprocedural threatens. A potential limitation of this approach consists in the possible coexistence of impaired renal function, which may contraindicate contrast-enhanced CT scan in some cases. A longitudinal study of the diagnostic performance of interactive segmentation of CT scan images with pathological correlations is warranted and is now ongoing.

References

1. Piazza N, Bleiziffer S, Brockmann G et al. Transcatheter aortic valve implantation for failing surgical aortic bioprosthetic valve (Part 2). *JACC Cardiovasc Intervention 2011;4:733-42.*
2. Piazza N, Bleiziffer S, Brockmann G et al. Transcatheter aortic valve implantation for failing surgical aortic bioprosthetic valve (Part 1). *JACC Cardiovasc Intervention 2011;4:721-32.*
3. Gotzmann M, Mugge A, Bojara W. Transcatheter aortic valve implantation for treatment of patients with degenerated aortic bioprostheses – Valve-in-valve technique. *Catheter Cardiovasc Intervention 2010;76:1000-6.*
4. Girard SE, Miller FA, Orszulak TA et al. Reoperation for prosthetic aortic valve obstruction in the era of echocardiography: trends in diagnostic testing and comparison with surgical findings. *J Am Coll Cardiol 2001;37:579-84.*
5. Azadani A, Jussaud N, Matthews P, Ge L, Chuter T, Tseng E. Transcatheter aortic valve inadequately relieves stenosis in small degenerated bioprosthesis. *Interact Cardiovasc Thorac Surg 2010;11:70-7.*
6. Azadani A, Jussaud N, Ge L, Chitsaz S, Chuter T, Tseng E. Valve-in-valve hemodynamics of 20-mm transcatheter aortic valves in small bioprosthesis. *Ann Thorac Surg 2011;548-55.*
7. Adam MC, Tribouilloy C, Mirode A, Marek A, Rey JL, Lesbre JP. Value and limits of single-plane transesophageal echocardiography in dysfunctions of aortic valve prosthesis. *Arch Mal Coeur Vaiss 1993;86:1017-23.*

Figure Legends.

Figure 1. Preoperative transthoracic echocardiography, showing no abnormal images at the subvalvular level (black arrowhead).

Figure 2. Preoperative CT scan images processed using 3D slicer software. The calcified regions are showed as green areas, and are shown to be located mainly at the subvalvular level. This suggest the presence of calcified subvalvular pannus.

Figure 3. Pathological examination of the explanted failed bioprosthesis. **A.** Aortic side. Although mild calcifications and two tears (black arrows) are present, the leaflets are pliable and only mildly hypomobile. **B.** Ventricular side. Pannus is present at the subvalvular level, covering approximately 40% of the valve orifice area. The pannus was calcified and had a stony consistence.

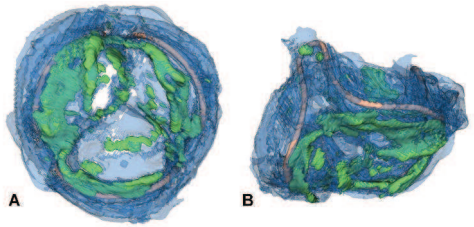
A
B

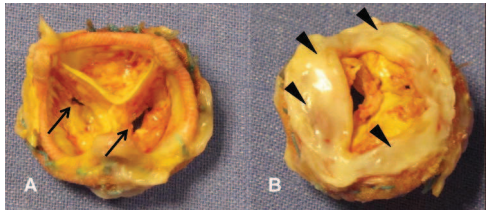
A
B